STUDY OF OPTICAL PROPERTIES OF SKIN TISSUES

FROM ULTRA-VIOLET TO SHORT-WAVE INFRARED

A Dissertation

Presented to

the Faculty of the Department of Physics

East Carolina University

In Partial Fulfillment

of the Requirements for the Degree

Doctor of Philosophy in Biomedical Physics

by

Xiaoyan Ma

June 2004

STUDY OF OPTICAL PROPERTIES OF SKIN TISSUES

FROM ULTRAVIOLET TO SHORT-WAVE INFRARED

by

Xiaoyan Ma

APPROVED BY:
ADVISOR OF DISSERTATION Xin-Hua Hu
XIN-HUA HU, Ph. D.
DEPARTMENT OF PHYSICS

COMMITTEE MEMBER Mumtaz A. Dinno
MUMTAZ A. DINNO, Ph. D.
DEPARTMENT OF PHYSICS

COMMITTEE MEMBER Robert M. Lust
ROBERT M. LUST, Ph. D.
DEPARTMENT OF PHYSIOLOGY

COMMITTEE MEMBER Edward J. Seykora
EDWARD J. SEYKORA, Ph. D.
DEPARTMENT OF PHYSICS

COMMITTEE MEMBER William A. Wooden
WILLIAM A. WOODEN, M. D.
DEPARTMENT OF SURGERY

DEAN OF THE GRADUATE SCHOOL Paul Tschetter
PAUL TSCHETTER, Ph. D.

Abstract

Xiaoyan Ma STUDY OF OPTICAL PROPERTIES OF SKIN TISSUES FROM ULTRA-VIOLET TO SHORT-WAVE INFRARED. (Under the direction of Dr. Xin-Hua Hu) Department of Physics, June 2004.

Accurate knowledge of optical properties of skin tissues is fundamental to the study of tissue optics and development of optical instrumentation in clinics. The goal of research described in this dissertation is to develop a system of experimental methods and theoretical models for the inverse determination of optical parameters of mammalian tissues and various tissue phantoms. Based on the integrating sphere and spatial filtering techniques, various experimental systems have been constructed and improved to measure the diffuse reflectance, the diffuse transmittance, and the collimated transmission of turbid sample~~s~~ from the spectral region of ultraviolet to short-wave infrared. Different Monte Carlo based algorithms have been developed to simulate photons transportation under different experimental configurations based on the radiation transfer theory. And the corresponding procedures for inverse determination of optical parameters from the experimental data have been established.

We have determined the complex refractive index of polystyrene microspheres as a function of wavelength from 370 nm to 1610nm using a Monte Carlo model in combination with the Mie phase function. The optical parameters of porcine skin dermis tissues have also been determined by assuming the surface of the dermis samples were flat and smooth. The effect of surface roughness on the inverse determination of bulk optical parameters of a turbid sample has been investigated. We found that the condition

of sample surface plays an important role in determining the light distribution in a turbid sample. Numerical simulations have shown that the surface roughness on scales close to the wavelength of light can significantly affect the values of bulk tissue optical parameters inversely determined from in vitro measurements even for a moderate index mismatch. As a result, we have developed a confocal imaging method to measure the surface profile of slab samples of fresh porcine skin dermis and extracted the profile parameters. With this knowledge, the surface roughness corrected optical parameters of porcine dermis tissue have been determined at the wavelengths of 325, 442, 532, 632.8, 850, 106.4, 1330, and 1550 nm.

Acknowledgements

I would like to thank Dr. Xin-Hua Hu for being the advisor of my Ph.D. dissertation. Dr. Hu gave me constant and unfailing advices during my four years at Department of Physics, East Carolina University. It was his solid knowledge and original insight that made this project possible. Especially, I am greatly indebted to him for his time and patience in reviewing the writing of this manuscript.

I would like to express my sincere gratitude to Dr. Jun Qing Lu for allowing me to use the Monte Carlo simulation codes she developed with her ingenuity and years of efforts. Without those codes I couldn’t imagine how the accomplishment of this project could make.

My thanks also go to Dr. Ping Yang from Texas A&M University for providing me a Mie calculation code he developed.

I would like to thank Dr. Mumtaz A. Dinno, Dr. Robert M. Lust, Dr. Edward J. Seykora, and Dr. William A. Wooden for serving on my dissertation committee and reviewing this manuscript.

I would like to thank Department of Comparative Medicine and Dr. You Su Sun from Department of Surgery for providing the porcine skin samples.

Thanks and appreciations are also due to Mr. Kenneth M. Jacobs for his helps in constructing the experimental systems.

I would like to thank the Department of Physics for their supports to my study and research here.

To My Family

Table of Contents

List of Figures

List of Tables

List of Symbols

Symbol	Name	Unit
C_{abs}	Absorption cross section	m^{-2}
C_{ext}	Attenuation cross section	m^{-2}
C_{sca}	Scattering cross section	m^{-2}
$\vec{E}$	Electric field of a plane wave	N/C
$\vec{E}_i$	Incident electric field	N/C
$\vec{E}_s$	Scattered electric field	N/C
g	Anisotropy factor	
$\vec{H}_i$	Incident magnetic field	
$\vec{H}_s$	Scattered magnetic field	
$\vec{H}$	Magnetic field of a plane wave	
I_i	Radiance or intensity of incident wave	
k	Wave number	m^{-1}
λ	Wavelength	m
$L(\vec{r},\hat{s})$	Radiance	
NA	Numerical aperture	
n_i	Imaginary part of a complex refractive index	
n_r	Real part of a complex refractive index	
$p(\hat{s},\hat{s}')$	Phase function	

R_c	Specular reflection	
R_d	Diffuse reflectance	
$\vec{S}$	Time-averaged Poynting vector	
$\vec{S}_s$	Scattered component of $\vec{S}$	
$\vec{S}_{ext}$	Attenuated component of $\vec{S}$	
T_c	Collimated transmission	
T_d	Diffuse transmittance	
μ_a	Absorption coefficient	mm^{-1}
μ_s	Scattering coefficient	mm^{-1}
μ_s'	Reduced scattering coefficient	mm^{-1}
μ_t	Attenuation coefficient	mm^{-1}
W_{abs}	Absorbed energy	
W_{ext}	Attenuated energy	
W_{sca}	Scattered energy	

Chapter 1 Introduction

The study of biomedical application of optical technologies has attracted active research efforts over the last two decades. A growing number of optical therapies and optical diagnoses such as photodynamic therapy [Henderson and Dougherty 1992], laser surgery procedures [Jacques and Prahl 1987], and optical coherent tomography [Huang et al 1991, Schmitt 1999] rely on the accurate knowledge of light-tissue interaction. However, the complex structures render most human tissues as highly turbid media according to their response to the optical radiations from ultraviolet to infrared regions. In addition to being absorbed, light propagating inside tissues experiences significant scatterings. The strong scattering of light in tissues presents a great challenge to characterize quantitatively the optical property of tissues [Cheong et al 1990].

Skin, as the interface between human body and optical environment, is one of the most important organs to study and develop photomedicine. Understanding the propagation of light in skin tissues is therefore fundamentally important to many applications of optical therapy and diagnosis [Anderson and Parrish 1981, Van Gemert et al 1989]. Extensive investigations have been carried out experimentally and theoretically in the past decades to determine skin tissues' optical properties. However, because of the turbid nature of the tissues, the theoretical models and experimental procedures employed in the previous studies need to be further developed to determine accurately optical properties of skin tissues and to advance optical technology in medical applications. The long-term goal of our research is to develop a system of experimental methods and theoretical models for accurate determination of optical parameters of mammalian tissues. In this dissertation, we used porcine skin dermis and other turbid samples as the models of human skin to study the optical properties of skin tissues in spectral regions from ultraviolet to near-infrared. For this purpose, we developed theoretical and numerical methods to take into account the effect of surface roughness on determination of the bulk optical parameters of a turbid sample. These theoretical investigations were combined with the experimental measurements to extract inversely the bulk optical parameters of the porcine skin dermis tissues and other turbid samples.

Development of tissue phantoms is critical to the study of tissue optics and calibration of optical instrumentation in clinics. Aqueous suspensions of polystyrene microspheres have long been used as tissue phantoms to calibrate instruments for measurements of light distributions [Peters et al 1990, Hull et al 1998, Shvalov et al 1999, Du et al 2001]. In addition, polystyrene microspheres are also employed as carriers of different biomedical agents such as antibody markers for a wide range of biomedical research [Kettman et al 1989]. The attractiveness of the polystyrene microspheres as the calibration standard lies in the fact that the scattering and absorption cross-sections of the spheres can be accurately calculated with the Mie theory [Bohren and Huffman 1983]. In this dissertation, we describe an inverse method based on the Monte Carlo simulation with a Mie phase function to accurately determine the complex refractive index of the polystyrene in the form of microspheres from the optical measurements of its water suspensions.

In Chapter 2, a brief review of the Mie theory is first introduced, which precisely predict the light scattering and absorption by a spherical particle. Compared with the conventional Mie formulation for a spherical particle immersed in a non-absorbing medium, the Mie theory for a spherical particle in an absorbing medium shows different features. Recent developments of the Mie theory are discussed. For light transportation in tissues on the macroscopic scales of mm or larger, we present the radiation transfer theory as an accurate model to describe light transportation within a turbid medium at the macroscopic level based on the law of energy conservation. Then the diffusion approximation of the radiation transfer theory is discussed to investigate the thickness dependence of light transmission for slab tissue samples. At the end of Chapter 2, the confocal imaging theory is presented to demonstrate its ability to evaluate the surface roughness of the tissue samples.

Absence of the analytic solutions of the radiation transfer equations under the realistic boundary conditions makes the Monte Carlo simulation the most resorted method to model light distribution in a turbid medium with real boundary conditions. In Chapter 3, the principle of Monte Carlo simulation and the algorithms for photon tracking in a turbid medium are briefly reviewed. For our investigation on light scatterings by spherical particles, the effect of different phase functions, the Henyey-Greenstein function and Mie phase function, on the determination of its optical properties of the turbid medium is discussed.

Boundary conditions play a critical role in determining the light distribution in a turbid medium and the detection of light signals outside the medium. Therefore, the interface profiles adopted in the Monte Carlo modeling will significantly affect the light distributions within the turbid medium and how accurately the optical parameters of turbid medium can be inversely determined. A code that is capable to consider surface roughness of the skin and turbid samples is developed for our Monte Carlo simulations and studies of rough interfaces effects are conducted. Since optical parameters like scattering coefficient, absorption coefficient, anisotropy factor, and complex refractive index can't be measured directly for a turbid medium, proper inverse calculations have to be performed. In this dissertation research, different inverse procedures are employed in order to obtain optical parameters efficiently under different interface conditions for tissue or spherical particles.

Chapter 4 presents the design of various experimental setups employed for the measurements of the diffuse reflectance R_d, the diffuse transmittance T_d, and the collimated transmission T_c from skin tissues and other turbid samples. Weak signal detection and data acquisition with low-noise preamplifier and lock-in amplifier are discussed. Sample preparations for porcine dermis tissue and polystyrene microsphere suspensions are given in detail. Scanning confocal microscope method for the surface roughness evaluation is described at the end.

The results of our investigations on porcine dermis tissue and polystyrene microsphere suspensions are presented in Chapter 5. The experimental systems for the measurements of R_d, T_d, and T_c from skin tissues and other turbid samples were calibrated. The Monte Carlo codes developed for the inverse determination of the optical parameters of skin tissues and other turbid samples from its optical measurements were validated through numerical “experiments”. The complex refractive index of polystyrene in the form of sphere has been inversely determined from the optical measurements of its microsphere suspensions for a spectral region between 370 nm and 1610nm. Optical parameters μ_s, μ_a, and g of porcine dermis tissue were first determined without considering the surface roughness. Numerical investigations indicate that surface roughness significantly affect the light distribution in the sample and dramatically change the inversely determined optical parameters. With the surface roughness measured by confocal imaging, the corrected optical parameters were obtained at 8 wavelengths from 325 nm to 1550nm. In Chapter 6, we discuss and summarize the results of this dissertation research, and point out possible research that should be pursued in the future.

Chapter 2 Theoretical Frameworks

We will first introduce the Mie theory to lay a foundation for understanding the light scattering and absorption in turbid media including biological tissues. Derived directly from Maxwell's equations, the Mie theory provides an analytic solution to the problem of the interaction of light with a spherical particle within a host medium. The effect of the host medium absorption on the optical properties of the microsphere suspensions will be particularly noted. Based on the law of energy conservation, the radiation transfer theory models accurately at the macroscopic level how light distributes inside a strongly turbid medium. The diffusion approximation of the radiation transfer theory is examined to evaluate the thickness effect on light transmission for slab tissue samples. We will also discuss the principle of confocal optical imaging that is used to measure the surface profile of skin tissue samples.

2.1 Introduction

Numerous studies have been carried out on skin tissues to investigate their optical properties in the visible and shortwave infrared (SWIR) region. Among the early investigations, Hardy *et al*. (1956) have measured goniometrically visible and infrared transmittance of human skin *in vitro* and found that light scattering dominates over absorption and has a strong forward characteristics over the spectral region between 0.5 and 1.23μm in wavelength. Anderson and Parrish (1981) obtained the spectral scattering (S) and absorption (K) coefficients for human skin *in vitro* based on a modified Kubelka-Munk flux theory [Kubelka 1948, Kulbelka 1954, Van Gemert et al 1987] from the measurements of transmittance and remittance of thin dermal section of typical thickness near 200μm in the spectral region from 300nm to 2400nm. Van Gemert *et al*. (1989) calculated the scattering and absorption coefficients using a diffusion model from previously published data on human dermis. Marchesini *et al* (1992) investigated the optical properties of human epidermis *in vitro* in the wavelength region from 400 to 800nm by measuring the diffuse reflectance and transmittance with integrating sphere. Based on the 1-D diffusion approximation of the radiation transport theory, the values of μ_a, μ_s' were calculated. We note that all these models used to inversely calculate the optical parameters are various approximations to the radiation transport equation.

With the rapid advances in computer technology, a computationally intensive method of Monte Carlo simulation has received wide attention for its ability to precisely solve the light transportation problems with realistic boundary conditions within the framework of radiation transport theory. In 1983, Wilson and Adams (1983) firstly proposed that Monte Carlo modeling be applied to calculate light dosimetry in tissues. Peters *et al*. (1990) reported the determination of (μ_a, μ_s, g) for breast tissues from measurements of the diffuse reflectance, transmittance and collimated transmission through inverse Monte Carlo calculations. Graaff *et al* (1993) inversely calculated μ_a and the reduced scattering coefficient, $\mu_s' = (1-g)\mu_s$, by using Monte Carlo simulation from the literature data on the measured total transmittance and total reflectance of samples of human skin *in vitro* at wavelengths between 300 nm to 1300nm. Simpson *et al* (1998) measured *ex vivo* the diffuse reflectance and transmittance using an integrating sphere and obtained μ_a and μ_s' of human skin through Monte Carlo simulations between 620nm and 1000nm. Recently, Du *et al* (2001) studied the optical property of porcine skin dermis from 900nm to 1500nm by using an approach similar to that reported by Peters *et al* (1990).

Based on the above discussions, we found that significant gaps exist in the knowledge base of skin optics in the spectral region from UV to SWIR. There are very few data on the optical properties of human skin tissues for wavelengths above 1100nm or below 400nm while these regions are important for medical applications such as laser ablation [Oraevsky *et al* 1991] and optical coherent tomography [Tearney *et al* 1995]. Furthermore, the surface roughness of tissue samples used for its optical property measurements has not yet been studied which may cause very large deviations of the inversely calculated bulk optical parameters from their true values and significant fluctuation in the results reported by different research groups. Surfaces of skin samples used in the reported measurements were assumed to be flat in their theoretical models and thus light deflection at an index mismatched tissue surface was included in the bulk scattering. In this dissertation, we present a comprehensive research plan to obtain inversely the bulk optical parameters (μ_a, μ_s, g) of skin tissues accurately in a broad spectral region from 200 nm to 2500nm by combining techniques of spatial filtering and integrating sphere measurements and Monte Carlo simulations of light transport in tissue. The surface roughness of the tissue samples will be quantitatively determined by means of confocal imaging measurements and statistical analysis. The effect of surface roughness will be modeled through Monte Carlo simulations to obtain the bulk optical parameters of the fresh porcine skin dermis tissues.

2.2 The Mie Theory

In principle, Maxwell's equations provide the foundation to understand the propagation of light in condensed matters including turbid medium. But its drawback lies in the extreme mathematical complexities for systems containing particles of irregular shapes and inhomogeneous properties, and hence its usefulness for understanding turbid medium is limited. The Mie theory provides one of the few analytical solutions of the light scattering problems for a spherical particle embedded in a medium. Combining Mie theory and the Monte Carlo simulations, we establish an accurate model of light distribution in microsphere suspensions which are often used as tissue phantoms for calibrating optical instruments and investigating cell and tissue optics [Ma et al 2003].

When an electromagnetic wave $(\vec{E}, \vec{H})$ propagates in a linear, isotropic, homogeneous medium, it must satisfy the following wave equations

$$\nabla^2 \vec{E} + k^2 \vec{E} = 0 , \tag{2.1}$$

$$\nabla^2 \vec{H} + k^2 \vec{H} = 0 , \tag{2.2}$$

derived from the Maxwell’s equations for a monochromatic wave

$$\nabla \cdot \vec{E} = 0 , \tag{2.3}$$

$$\nabla \cdot \vec{H} = 0 , \tag{2.4}$$

$$\nabla \times \vec{E} = i\omega\mu \vec{H} , \tag{2.5}$$

$$\nabla \times \vec{H} = -i\omega\varepsilon\vec{E} , \tag{2.6}$$

where $k = \omega^2\varepsilon\mu$ is the wave number, ω is the angular frequency of the wave, ε is the permittivity of the medium, and μ is the permeability of the medium.

Instead of solving $\vec{E}$ and $\vec{H}$ vectors directly from Eq. (2.1) and (2.2), Mie (1908) proposed to construct two vector functions by introducing a scalar function ψ in a spherical polar coordinates (r, θ, ϕ) :

$$\vec{M} = \nabla \times (\vec{r}\psi) , \tag{2.7}$$

$$\vec{N} = \frac{\nabla \times \vec{M}}{k} , \tag{2.8}$$

where $\vec{M}$ and $\vec{N}$ possess the properties:

$$\nabla \cdot \vec{M} = 0 , \tag{2.9}$$

$$\nabla \cdot \vec{N} = 0 , \tag{2.10}$$

$$\nabla \times \vec{N} = k\vec{M} , \tag{2.11}$$

$$\nabla \times \vec{M} = k\vec{N} . \tag{2.12}$$

More importantly, if ψ is a solution of a scalar wave equation in the spherical polar coordinates, i.e.,

$$\frac{1}{r}\frac{\partial}{\partial r}\left(r^2\frac{\partial\psi}{\partial r}\right)+\frac{1}{r^2\sin\theta}\frac{\partial}{\partial r}\left(\sin\theta\frac{\partial\psi}{\partial\theta}\right)+\frac{1}{r^2\sin\theta}\frac{\partial^2\psi}{\partial\phi^2}+k^2\psi=0, \tag{2.13}$$

then $\overrightarrow{M}$ and $\overrightarrow{N}$ will satisfy the vector wave equation:

$$\nabla^2\overrightarrow{M}+k^2\overrightarrow{M}=0, \tag{2.14}$$

$$\nabla^2\overrightarrow{N}+k^2\overrightarrow{N}=0. \tag{2.15}$$

Therefore, $\overrightarrow{M}$ and $\overrightarrow{N}$ have all the required properties of an electromagnetic field. And the problem of finding solution of vector wave equations (2.1) and (2.2) is reduced to finding scalar solutions to the wave equation (2.13), which drastically decrease the mathematical complexity of the problem.

2.2.1 The Mie Theory for a Nonabsorbing Host Medium

Consider first that a plane harmonic wave $\left(\vec{E}_i,\vec{H}_i\right)$ illuminates a sphere embedded in a medium nonabsorptive to the incident wave, as shown in Fig 2.1. In the medium outside the sphere, the electromagnetic field is the superposition of the incident wave $\left(\vec{E}_i,\vec{H}_i\right)$ and the scattered wave $\left(\vec{E}_s,\vec{H}_s\right)$:

$$\vec{E}=\vec{E}_i+\vec{E}_s, \tag{2.16}$$

$$\vec{H}=\vec{H}_i+\vec{H}_s. \tag{2.17}$$

It is pointed out [Bohren and Huffman 1983] that the energy absorbed by the particle is given by

$$W_{abs} = -\int_A \vec{S} \cdot \hat{e}_r dA \,, \tag{2.18}$$

and the energy scattered by the sphere is given by

$$W_{sca} = \int_A \vec{S}_s \cdot \hat{e}_r \, dA \,, \tag{2.19}$$

where A represents a closed surface surrounding the particle; $\hat{e}_r$ is unit vector along the radial direction in spherical polar coordinates; $\vec{S}$ is the time-averaged Poynting vector and is defined as

$$\vec{S} = \frac{1}{2} \mathrm{Re}\left\{\vec{E} \times \vec{H}^*\right\}, \tag{2.20}$$

and $\vec{S}_s = \frac{1}{2} \mathrm{Re}\left\{\vec{E}_s \times \vec{H}_s^*\right\}$. Furthermore, the total energy removed or extinguished from the incident wave W_{ext} will be the sum of W_{abs} and W_{sca}

$$W_{ext} = W_{abs} + W_{sca} \,, \tag{2.21}$$

and can be expressed as

$$W_{ext} = -\int_A \vec{S}_{ext} \cdot \hat{e}_r \, dA \,, \tag{2.22}$$

where $\vec{S}_{ext} = \frac{1}{2}\mathrm{Re}\left\{\vec{E}_i \times \vec{H}_s^* + \vec{E}_s \times \vec{H}_i^*\right\}$. Therefore, the interaction of a plane wave with a spherical particle can be characterized by the extinction cross section C_{ext}, the scattering cross section C_{sca}, and the absorption cross section as C_{abs} and they are defined respectively as

$$C_{ext} = \frac{W_{ext}}{I_i}, \tag{2.23}$$

$$C_{sca} = \frac{W_{sca}}{I_i}, \tag{2.24}$$

$$C_{abs} = \frac{W_{abs}}{I_i}, \tag{2.25}$$

and

$$C_{ext} = C_{abs} + C_{sca}, \tag{2.26}$$

where I_i is the incident wave intensity.

If we assume that the incident plane wave is x-polarized and propagating along the z-axis without losing generality, for a homogeneous spherical particle, the scalar wave equation (2.13) can be solved exactly [Bohren and Huffman 1983] with details in Appendix A1, and the scattering cross section C_{sca}, the extinction cross section C_{ext} and the anisotropy parameter g are given in the form of series:

$$C_{sca} = \frac{2\pi}{k^2}\sum_{n=1}^{\infty}(2n+1)\left(|a_n|^2 + |b_n|^2\right), \tag{2.27}$$

$$C_{ext} = \frac{2\pi}{k^2}\sum_{n=1}^{\infty}(2n+1)\,\mathrm{Re}\{a_n + b_n\}, \tag{2.28}$$

$$\begin{aligned} g &= \langle\cos\theta\rangle \\ &= \frac{4\pi}{k^2 C_{sca}}\left[\sum_n \frac{n(n+2)}{n+1}\mathrm{Re}\{a_n a_{n+1}^* + b_n b_{n+1}^*\} + \sum_n \frac{2n+1}{n(n+1)}\mathrm{Re}\{a_n b_n^*\}\right], \end{aligned} \tag{2.29}$$

where the expansion coefficients a_n and b_n are given in appendix A. The numerical values of these cross sections were obtained from MIETAB that is available as a public domain software and has been validated (http://www.zianet.com/damila/freestuf.htm).

2.2.2 The Mie Theory for an Absorbing Host Medium

When the medium within which the sphere is immersed is nonabsorptive to the incident wave, the effect of the host medium is simply to reduce the complex refractive index of the spherical particle by a factor of the refractive index of the medium. The scattering properties such as the scattering cross section C_{sca}, the absorption cross section C_{abs}, and the extinction cross section C_{ext} calculated at the sphere's surface (i.e., the near field) are identical to that calculated in the radiation zone (i.e., the far field).

However, when the host medium is absorptive to the incident wave, the effect of the host medium absorption on the prediction of light scattering by the spherical particle requires thorough consideration. Different types of C_{sca} have been employed and discussed in previous studies [Chylek 1997, Fu and Sun 2001, Yang et al 2002]. An inherent scattering cross-section can be defined in the near-field, i.e., at the sphere's surface, of the scattered light while an apparent scattering cross-section can be derived from the asymptotic form of the scattered light fields in the far-field or the radiation zone where light measurements are carried out. As Yang et al [2002] have pointed out, the scattered wave when leave the particle and travel within the absorbing medium will suffer not only attenuation in magnitude but also modulation of the wave modes when reaching the radiation zone. The form of the scattering cross section used to determine the scattering properties in the far field needs careful examination. The inherent scattering cross section, will couple the medium's absorption in an inseparable way in the radiation zone that it can't correctly predict the experimental observations in the far field. The apparent scattering cross section, which is calculated from the asymptotic form of the scattering waves in the far field, will be the proper definition of the scattering cross section for the radiation transfer calculations. On the other hand, the inherent absorption cross-section is assumed identical to its apparent part, which is defined in the same way as the scattering cross section.

For a plane incident wave with a x-polarization propagating within an absorptive medium of the complex refractive index N_0

$$N_0 = N_{0r} + iN_{0i} \tag{2.30}$$

the apparent scattering cross section C'_{sca} is given by

$$C'_{sca} = \frac{2\pi \exp(-2N_{0i}k_0R_a)}{|N_0|^2 k_0^2} \sum_{n=1}^{\infty} (2n+1)\left(|a_n|^2 + |b_n|^2\right) \tag{2.31}$$

where $k_0 = \omega / c$ and c is the speed of light in vacuum and R_a is the radius of the spherical particle.

Therefore, for spherical particles system of particle number concentration C_0 within an absorptive medium, in the far field, the absorption coefficient μ_a is given by

$$\mu_a = C_0 \times C_{abs} + \frac{4\pi N_{0i}}{\lambda} \tag{2.32}$$

and the scattering coefficient μ_s is given by, as suggested by Yang et al [2002],

$$\mu_s = C_0 \times C'_{sca} \times \exp(2N_{0i}k_0R_a) \tag{2.33}$$

where C_{abs} is the absorption cross section, its expression can be found in Appendix A; λ is the wavelength of the incident wave in vacuum.

The effect of water absorption is vividly illustrated in Fig 2.2 on the inverse determination of the imaginary refractive index n_i of polystyrene. In the weak water absorption region like 1000nm, the value of n_i inversely determined with the water absorption being taken into account (squares in Fig.2.2) is identical to one inversely determined without considering the water absorption (circles in Fig 2.2) within the experimental error. However, within the water absorption region around 1450nm, significant difference shows in the inversely determined values of n_i.

2.3 The Radiation Transport Theory

Understanding the propagations of light in turbid mediums is essential to many applications in medicine. In contrast to the classical electrodynamic theory, the radiation transport theory [Chandrasekhar 1950] is based on the energy conservation law to describe light energy or intensity transportation. With this simplified picture, understanding light distribution at the macroscopic scales, much larger than the wavelength, becomes possible and, therefore, it has been widely adopted to model light propagation and distribution in turbid media in general and in tissue optics in particular.

Three parameters are used to describe an energy transportation process: the absorption coefficient μ_a, the scattering coefficient μ_s, and the scattering phase function $p(\hat{s}, \hat{s}')$. In this dissertation research we will take further simplifications to assume that a particular type of skin tissue, such as epidermis or dermis, can be modeled as a homogeneous turbid medium so that the μ_a and μ_s can be treated as constants and $p(\hat{s}, \hat{s}')$ can be approximated by a Henyey-Greenstein function [Henyey and Greenstein 1941] characterized with a single parameter of anisotropy factor g.

The radiation transport theory equates $\hat{s}$-component of the gradient of radiance $L(\vec{r}, \hat{s})$, which is energy flow rate per unit area and solid angle at position $\vec{r}$ in direction

$\hat{s}$, to the losses due to absorption and scattering and the gains due to lights scattered from all other directions $\hat{s}'$ into direction $\hat{s}$ and light sources:

$$\hat{s}\cdot\nabla L(\vec{r},\hat{s}) = -\left(\mu_a + \mu_s\right) L(\vec{r},\hat{s}) + \mu_s \int_{4\pi} p(\hat{s},\hat{s}') L(\vec{r},\hat{s}') d\omega' + S(\vec{r},\hat{s}) \qquad (2.34)$$

where μ_a is the absorption coefficient, μ_s is the scattering coefficient, $\mu_t = \mu_a + \mu_s$ is called the attenuation coefficient, $S(\vec{r},\hat{s})$ is the light power generated by external sources per unit area and solid angle at position $\vec{r}$ in direction $\hat{s}$. The scattering phase function $p(\hat{s},\hat{s}')$ is the possibility of a photon being scattered from the direction of $\hat{s}'$ into the direction $\hat{s}$ and thus satisfies

$$\int_{4\pi} p(\hat{s},\hat{s}') d\omega = 1 \qquad (2.35)$$

Generally it is assumed that the light scattering under study is of axial symmetry. Therefore, the phase function $p(\hat{s},\hat{s}')$ is only a function of the angle θ between $\hat{s}$ and $\hat{s}'$. The anisotropy factor g is defined as the mean cosine of the scattering angle:

$$g = \int_{4\pi} p(\hat{s}\cdot\hat{s}')(\hat{s}\cdot\hat{s}') d\omega' = \int_{4\pi} p(\hat{s}\cdot\hat{s}') \cos\theta d\omega' \qquad (2.36)$$

which is a measure of deviation of the scattered light distribution from the incident direction. The cases of g = 1, 0, -1 correspond to the completely forward scattering, isotropic scattering, and completely backscattering.

The radiance within a turbid medium such as the skin tissue can be separated into a direct component $L_p(\vec{r},\hat{s})$, which is the 'left-over' portion of the incident light without being absorbed and scattered, and a scattering component $L_s(\vec{r},\hat{s})$:

$$L(\vec{r},\hat{s}) = L_p(\vec{r},\hat{s}) + L_s(\vec{r},\hat{s}) \tag{2.37}$$

The incident light suffers energy loss by the medium absorption and scattering. The irradiance of the incident light will decay exponentially in tissue:

$$E(\vec{r},\hat{s}_0) = E_0(\vec{r},\hat{s}_0)\exp(-\mu_t \ell) \tag{2.38}$$

where $E_0(\vec{r},\hat{s}_0)$ is the irradiance at position $\vec{r}$ in the absence of tissue attenuation, $\hat{s}_0$ is the propagation direction of the incident light at position $\vec{r}$, and ℓ is the distance the incident light traveled in tissue before it reach position $\vec{r}$. After a portion of the incident light experience its first scattering in tissue, it will be removed from L_p to L_s. If we assume no other light sources inside tissue, the scattered radiance results from the incident light. Therefore, we can treat the direct component of the incident light as the source of the scattered radiance in tissue after its first scattering events. The probability of photon traveling in the direction $\hat{s}_0$ being scattered into the direction $\hat{s}$ is equal to $\mu_s p(\hat{s}\cdot\hat{s}_0)$. Therefore, the direct component $L_p(\vec{r},\hat{s})$ can be written as

$$L_p(\vec{r},\hat{s}) = E(\vec{r},\hat{s}_0)\delta(1-\hat{s}\cdot\hat{s}_0)/(2\pi) \tag{2.39}$$

where function δ is the Dirac function. The direct component $L_p(\vec{r},\hat{s})$ vanishes except in the direction $\hat{s}=\hat{s}_0$. On the incident direction $\hat{s}_0$, Beer's law can be expressed as

$$\hat{s}\cdot\nabla L_p(\vec{r},\hat{s}) = -\mu_t L_p(\vec{r},\hat{s}) \tag{2.40}$$

Substituting Eq. (2.37), (2.39), and (2.40) into the radiation transfer equation Eq. (2.34), we have

$$\hat{s}\cdot\nabla L_s(\vec{r},\hat{s}) + \mu_t L_s(\vec{r},\hat{s}) = \mu_s \int_{4\pi} p(\hat{s},\hat{s}')L_s(\vec{r},\hat{s}')d\omega' + \mu_s p(\hat{s},\hat{s}_0)E(\vec{r},\hat{s}_0) \tag{2.41}$$

The source term in Eq. (2.41), the transfer equation for the scattering component $L_s(\vec{r},\hat{s})$ comes from

$$\begin{aligned} S(\vec{r},\hat{s}) &= \int_{4\pi} \mu_s p(\hat{s},\hat{s}_0) L_p(\vec{r},\hat{s}')\,d\omega' = \mu_s E(\vec{r},\hat{s}_0)\int_{4\pi} p(\hat{s},\hat{s}')\,\delta(1-\hat{s}'\cdot\hat{s}_0)\frac{d\omega'}{2\pi} \\ &= \mu_s E(\vec{r},\hat{s}_0)\,p(\hat{s}\cdot\hat{s}_0) \end{aligned} \tag{2.42}$$

The net energy flux vector $\vec{F}(\vec{r})$, which is a measure of the net scattered energy flow at position $\vec{r}$, is defined by

$$\vec{F}(\vec{r}) = \int_{4\pi} L_s(\vec{r},\hat{s})\hat{s}\,d\omega \tag{2.43}$$

For an arbitrary direction $\hat{n}$, the scattered energy traveling in the positive and negative directions of $\hat{n}$ are defined by the hemispherical energy fluxes

$$F_{n+}(\vec{r}) = \int_{\hat{s}\cdot\hat{n}>0} L_s(\vec{r},\hat{s})(\hat{s}\cdot\hat{n})d\omega \tag{2.44}$$

$$F_{n-}(\vec{r}) = -\int_{\hat{s}\cdot\hat{n}<0} L_s(\vec{r},\hat{s})(\hat{s}\cdot\hat{n})d\omega \tag{2.45}$$

$\vec{F}_{n+}(\vec{r})$ and $\vec{F}_{n-}(\vec{r})$ are used here to calculate energies being reflected and transmitted by tissue.

2.3.1 The Diffusion Approximation

The scattered radiance $L_s(\vec{r},\hat{s})$ can be expanded in a series of Legendre polynomials. Taking only the first two terms is often called the P1 approximation of diffusion model [Jackson 1962]:

$$L_s(\vec{r},\hat{s}) = L_0(\vec{r}) + \frac{3}{4\pi}\vec{F}(\vec{r})\cdot\hat{s} \tag{2.46}$$

where $L_0(\vec{r})$ is a constant at position $\vec{r}$ and $\vec{F}(\vec{r})$ is the net energy flux vector defined by Eq. (2.41). Under the diffusion approximation, the radiant transport equation Eq. (2.40) can be transformed into two equations:

$$\nabla\cdot\vec{F}(\vec{r}) = -\mu_a\phi_s(\vec{r}) + \mu_s E(\vec{r},\hat{s}_0) \tag{2.47}$$

$$\vec{F}(\vec{r}) = -\frac{1}{3\mu_{tr}}\nabla\phi_s(\vec{r}) + \frac{\mu_s g}{\mu_{tr}}E(\vec{r},\hat{s}_0)\hat{s}_0 \tag{2.48}$$

where $\mu_{tr} = \mu_t - \mu_s g = \mu_a + (1-g)\mu_s$ is often called the transport attenuation coefficient and the fluence rate $\phi_s(\vec{r})$ is defined as

$$\phi_s(\vec{r}) = \int_{4\pi} L_s(\vec{r},\hat{s})\,d\omega \qquad (2.49)$$

Integrating Eq. (2.44) over the 4π solid angle, we can find

$$\phi_s(\vec{r}) = \int_{4\pi} L_s(\vec{r},\hat{s})\,d\omega = 4\pi L_0(\vec{r}) \qquad (2.50)$$

Substituting Eq. (2.44) into Eqs. (2.42) and (2.43) gives

$$F_{n+}(\vec{r}) = \pi L_0(\vec{r}) + \frac{\vec{F}(\vec{r})\cdot\hat{n}}{2} \qquad (2.51)$$

$$F_{n-}(\vec{r}) = \pi L_0(\vec{r}) - \frac{\vec{F}(\vec{r})\cdot\hat{n}}{2} \qquad (2.52)$$

From Eq. (2.49) and Eq. (2.50), we can find

$$\vec{F}(\vec{r})\cdot\hat{n} = F_{n+}(\vec{r}) - F_{n-}(\vec{r}) \qquad (2.53)$$

$$\phi_s(\vec{r}) = 2\left[F_{n+}(\vec{r}) + F_{n-}(\vec{r})\right] \qquad (2.54)$$

2.3.2 Diffusion Theory in Infinite Slab of Finite Thickness with a Wide-Beam Collimated Light

Consider an infinite tissue slab of finite thickness d in the air illuminated perpendicularly by a uniform light E_0 (Fig.2.3). At the air-tissue boundaries, the incident light will experience reflections and refractions. And inside the tissue it will experience absorptions and scatterings. The irradiance of the collimated incident light will have the form $E(z) = (1 - r_{ce}) E_0 \exp(-\mu_t z)$ inside the tissue. Here, r_{ce} represents the specular reflection coefficient for the collimated light at the air-tissue boundary. If assume that the beam size is sufficiently large (wide-beam), the net energy flux vector $\vec{F}(\vec{r})$ will be parallel to the positive z axis inside tissue. Therefore, the radiation transport equations, Eq. (2.45) and (2.46) in one-dimension can be written as with $\hat{n} = \hat{z}$ [Star 1995]

$$\frac{\partial}{\partial z}\left[F_{z+}(z) - F_{z-}(z)\right] = -2\mu_a\left[F_{z+}(z) + F_{z-}(z)\right] + \mu_s E_0 (1 - r_{ce}) \exp(-\mu_t z) \tag{2.55}$$

$$\frac{\partial}{\partial z}\left[F_{z+}(z) + F_{z-}(z)\right] = -\frac{3}{2}\mu_{tr}\left[F_{z+}(z) - F_{z-}(z)\right] + \frac{3}{2} g\mu_s E_0 (1 - r_{ce}) \exp(-\mu_t z) \tag{2.56}$$

It is usually assumed that the hemispherical fluxes F_{z+} and F_{z-} at a refractive index mismatched boundary can be related by a reflection factor r_{21}:

$$r_{21} = -1.44n^2 + 0.71n^{-1} + 0.668 + 0.0636n \tag{2.57}$$

where n is the refractive index of tissue in this case. If we further assume generally that there is no light scattering in the air and all the scatterings happen in tissue, the boundary conditions will be given by:

$$F_{z+}(0) = r_{21}F_{z-}(0) \qquad \text{at} \qquad z = 0 \tag{2.58}$$

$$F_{z-}(d) = r_{21}F_{z+}(d) \qquad \text{at} \qquad z = d \tag{2.59}$$

In order to solve the transport equations [Eqs. (2.53) and (2.54)] with boundary conditions Eqs.(2.56) and (2.57), we firstly make a transformation:

$$F'_{z+}(z) = F_{z+}(z) - r_{21}F_{z-}(z) \tag{2.60}$$

$$F'_{z-}(z) = F_{z-}(z) - r_{21}F_{z+}(z) \tag{2.61}$$

Under this transformation, the transport equations [Eqs. (2.53) and (2.54)] become

$$\frac{1}{1+r_{21}}\frac{\partial}{\partial z}\left[F'_{z+}(z) - F'_{z-}(z)\right]$$
$$= -2\mu_a \frac{1}{1-r_{21}}\left[F'_{z+}(z) + F'_{z-}(z)\right] + \mu_s(1-r_{ce})E_0\exp(-\mu_t z) \tag{2.62}$$

$$\frac{1}{1-r_{21}}\frac{\partial}{\partial z}\left[F'_{z+}(z)+F'_{z-}(z)\right]$$
$$=-\frac{3}{2}\mu_{tr}\frac{1}{1+r_{21}}\left[F'_{z+}(z)-F'_{z-}(z)\right]+\frac{3}{2}g\mu_s(1-r_{ce})E_0\exp(-\mu_t z) \quad (2.63)$$

and the boundary conditions become

$$F'_{z+}(0)=0 \qquad \text{at } z=0 \quad (2.64)$$

$$F'_{z-}(d)=0 \qquad \text{at } z=d \quad (2.65)$$

Solving $F'_{z+}(z)$ and $F'_{z-}(z)$ from Eqs. (2.60) and (2.61) produces

$$\frac{\partial^2}{\partial z^2}F'_{z\pm}(z)-3\mu_a\mu_{tr}F'_{z\pm}(z)+S'_{\pm}\exp(-\mu_t z)=0 \quad (2.66)$$

where

$$S'_{+}=S_{+}-r_{21}S_{-} \quad (2.67)$$

$$S'_{-}=S_{-}-r_{21}S_{+} \quad (2.68)$$

and

$$S_{+}=\frac{\mu_s}{4}\left[(5+9g)\mu_a+5\mu_s\right](1-r_{ce})E_0 \quad (2.69)$$

$$S_- = \frac{\mu_s}{4}\left[(1-3g)\mu_a + \mu_s\right](1-r_{ce})E_0 \tag{2.70}$$

The solutions of Eq. (2.64) have the forms

$$F'_{z+}(z) = A_{++}\exp(\mu_{eff}z) + A_{+-}\exp(-\mu_{eff}z) + A_+\exp(-\mu_t z) \tag{2.71}$$

and

$$F'_{z-}(z) = A_{-+}\exp(\mu_{eff}z) + A_{--}\exp(-\mu_{eff}z) + A_-\exp(-\mu_t z) \tag{2.72}$$

where

$$\mu_{eff} = (3\mu_a\mu_{tr})^{1/2} = \left\{3\mu_a\left[\mu_a + (1-g)\mu_s\right]\right\}^{1/2} \tag{2.73}$$

If Eqs. (2.69) and (2.70) are substituted into Eq. (2.64) , the coefficient of the exponential term $\exp(-\mu_t z)$ will generate

$$A_\pm = -\frac{S'_\pm}{\mu_t^2 - \mu_{eff}^2} \tag{2.74}$$

If Eqs. (2.69) and (2.70) are substituted into Eqs. (2.60) and (2.61), the coefficient of each exponential term will produce the following relations:

$$A_{++} = q' A_{-+} \tag{2.75}$$

$$A_{--} = q' A_{+-} \tag{2.76}$$

where

$$q' = \frac{(\mu_{eff} - 2\mu_a) - r_{21}(\mu_{eff} - 2\mu_a)}{(\mu_{eff} + 2\mu_a) + r_{21}(\mu_{eff} - 2\mu_a)} \tag{2.77}$$

By applying the boundary conditions Eqs. (2.62) and (2.63) to solutions Eqs. (2.69) and (2.70), we have

$$A_{++} + A_{+-} + A_{+} = 0 \tag{2.78}$$

$$A_{-+}\exp(\mu_{eff} d) + A_{--}\exp(-\mu_{eff} d) + A_{-}\exp(-\mu_t d) = 0 \tag{2.79}$$

Combining Eqs. (2.73) and (2.74) with Eqs. (2.76) and (2.77), we can find

$$A_{+-} = \frac{\frac{A_+}{q'}\exp(\mu_{eff} d) - A_{-}\exp(-\mu_t d)}{q'\exp(-\mu_{eff} d) - \frac{1}{q'}\exp(\mu_{eff} d)} \tag{2.80}$$

$$A_{-+} = \frac{-A_{+}\exp(-\mu_{eff} d) + \frac{A_-}{q'}\exp(-\mu_t d)}{q'\exp(-\mu_{eff} d) - \frac{1}{q'}\exp(\mu_{eff} d)} \tag{2.81}$$

According to the transform Eqs. (2.58) and (2.59), the energy flows in the positive and negative direction of z are given by

$$F_{z+}(z) = \frac{1}{1-r_{21}^2}\left[F'_{z+}(z) + r_{21}F'_{z-}(z)\right] \tag{2.82}$$

$$F_{z-}(z) = \frac{1}{1-r_{21}^2}\left[F'_{z-}(z) + r_{21}F'_{z\_}(z)\right] \tag{2.83}$$

Therefore, the reflected energy flow, which is equal to the net energy flux in the negative z direction, is given by

$$R = \left(1-r_{21}\right)F_{z-}\left(0\right) + r_{ce}E_0 \tag{2.84}$$

And the transmitted energy flow, which is equal to the net energy flux in the positive z direction, is given by

$$T = \left(1-r_{21}\right)F_{z+}\left(d\right) + \left(1-r_{ce}\right)^2 E_0 \exp\left(-\mu_t d\right) \tag{2.85}$$

The dependence of transmittance T depicted by Eq. (2.85) on the thickness d contains not only term $\exp\left(-\mu_t \cdot d\right)$, which describes the attenuation of the direct component, but also terms $\exp\left(\mu_{eff} \cdot d\right)$ and $\exp\left(-\mu_{eff} \cdot d\right)$. Therefore, the transmittance T described by Eq. (2.85) will deviate gradually the straight line determined by $\exp\left(-\mu_t \cdot d\right)$ as d increases. As shown in Fig 2.4, dependence of the collimated transmission Tc was determined through Monte Carlo simulations with parameters μ_a = 0.4 mm^{-1}, μ_t = 40 mm^{-1}, and g =0.8. As expected, Tc decays as $\exp\left(-\mu_t \cdot d\right)$ at small d. As d increases, T_c becomes flattened because diffused scatterings. As illustrated in Fig

2.3, a function containing terms $\exp\left(\mu_{eff}\cdot d\right)$, $\exp\left(-\mu_{eff}\cdot d\right)$, and $\exp\left(-\mu_t\cdot d\right)$ precisely predicts the behavior of T_c and correctly extract the parameter of μ_t.

2.4 Diffraction Theory of Confocal Imaging

Confocal optical microscopy has long established itself as a useful tool in biomedical science by sharply increasing the depth resolution of the cross-section images [Wilson 1990]. Taking advantage of viewing only a very small volume near focus of the objective lens through spatial filtering, confocal imaging could be used to realize optical tomography.

In the paraxial region as shown in Fig.2.5, the Kirchhoff's diffraction formula provides an approximate solution to the wave equation for the amplitude of the scalar electromagnetic field in the plane (x_2, y_2) in terms of the distribution in the plane (x_1, y_1) [Born and Wolf 1999]:

$$U_2\left(x_2,y_2\right)=\int\int_{-\infty}^{+\infty}\frac{1}{i\lambda R}U_1\left(x_1,y_1\right)e^{-ikR}dx_1dy_1 \tag{2.86}$$

where k is the wave number, given by $k=2\pi/\lambda$. According to the Fresnel approximation ($z \gg x_1, y_1, x_2, y_2$), we may replace the R in the denominator by z and the R in the exponent by the first two terms in its binomial expansion

$$U_2\left(x_2,y_2\right)=\frac{e^{-ikz}}{i\lambda z}\int\int_{-\infty}^{+\infty}U_1\left(x_1,y_1\right)e^{-\frac{ik}{2z}\left\{\left(x_2-x_1\right)^2+\left(y_2-y_1\right)^2\right\}}dx_1dy_1 \tag{2.87}$$

Furthermore, if we consider the Fraunhofer approximation, given by $z \gg \frac{1}{2}k\left(x_1^2+y_1^2\right)$, we may neglect the terms involving x_1^2 and y_1^2 in Eq. (2.87)

$$U_2\left(x_2,y_2\right)=\frac{e^{-ikz}}{i\lambda z}e^{-\frac{ik}{2z}\left(x_2^2+y_2^2\right)}\int\int_{-\infty}^{+\infty}U_1\left(x_1,y_1\right)e^{\frac{ik}{z}\left(x_1x_2+y_1y_2\right)}dx_1dy_1 \tag{2.88}$$

Considering a thin lens with a focal length f, as shown in Fig. 2.6, satisfying the lens law $\frac{1}{d_1}+\frac{1}{d_2}=\frac{1}{f}$, the image field amplitude U (x_3, y_3) in a plane located behind the lens with a distance d_2 is then given by [Wilson and Sheppard 1984]

$$\begin{aligned}U\left(x_3,y_3\right)=&-\frac{e^{-ikd_1(1+M)}}{\lambda^2 Md_1^2}\iint\int_{-\infty}^{+\infty}\int P\left(x_2,y_2\right)U\left(x_1,y_1\right)\\&\times e^{\frac{-ik}{2d_1}\left(x_1^2+y_1^2\right)}e^{\frac{-ik}{2Md_1}\left(x_3^2+y_3^2\right)}\times e^{\frac{ik}{d_1}\left[x_2\left(x_1+\frac{x_3}{M}\right)+y_2\left(y_1+\frac{y_3}{M}\right)\right]}dx_1dy_1dx_2dy_2\end{aligned} \tag{2.89}$$

where $U(x_1,y_1)$ is the objective field amplitude in a plane at a distance d_1 before the lens, $M=d_2/d_1$ is the magnification of the lens, and $P(x_2,y_2)$ is the pupil function of the lens. For a circular lens of radius a, the pupil function is assumed to have the form:

$$P\left(r\right)=\begin{cases}1 & r\le a\\0 & r>a\end{cases} \tag{2.90}$$

Therefore, we find the image intensity of a point source objective as

$$I(v) = \left|U(x_3, y_3)\right|^2 = \left(\frac{2J_1(v)}{v}\right)^2 \tag{2.91}$$

where J_1 is a first order Bessel function and the normalized coordinate v is given by

$$v = \frac{2\pi}{\lambda} r \sin\alpha \tag{2.92}$$

and r is the coordinate in the image plane, $\sin\alpha = a/d_1$ is the numeric aperture of the lens. The variation of image intensity along the optical axis around the image plane is

$$I(u) = \left[\frac{\sin(u/4)}{u/4}\right]^2 \tag{2.93}$$

with $u \approx kza^2/f^2 \approx 4kz\sin^2(\alpha/2)$ and z is the distance from the image plane.

Now consider a confocal imaging system shown in Fig.2.7. One lens of pupil function $P_1(\xi_1, \eta_1)$ focuses light onto the investigated object of amplitude transmittance $t(x_0,y_0)$; the transmitted radiation is then collected by another lens of pupil function $P_2(\xi_2, \eta_2)$ and focused onto a detector $D(x_2, y_2)$ of constant sensitivity through a pinhole. The field just after passing the object can be written as

$$U_1(x_0, y_0) = h_1(x_0, y_0)\, t(x_0, y_0) \tag{2.94}$$

where the amplitude point spread function h_1 of the lens $P_1(\xi_1, \eta_1)$ is given by

$$h_1(x_0, y_0) = \int\int_{-\infty}^{+\infty} P_1(\xi_1, \eta_1) e^{\frac{ik}{d_1}(\xi_1 x_0 + \eta_1 y_0)} d\xi_1 d\eta_1 \tag{2.95}$$

The field after the lens $P_2(\xi_2, \eta_2)$ can be found by propagating $U_1(x_0, y_0)$ to the (ξ_2, η_2) plane

$$U_2(\xi_2, \eta_2) = \int\int_{-\infty}^{+\infty} U_1(x_0, y_0) e^{\frac{ik}{d_2}(x_0 \xi_2 + y_0 \eta_2)} P_2(\xi_2, \eta_2) dx_0 dy_0 . \tag{2.96}$$

Finally, the field in the detector plane can be obtained as

$$\begin{aligned} U(x_2, y_2) & \\ &= \int\int_{-\infty}^{+\infty} U_2(\xi_2, \eta_2) e^{\frac{ik}{Md_2}(\xi_2 x_2 + \eta_2 y_2)} d\xi_2 d\eta_2 \\ &= \int\int_{-\infty}^{+\infty} h_1(x_0, y_0) t(x_0, y_0) h_2\left(\frac{x_2}{M} + x_0, \frac{y_2}{M} + y_0\right) dx_0 dy_0 \end{aligned} \tag{2.97}$$

where

$$h_2(x, y) = \int\int_{-\infty}^{+\infty} P_2(\xi_2, \eta_2) e^{\frac{ik}{d_2}(\xi_2 x + \eta_2 y)} d\xi_2 d\eta_2 \tag{2.98}$$

and M is the linear magnification of lens $P_2(\xi_2, \eta_2)$.

Therefore, the intensity detected by a point detector $D(x_2, y_2) = \delta(x_2)\delta(y_2)$ is

$$I = \left| \int \int_{-\infty}^{+\infty} h_1(x_0, y_0)\, t(x_0, y_0)\, h_2(x_0, y_0)\, dx_0 dy_0 \right|^2 \tag{2.99}$$

If the two lenses are circular and of equal numerical aperture, the image of a point object is

$$I(v) = \left(\frac{2J_1(v)}{v} \right)^4 \tag{2.100}$$

and the axial intensity varies as

$$I(u) = \left(\frac{\sin(u/4)}{u/4} \right)^4 \tag{2.101}$$

Compare with the conventional lens imaging, Eq. (2.91) and Eq. (2.93), we can see that the confocal image, Eq. (2.100), and (2.101), is dramatically sharpened, as shown in Fig.2.8. And the intensity falls off monotonically away from the image plane.

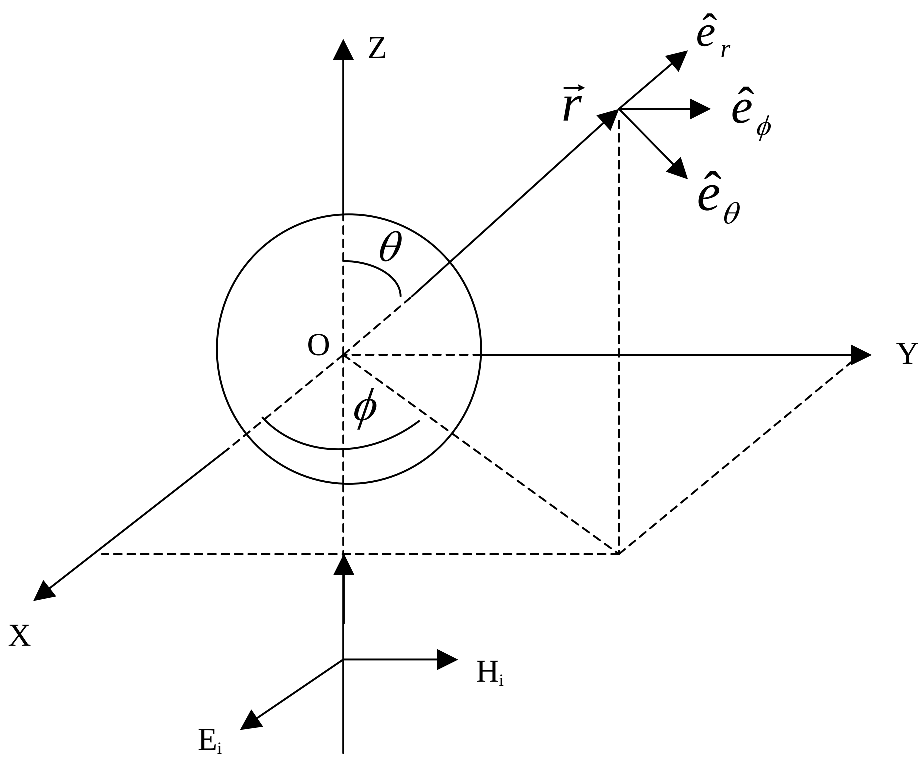

Figure 2.1 Geometry for the scattering of a linearly polarized plane wave by a spherical particle.

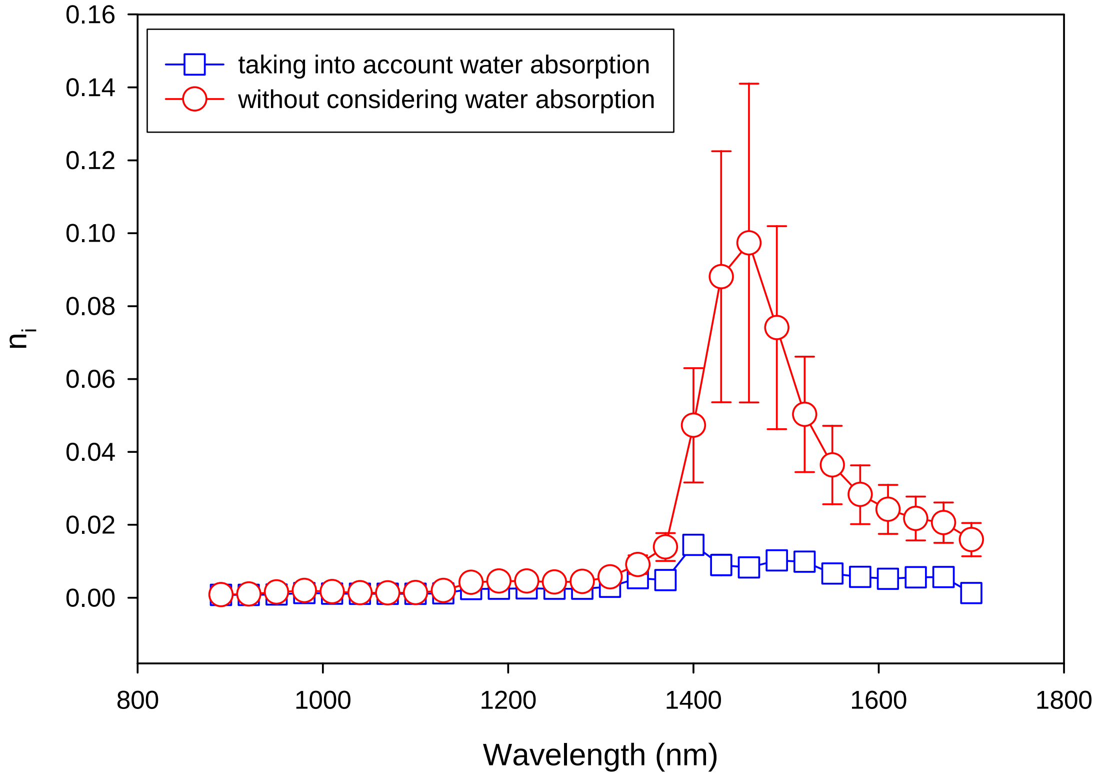

Figure 2.2 Effect of water absorption on the determination of the imaginary refractive index n_i of polystyrene microsphere. Solid lines are for guide of eye.

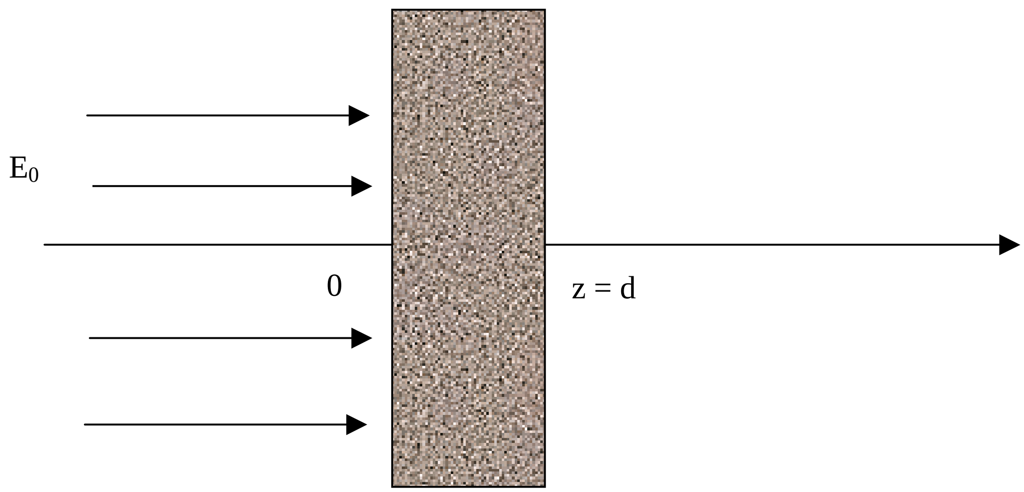

Figure 2.3 Geometry of tissue slab.

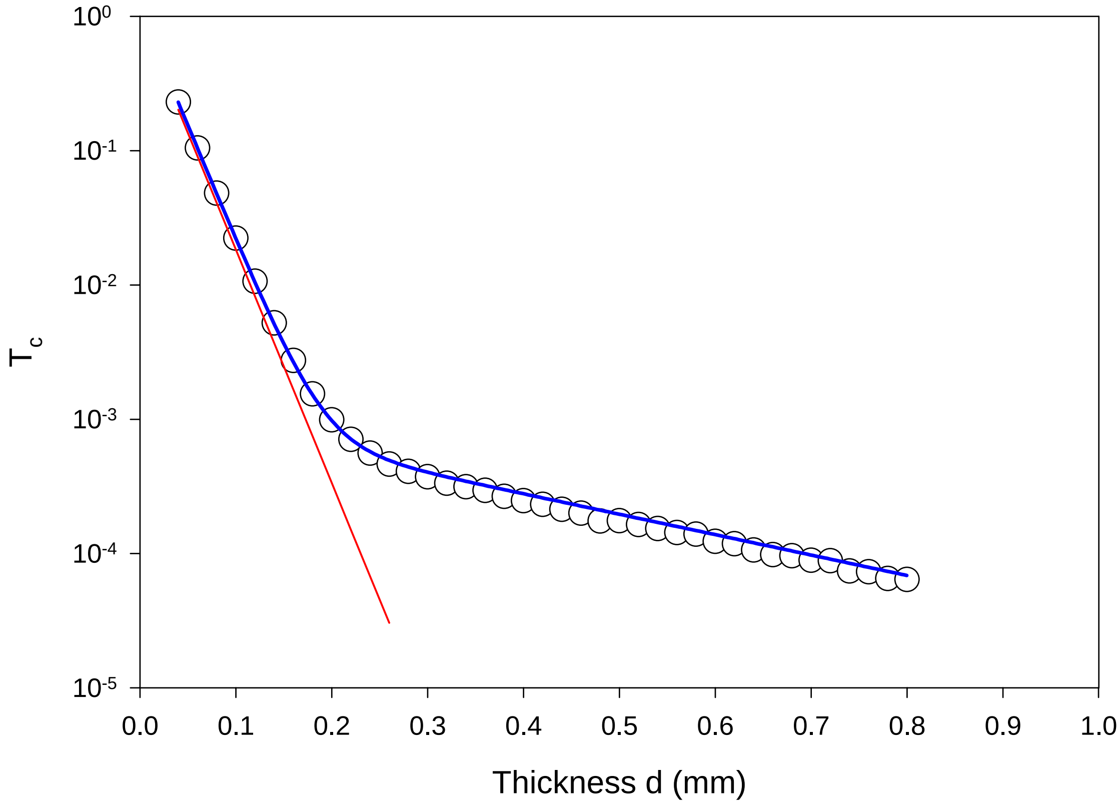

Figure 2.4 Dependence of collimated transmission T_c on thick d. Circles represents Monte Carlo simulated T_c with μ_a = 0.4 mm^{-1}, μ_t = 40 mm^{-1} and g =0.8. The red line shows the decay of $\exp(-\mu_t \cdot d)$. The blue line represents function $y = a \times \exp(\mu_{eff} \cdot d) + b \times \exp(-\mu_{eff} \cdot d) + c \times \exp(-\mu_t^{'} \cdot d)$ with $\mu_{eff} = 3.5\text{mm}^{-1}$ and $\mu_t = 39.4\text{mm}^{-1}$. T_c is plotted in log scale.

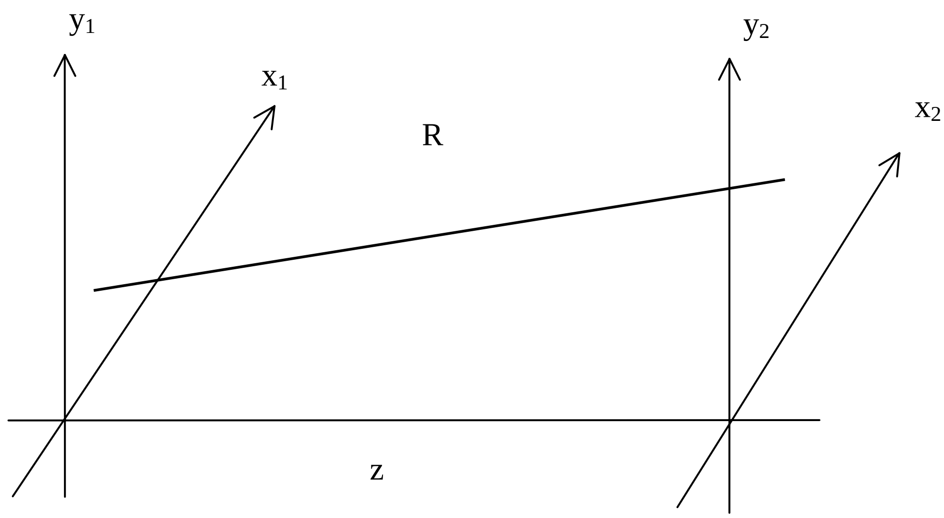

Figure 2.5 Kirchhoff diffraction geometry.

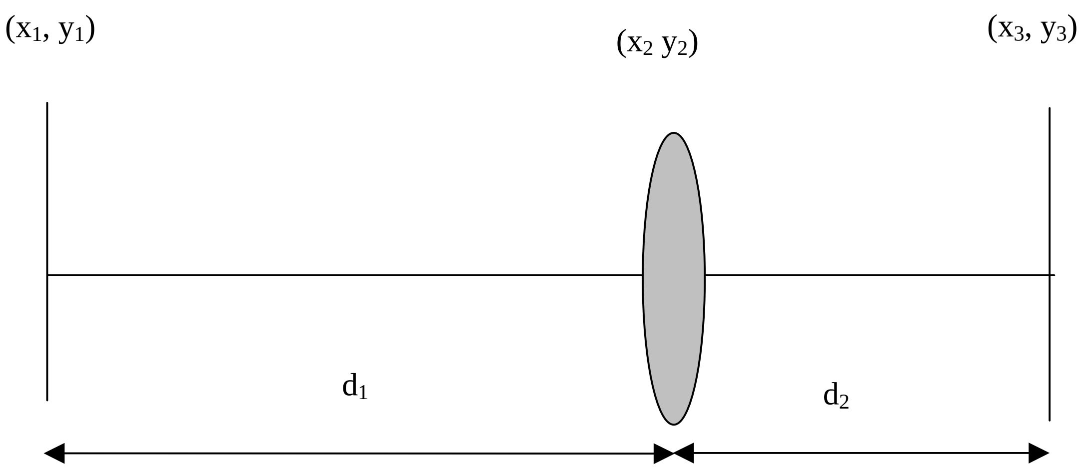

Figure 2.6 Optical imaging by a lens.

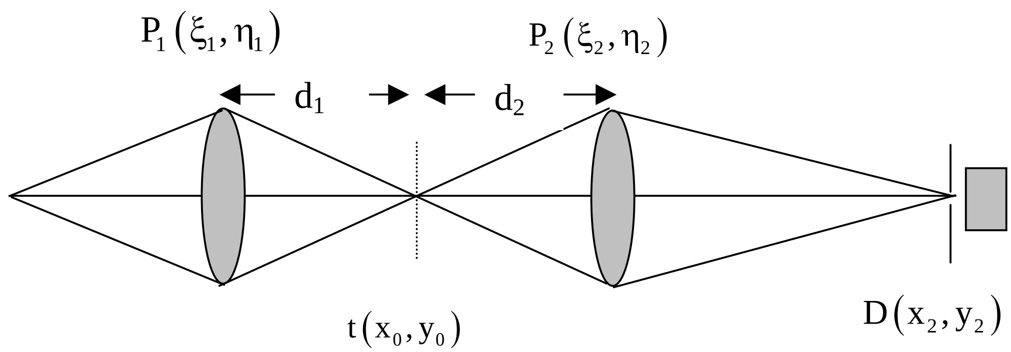

Figure 2.7 Confocal imaging.

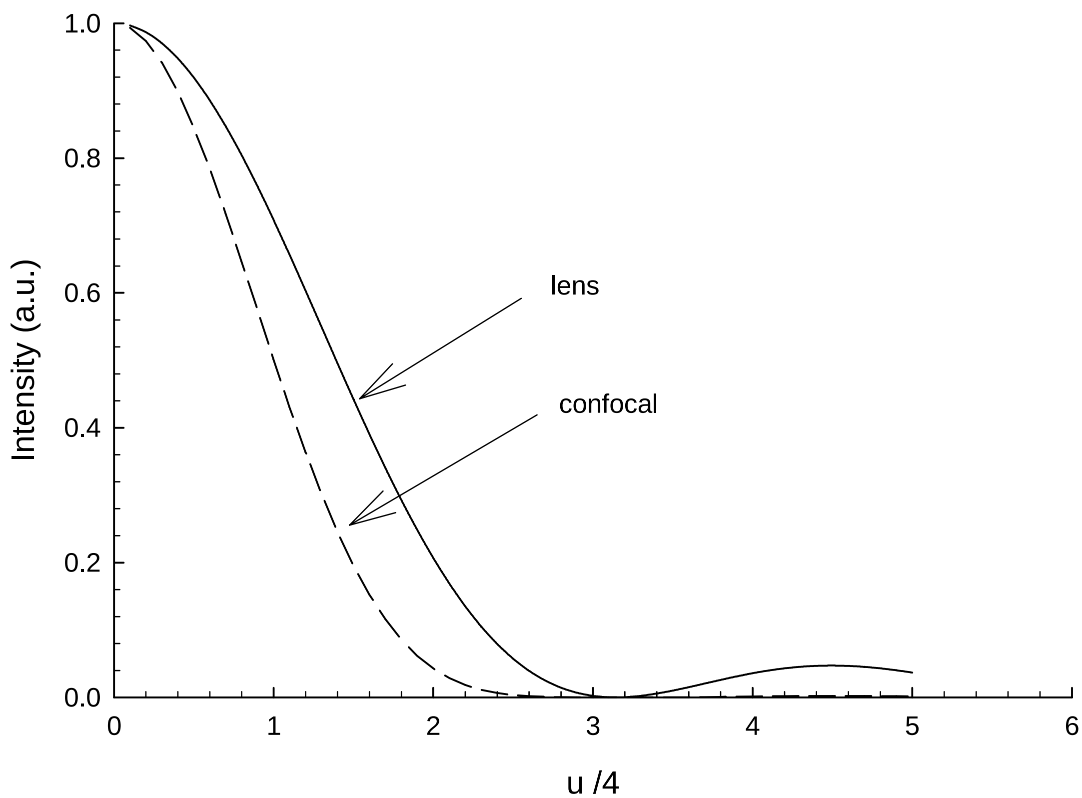

Figure 2.8 Variation of image intensity along the optical axis for conventional lens imaging (solid line) and confocal imaging (dash line).

Chapter 3 Numerical Simulations and Analysis

Numerical simulations of light energy transport in a turbid medium are fundamentally important in many medical applications of light. Because of the complex structures of biological tissues, neither the Maxwell's equations nor the radiation transfer equation can be solved analytically to model light-tissue interaction problems under realistic boundary conditions. However, with light being treated as classical particles of photons without phase information, Monte Carlo simulations offer a statistical and yet vigorous approach toward understanding light distribution distributions within the framework of radiation transfer theory [Wilson and Adams 1983]. In this chapter, we introduce briefly the principle of Monte Carlo simulations and photon tracking algorithms and discuss the inverse methods for determining the optical parameters of turbid samples in vitro and the effect of surface roughness.

3.1 Monte Carlo Simulations

3.1.1 Statistical Treatments of Photon Transportation

Monte Carlo simulation depends on the random sampling of variables from the given probability distributions. Consider a random variable ξ, its probability density function, $p_\xi(\xi)$, defines the distribution of ξ over an interval $a \le \xi \le b$ and satisfies:

$$\int_a^b p_\xi(\xi) d\xi = 1 \tag{3.1}$$

The probability that ξ will fall in the interval $a \le \xi \le \xi_1$ is given by a distribution function, $F_\xi\left(\xi_1\right)$

$$F_\xi\left(\xi_1\right) = \int_a^{\xi_1} p_\xi\left(\xi\right) d\xi \tag{3.2}$$

For a random number ζ generated by the random number generator, its probability density function remains uniform within the interval $0 \le \zeta \le 1$, i.e.,

$$p_\zeta\left(\zeta\right) = 1 \tag{3.3}$$

And the corresponding distribution function $F_\zeta\left(\zeta_1\right)$ is given by

$$F_\zeta\left(\zeta_1\right) = \int_0^{\zeta_1} p_\zeta\left(\zeta\right) d\zeta = \zeta_1 \tag{3.4}$$

The Monte Carlo method is to transform the uniformly distributed random numbers ζ to a unique choice of the random variable ξ that is consistent with the given probability density function $p_\xi\left(\xi\right)$. The key to the Monte Carlo selection of ξ by means of ζ is based on the one-to-one mapping between the two probability distributions. It is recognized [Cashwell and Everett 1959, Kalos and Whitlock 1986] that if Eq. (3.2) is equivalent to Eq. (3.4)

$$\int_a^{\zeta_1} p(\zeta)d\zeta = \zeta_1 = \int_a^{\xi_1} p(\xi)d\xi \tag{3.5}$$

a choice of the evenly distributed random number ζ_1 will determine a unique value ξ_1 from the given probability density function $p_\xi(\xi)$. In general, Eq. (3.5) can be written as

$$\zeta = \int_a^{\xi} p(\xi)d\xi \tag{3.6}$$

The absorption and scattering coefficients are related to the probabilities of a propagating particle being absorbed or scattered per unit of propagation length respectively. This can be realized by requiring the probabilities that a photon being absorbed or scattered in the interval [0,L] as [Keijer et al (1989)]

$$F_{abs}(L) = 1 - \exp(-\mu_a L) \tag{3.7}$$

and

$$F_{sca}(L) = 1 - \exp(-\mu_s L) \tag{3.8}$$

respectively. Therefore, the probability density functions for the absorption and scattering events can be deduced from derivatives of Eq. (3.7) and Eq. (3.8) and expressed as

$$p_{abs}(L) = \mu_a \exp(-\mu_a L) \tag{3.9}$$

$$p_{sca}(L) = \mu_s \exp(-\mu_s L) \tag{3.10}$$

By combining Eq. (3.6) and Eq. (3.10), one can randomly choose a free path length of scattering L_{sca} for a photon between two scattering events using a random number ζ

$$L_{sca} = -\frac{\ln(1-\zeta)}{\mu_s} \tag{3.11}$$

which obeys the given distribution described by Eq.(3.8). Similarly, the total path length of a photon traveled before being absorbed is given by

$$L_{abs} = -\frac{\ln(1-\zeta)}{\mu_a} \tag{3.12}$$

For a scattered photon, its trajectory is deflected by an angle θ in the interval [0, π]. For tissues, the widely adopted probability density function of angle θ, also called phase function, was first proposed by Henyey and Greenstein (1941), and is expressed as

$$p(\cos\theta) = \frac{1-g^2}{2\left(1+g^2-2g\cos\theta\right)} \tag{3.13}$$

where the parameter g is called the anisotropy factor, which is a measure of the asymmetry of scattered light distribution, and is defined by

$$g = \int_0^\pi p(\cos\theta)\cos\theta\sin\theta d\theta \tag{3.14}$$

With the introduction of $\mu = \cos\theta$, Eq. (3.13) becomes

$$p(\mu) = \frac{1-g^2}{2\left(1+g^2-2g\mu\right)} \tag{3.15}$$

By applying Eq. (3.6) to Eq. (3.15), the scattering angle θ can be selected through the random number ζ by

$$\mu = \frac{1}{2g}\left[1 + g^2 - \left(\frac{1 - g^2}{1 - g + 2g\zeta}\right)^2\right] \qquad \text{for } g \neq 0 \qquad (3.16)$$

and

$$\mu = 2\zeta - 1 \qquad \text{for } g = 0 \qquad (3.17)$$

In the above derivations, we assume that the photon deflects symmetrically about the incident direction by an azimuthal angle ψ that uniformly distributes in the interval $[0, 2\pi]$. Based on Eq. (3.6), we have

$$\psi = 2\pi\zeta \qquad (3.18)$$

3.1.2 Photon Tracking Algorithm Based on the Monte Carlo Method

In Monte Carlo simulations, various random processes are used to track the propagation of photons in a turbid tissue. In our model, the tissue sample and holder assembly is simulated as a three-layer structure in which a turbid layer is sandwiched between two transparent layers. The latter simulate the sample holder using two flat window glasses (one is called the entrance window glass, the other is called the exit window glass). The modeled structure is surrounded by air. The turbid layer is modeled as a homogeneous turbid medium with the absorption coefficient μ_a, the scattering coefficient μ_s, and the refractive index as constant. Henyey-Greenstein function is used as the scattering phase function, which is characterized by a single anisotropy factor g. The propagation of a photon inside the turbid medium is simulated as 'random-walk'.

The two window glasses are treated as a uniform medium free of scattering and absorption to every photon. Within a window glass, a photon moves simply from one interface to the other.

Each photon is first injected towards the glass-tissue interface inside the entrance window glass in a way that corresponds to a collimated incident beam. At the glass-tissue interface, Fresnel's equation is used to decide the direction of the tracked photon by comparison of a random number with the reflectivity: if the random number is less than the reflectivity, the tracked photon will move into the tissue; if the random number is bigger than the reflectivity, the photon is reflected back and remain in the window glass. If reflection happens at the glass-tissue interface, the tracked photon will arrive at the glass-air interface. Again at the glass-air interface Fresnel's equation is used to determine whether the tracked photon moves out of the glass and is registered as backward scattering or is reflected back into glass and moves toward the glass-tissue interface and the tracking process will start over again.

Once the tracked photon moves inside the tissue, its total path length L_{abs} is determined from Eq. (3.11), which defines the "life" of this photon in space before being absorbed and the step size L_{sca} for each of its movement is defined by Eq. (3.10). When a scattering event happens, the direction of the tracked photon's movement after scattering is decided by Eq. (3.15), Eq. (3.16) and Eq. (3.17). As the tracked photon reaches the tissue-glass interface, Fresnel's equation will be applied to check if the tracked photon is still within the tissue or moves into the window glass.

During the photon tracking within the tissue, two confinements are checked after each movement. The first checkpoint is the accumulated distance that a photon has traveled. If it exceeds L_{abs}, the photon is designated as absorbed. The second checkpoint is the side limits defined by the turbid layer's lateral dimensions. If a photon moves out of the side limitations, it is registered as leaked or escaped.

For the period that the tracked photon moves within the entrance or exit window glass, Fresnel's equation is applied successively at the glass-air interface or the glass-tissue interface to decide whether the tracked photon still stay within the entrance or exit window glass or moves out into either tissue or the surrounding air. If the tracked photon is found to move out into the surrounding air, it is registered as forward scattering if it moves out from the exit window glass or backward scattering if it moves out from the entrance window glass. As long as the tracked phone travels inside the tissue, the tracking procedure mentioned above for a photon inside the tissue is repeated.

There is only one confinement to check after each movement when the tracked photon stays inside the window glasses. This checkpoint is the side limits defined by the widow glasses' lateral dimensions. If a photon moves out of the side limitations, it is registered as leaked.

3.2 The Role of Phase Function

The implementation of Monte Carlo simulation of light transportation within a turbid medium requires *a priori* knowledge of the scattering phase function.

Unfortunately, structure complexities and the unknown nature of inhomogeneities for most of the turbid media like biomedical tissues make the construction of the real phase functions based on the scattering theory of electromagnetic waves practically impossible. Henyey and Greenstein (1941) proposed the phase function (HG), which approximates the scattering angle distributions calculated from Mie theory, is the most widely adopted form of phase functions to model the photon transport in a turbid medium according to the radiation transfer theory. Van Gemert et al (1989) measured the scattering phase functions of the stratum cornea and epidermis with a goniometer within an angular range from ~0^0 to 60^0. It was found that the HG phase function fits the experimental data plausibly well. However, as was pointed out by Mourant et al (1996), there still exist differences in the curve shapes between the experimental scattering phase function and the HG phase function. Furthermore, measurements on the brain tissue made by Van der Zee et al (1993) showed that the value of the scattering phase function increased at angles greater that 150^0 that is not a feature of the HG phase function. Recently, Kienle et al (2001) discussed the effect of the phase function on determination of the optical parameters by the spatially resolved reflectance. It was indicated that significant differences occurred in the derived reduced scattering and absorption coefficients if different phase functions were utilized in the inverse Monte Carlo simulations.

Aqueous suspension of polystyrene microspheres is one of a few turbid media of which the exact form of phase function is known. Mie theory provides a precise solution to the light interaction with a single sphere. The scattering phase function can be precisely calculated for a sphere with known refractive index, wavelength, and radius.

Therefore, the Monte Carlo simulation of photon distribution within an aqueous suspension of polystyrene microsphere can be carried out using the accurate scattering phase function, instead of the HG phase function.

For an unpolarized incident light, the scattering phase function by a sphere is given by [Bohren et al 1983]

$$p = \frac{1}{2}\left(\left|S_1\right|^2 + \left|S_2\right|^2\right) \tag{3.19}$$

where

$$S_1 = \sum_n \frac{2n+1}{n(n+1)}\left(a_n \pi_n + b_n \tau_n\right) \tag{3.20}$$

$$S_2 = \sum_n \frac{2n+1}{n(n+1)}\left(a_n \tau_n + b_n \pi_n\right) \tag{3.21}$$

and definitions of a_n,b_n, π_n,τ_n can be found in Appendix A.

Even through the value of the Mie phase function at a given scattering angle for a spherical particle can be calculated from Eq. (3.19), it is still mathematically difficult to apply Eq. (3.6) in Monte Carlo simulations. The integral of the Mie phase function, Eq. (3.19), is not feasible to lead to an analytical expression of the scattering angle in a closed form because of the complicated form of Eq. (3.19).

In order to use the exact form of phase function in Monte Carlo simulation of light propagation in polystyrene microsphere suspensions, Toublanc [1996] proposed that a table of Mie's phase function $p_i(\theta)$ versus the scattering angle θ was constructed and normalized by

$$\sum_{i=1}^{N} p_i(\theta) = 1 \tag{3.22}$$

where N is the total number of angles equally divided between 0^0 and 180^0. The scattering angle was then determined by finding an integer m to satisfy

$$\sum_{i=1}^{m-1} p_i(\theta) \langle \mathrm{RND} \le \sum_{i=1}^{m} p_i(\theta) \tag{3.23}$$

where RND is the random number uniformly distributed between 0 and 1, and the left sum is set to zero when m = 1. The number N determines the sampling accuracy and we found that $N = 5000$ was sufficiently large to sample the scattering angle θ with an accuracy of 0.036^0 without significantly slowing down the Monte Carlo simulations.

3.3 The Inverse Method

Let ***S*** be the physical system under investigation. Assume that there exists a set of model parameters whose values completely characterize the system. The forward modeling problem is to find the physical laws that could be used to make predictions on values of some observable parameters from given values of the model parameters. The inverse problem is, on the other hand to use the measured results of the observable parameters to infer the values of the system parameters.

Within the radiation transfer theory, the optical properties of a turbid medium such as tissues are characterized by the scattering coefficient μ_s, the absorption coefficient μ_a and the scattering phase function $p(\vec{s}, \vec{s}\,')$ that describes the probability of light being scattered from a direction $\vec{s}\,'$ to direction $\vec{s}$. Since these parameters cannot be measured directly and analytical solutions of the radiation transfer theory cannot be found for nearly all the practical cases, modeling of tissue optics often has to be achieved statistically through Monte Carlo methods. And multiple Monte Carlo simulations have to be carried out to retrieve inversely the optical parameters of the turbid medium from experimental results.

In order to evaluate the optical properties of tissues, the diffuse reflectance and transmittance, R_d and T_d, and the collimated transmission T_c were measured in this dissertation by the integrating sphere and the spatial filtering respectively. And the Henyey-Greenstein function was adopted as the scattering phase function. Therefore, the distribution of the scattering angles was determined by a single parameter g. The determination of μ_s, μ_a, and g from the measured R_d, T_d, and T_c was realized through the Monte Carlo simulations and optimization iteration using the least-square criterion. Two different Monte Carlo based optimization methods, which correspond to two different procedures to measure R_d, T_d, and T_c were used to find out the optimal optical parameters μ_s, μ_a, and g.

The first Monte Carlo based optimization method used to search for the best possible values of μ_s, μ_a, and g of a turbid medium is used for cases that the measured R_d, T_d, and T_c from the same sample are used as the inputs to the inverse calculations. Consequently, μ_s, μ_a, and g become three free variables for the Monte Carlo optimizations. For any selected μ_s, μ_a, and g, Monte Carlo simulation produces the calculated values of R_d, T_d, and T_c represented here by $(R_d)_{cal}$, $(T_d)_{cal}$, and $(T_c)_{cal}$ respectively. The least-square criterion δ^2 used for optimization iteration is

$$\delta^2 = \left(\frac{(R_d)_{cal} - R_d}{R_d}\right)^2 + \left(\frac{(T_d)_{cal} - T_d}{T_d}\right)^2 + \left(\frac{(T_c)_{cal} - T_c}{T_c}\right)^2 \qquad (3.24)$$

The iteration process for the inverse determination of μ_s, μ_a and g stopped when $\delta^2 \le 4\times10^{-4}$, that corresponds to a relative error of about 1.2% for $(R_d)_{cal}$, $(T_d)_{cal}$ and $(T_c)_{cal}$.

Some rules that can help reduce the number of iteration in searching the optimal values of μ_s, μ_a and g for the current situation are discussed below. Generally speaking, changes in any of μ_s, μ_a and g may induce coupled effects on $(R_d)_{cal}$, $(T_d)_{cal}$ and $(T_c)_{cal}$. When μ_s increases, $(T_c)_{cal}$ will decrease but the ratio of $(R_d)_{cal}$ and $(T_d)_{cal}$ will increase and vice versa. This behavior is being observed in a large range, but exception may occurs when δ^2 is close to 4×10^{-4}. In the vicinity of $\delta^2 \le 4\times10^{-4}$, a slight increase in μ_s may cause $(T_c)_{cal}$ increase. When this happens, the best tactics that is practically observed is to adjust μ_a and g. Increase in μ_s also slightly draw the sum of $(R_d)_{cal}$ and $(T_d)_{cal}$ to increase and vice versa. At the time when g increases, the ratio of $(R_d)_{cal}$ and $(T_d)_{cal}$ will decrease but $(T_c)_{cal}$ tends to increase and vice versa. Few exceptions are observed to this rule. In the meantime, increase in g can lead to changes in the sum of $(R_d)_{cal}$ and $(T_d)_{cal}$, but no preferred tendencies are practically observed. Decrease of μ_a is always the choice to diminish the values of $(R_d)_{cal}$, $(T_d)_{cal}$, and $(T_c)_{cal}$, and vice versa. Meanwhile decrease in μ_a will reduce the ratio of $(R_d)_{cal}$ and $(T_d)_{cal}$, and vice versa.

After a Monte Carlo simulation, it was practically found that to bring the ratio of $(R_d)_{cal}$ and $(T_d)_{cal}$ close to the ratio of the measured R_d and T_d by adjusting g is most profitable to reduce the iteration times. Whence the ratio of $(R_d)_{cal}$ and $(T_d)_{cal}$ is in the close vicinity of the ratio of the measured R_d and T_d, alter μ_a to trim down the difference between the sum of $(R_d)_{cal}$, $(T_d)_{cal}$ and the sum of the measured R_d, T_d. And last vary μ_s to make $(T_c)_{cal}$ close to the measured T_c. As discussed above, the side effects that the change of a parameter may make other parameters' values going back and forth.

The second Monte Carlo based optimization method is suitable for the experimental procedure that the measured values of R_d, T_d and T_c come from different samples. The collimated transmission T_c for samples with different thickness was measured. According to the Lambert-beer's law for the collimated transmission T_c at a fixed wavelength

$$T_c = A\exp\left(-\mu_t D\right) \tag{3.25}$$

where A denotes the loss and deflection of incident light at the surfaces of the tissue sample, the bulk attenuation coefficient μ_t is the slope of the fitted straight line between log (T_c) and sample thickness D. Since μ_t is the sum of the scattering coefficient μ_s and the absorption coefficient μ_a

$$\mu_t = \mu_s + \mu_a \tag{3.26}$$

the free variables for the inverse Monte Carlo simulations are left to only two: μ_a and g. Therefore, the optimization of parameters μ_a, $\mu_s\left(=\mu_t-\mu_a\right)$, and g is achieved through the inverse Monte Carlo simulations with the measured R_d and T_d as additional inputs to minimize the error function δ^2

$$\delta^2 = \left(\frac{\left(R_d\right)_{cal} - R_d}{R_d}\right)^2 + \left(\frac{\left(T_d\right)_{cal} - T_d}{T_d}\right)^2 \tag{3.27}$$

where $\left(R_d\right)_{cal}$ and $\left(T_d\right)_{cal}$ are the calculated diffuse reflectance and transmittance. The iteration process for the inverse determination of μ_s, μ_a and g stopped when $\delta^2 \le 4\times10^{-4}$, that corresponds to a relative error of about 1.4% for $\left(R_d\right)_{cal}$ and $\left(T_d\right)_{cal}$.

The tactics that is practically found to be able to efficiently select the optimal values for μ_s, μ_a and g under the current circumstance is summarized in the following. In general, increase the value of μ_a will decrease the sum of $\left(R_d\right)_{cal}$ and $\left(T_d\right)_{cal}$, increase the value of g will decrease the ratio of $\left(R_d\right)_{cal}$ and $\left(T_d\right)_{cal}$, and vice versa. After the

Monte Carlo simulation for the blind trial of μ_s, μ_a and g, the priority is to choose a value of μ_a that can reduce the difference between the sum of $(R_d)_{cal}$ and $(T_d)_{cal}$ and the sum of the measured R_d and T_d: if the sum of $(R_d)_{cal}$ and $(T_d)_{cal}$ is lager than the sum of the measured R_d and T_d, select a lager μ_a for next run; otherwise choose a smaller μ_a. When the difference between the sum of $(R_d)_{cal}$ and $(T_d)_{cal}$ and the sum of the measured R_d and T_d is less than 0.01, the value of g is being adjusted to bring the ratio of $(R_d)_{cal}$ and $(T_d)_{cal}$ close to the ratio of the measured R_d and T_d. If the ratio of $(R_d)_{cal}$ and $(T_d)_{cal}$ is lager than the ratio of the measured R_d and T_d, a lager g is picked up for the next run; otherwise a smaller one is selected. During the modification of g, the difference between the sum of $(R_d)_{cal}$ and $(T_d)_{cal}$ and the sum of the measured R_d and T_d may go up above 0.01. Once this happens, switch to tune μ_a to bring it down.

3.4 Modeling of Rough Surface in Monte Carlo Simulations

In order to investigate the effect of the surface roughness of the tissue sample used in the optical measurements on the determination of the bulk optical parameters of tissue, the random Gaussian surface model was employed to generate the rough surfaces for modeled tissue samples in the Monte Carlo simulations.

3.4.1 The Random Gaussian Surface Model

A random rough surface can be generated with a collection of the random variables $\left\{\zeta\left(\vec{R}\right)\right\}$ as the surface height. Here, $\vec{R}=(x,y)$ denotes the lateral coordinates of a surface position. At each point $\vec{R}$, surface height $\zeta\left(\vec{R}\right)$ is selected randomly from a set of possible values. Therefore, the collection of variables $\left\{\zeta\left(\vec{R}\right)\right\}$ forms a stochastic process, also called a random process. We first assume that the random process for the surface heights $\left\{\zeta\left(\vec{R}\right)\right\}$ is a wide-sense stationary (WSS) process, which requires that (1) the mean value $\left\langle\zeta\left(\vec{R}\right)\right\rangle$ must be independent of $\vec{R}$ and (2) the correlation $\left\langle\zeta\left(\vec{R}\right)\zeta\left(\vec{R}'\right)\right\rangle$ between two variables, $\zeta\left(\vec{R}\right)$ and $\zeta\left(\vec{R}'\right)$, depends only on the difference $\left(\vec{R}-\vec{R}'\right)$.

Then we further assume that the height distribution function $p(\zeta)$ is a Gaussian distribution function:

$$p(\zeta)=\frac{1}{\delta\sqrt{2\pi}}\exp\left(-\frac{\zeta^2}{2\delta^2}\right) \tag{3.28}$$

and the correlation $\left\langle\zeta\left(\vec{R}\right)\zeta\left(\vec{R}'\right)\right\rangle$ also follows a Gaussian function:

$$\left\langle\zeta\left(\vec{R}\right)\zeta\left(\vec{R}'\right)\right\rangle=\delta^2\exp\left[-\left(\vec{R}-\vec{R}'\right)^2\Big/a^2\right] \tag{3.29}$$

where δ is the root-mean-square (rms) height of the surface roughness and a is the lateral correlation length of the surface roughness describing the average lateral distance between the peak and valley in the surface profile. With choosing

$$\left\langle \zeta\left(\vec{R}\right)\right\rangle = 0 \tag{3.30}$$

the surface height can be expressed as

$$\zeta\left(\vec{R}\right) = \left(2\pi\right)^{-1}\delta\left(\frac{a^2}{16\pi}\right)^{-1/2}\int_{-\infty}^{\infty} X\left(\vec{R}\,'\right)\exp\left[-\frac{2\left(\vec{R}-\vec{R}\,'\right)^2}{a^2}\right]d\vec{R}\,' \tag{3.31}$$

where $X\left(\vec{R}\right)$ is an uncorrelated Gaussian function defined by

$$\left\langle X\left(\vec{R}\right)\right\rangle = 0 \tag{3.32}$$

$$\left\langle X\left(\vec{R}\right)X\left(\vec{R}\,'\right)\right\rangle = \Delta\left(\vec{R}-\vec{R}\,'\right) \tag{3.33}$$

and function $\Delta\left(\vec{R}-\vec{R}\,'\right)$ is the Dirac δ-function. In Eq. (3.29), the surface height is the convolution of $X\left(\vec{R}\right)$ with a Gaussian function $G\left(\vec{R}\right)$ that is defined by

$$G\left(\vec{R}\right) = \delta\left(\frac{a^2}{16\pi}\right)^{-\frac{1}{2}}\exp\left[-\frac{2\vec{R}^2}{a^2}\right] \tag{3.34}$$

If the Fourier transforms of $X\left(\vec{R}\right)$ and $G\left(\vec{R}\right)$ are denoted by $\chi\left(\vec{Q}\right)$ and $g\left(\vec{Q}\right)$ respectively,

$$\chi\left(\vec{Q}\right) = \frac{1}{2\pi}\int X\left(\vec{R}\right)\exp\left(-i\vec{Q}\cdot\vec{R}\right)d\vec{R} \tag{3.35}$$

$$g\left(\vec{Q}\right)=\frac{1}{2\pi}\int G\left(\vec{R}\right)\exp\left(-i\vec{Q}\cdot\vec{R}\right)d\vec{R}=\delta\left(a^{2}\pi\right)^{1/2}\exp\left(-\frac{a^{2}\vec{Q}^{2}}{8}\right) \tag{3.36}$$

we can find, by substituting Eqs. (3.33) and (3.34) into Eq. (3.29),

$$\begin{aligned}\zeta\left(\vec{R}\right)&=\frac{1}{2\pi}\int g\left(\vec{Q}\right)\chi\left(\vec{Q}\right)\exp\left(i\vec{Q}\cdot\vec{R}\right)d\vec{Q}\\&=\frac{\delta a\sqrt{\pi}}{2\pi}\int\exp\left(-\frac{a^{2}\vec{Q}^{2}}{8}\right)\chi\left(\vec{Q}\right)\exp\left(i\vec{Q}\cdot\vec{R}\right)d\vec{Q}\end{aligned} \tag{3.37}$$

3.4.2 Rough Surface Generation

Following the procedure proposed by Maradudin et al (1990) to numerically generate a surface profile, function $\zeta\left(\vec{R}\right)$ is sampled at a set of discrete points: $x_m = m\Delta x$, $y_n = n\Delta y$ with $m,n = 0,\pm 1,\pm 2,\ldots$ where Δx and Δy are the sampling steps along x and y coordinates respectively. Hence, the sampled values of functions $\zeta\left(\vec{R}\right)$, $X\left(\vec{R}\right)$, and $G\left(\vec{R}\right)$ can be expressed as $\zeta_{mn}=\zeta\left(x_m,y_n\right)$, $X_{mn}=X\left(x_m,y_n\right)$, and $G_{mn}=G\left(x_m,y_n\right)$ respectively.

In order to implement Fast Fourier Transform, ζ_{mn}, as well as X_{mn} and G_{mn}, is assumed to be a periodic function of m and n with period 2M and 2N

$$\zeta_{mn}=\zeta_{(m+2M)n}=\zeta_{m(n+2N)} \tag{3.38}$$

Hence, the Fourier transform of $X\left(\vec{R}\right)$ can be written as

$$\chi_{uv} = \frac{1}{2\sqrt{MN}} \sum_{m=-M}^{M-1} \sum_{n=-N}^{N-1} X_{mn} \exp\left[-2\pi i\left(\frac{mu}{2M} + \frac{nv}{2N}\right)\right] \tag{3.39}$$

and the Fourier transform of $G\left(\vec{R}\right)$ can be written as

$$g_{uv} = \frac{1}{2\sqrt{MN}} \sum_{m=-M}^{M-1} \sum_{n=-N}^{N-1} G_{mn} \exp\left[-2\pi i\left(\frac{mu}{2M} + \frac{nv}{2N}\right)\right] \tag{3.40}$$

If now we introduce the representations

$$q_{1u} = \frac{2\pi u}{2M\Delta x} \tag{3.41}$$

$$q_{2v} = \frac{2\pi v}{2N\Delta y} \tag{3.42}$$

Eq. (3.34) can be written as

$$g\left(q_{1u}, q_{2v}\right) = \delta a\sqrt{\pi} \exp\left[-\frac{a^2\left(q_{1u}^2 + q_{2v}^2\right)}{8}\right] \tag{3.43}$$

Therefore, from Eq. (3.35), we have

$$\zeta\left(x_m, y_n\right) = \frac{\delta a\sqrt{\pi}}{2\sqrt{MN\Delta x\Delta y}} \sum_{u=-M}^{M} \sum_{v=-N}^{N} \chi_{uv} \exp\left[-\frac{a^2\left(q_{1u}^2 + q_{2v}^2\right)}{8}\right] \exp\left[i\left(q_{1u}x_m + q_{2v}y_n\right)\right] \tag{3.44}$$

If we express χ_{uv} as

$$\chi_{uv} = \frac{1}{\sqrt{2}}\left(\chi_{uv}^r + i\chi_{uv}^i\right) \tag{3.45}$$

from Eqs. (3.30), (3.31), and (3.37), it follows that $\left\{\chi_{uv}^r\right\}$ and $\left\{\chi_{uv}^i\right\}$ are Gaussian variables with zero mean and a standard deviation of unity, they cab be generated by the

Marsaglia and Bray modification of the Box-Muller transformation of a pair of uniform deviates between zero and one [Stuart and Org 1987].

3.4.3 Method for Surface Statistical Analysis

A scanning confocal microscopy is used to map the surface profile of the sample used for optical measurements. The statistical properties of the rough surface are analyzed by a one-dimensional line surface profile randomly chosen within the two-dimensional surface profile under study.

3.4.3.1 Surface Profile Measurement Using a Confocal Microscope

To measure the surface profile of a tissue sample, a laser scanning confocal microscope (LS510, Zeiss) is used which filters the reflected light spatially to form a 2D image with significantly reduced focal depth at a selected axial position. The unstained porcine skin dermis sample is sandwiched between two glass covers and brought to a position with its rough surface slightly below the focal plane of the microscope objective lens. And this z-position is later used as the reference point for the surface profile reconstruction. An image of 512×512 pixels is taken by scanning the focused laser beam in the x and y direction of the transverse plane with a step size of 0.45 μm and recording the reflected light signal at each scanned position to form an image pixel. Then, the sample is translated one step closer to the focal plane of the microscope objective. Another image is recorded in the same fashion. This imaging procedure is repeated until the sample is translated to the axial position where the lowest point of the sample surface is above the focal plane. The step size of z-scan is preset to be 0.2 μm.

From the set of images acquired at different values of z, the reflected light signals acquired by the confocal microscope can be plotted as a function of z, I(z), for a fixed transverse position of (x, y). According to the confocal imaging model based on diffraction theory, described in Chapter 2, I(z) reaches a maximum value at $z = \zeta$ where the focal plane crosses the tissue sample surface because the index mismatch is maximal. This feature of I(z) provides the mean to determine the height of the sample surface at a transverse position (x, y) and, therefore, the surface profile function $z = \zeta(x, y)$, as shown in Fig3.1. The theory of confocal imaging depicted in Chapter 2 predicts that the reflected light signal decays monotonically at both sides around the image plane along the optical axis for any region being imaged [see Eq. (2.201)] and reaches maximum when the region being imaged is located at the surface where reflection tends to be larger.

The confocal signals recorded in a 12-bit TIFF format correspond to 4096 gray scales. In an attempt to increase the accuracy of surface position determination, at each (x,y) point, the function I(z) is fitted to a Gaussian function. The surface profile function $z = \zeta(x, y)$ is then set to be the center position of the fitted Gauss function at which the maximum I is reached.

3.4.3.2 Surface Profile Statistics

The surface profile function z = $\zeta(x, y)$ measured by using a scanning confocal microscope is a two-dimensional function of the surface height z sampled at evenly spaced intervals along the x and y directions within a finite region of typically $230 \times 230\mu m$

$$\{z_{mn} = \zeta(x = m\tau, y = n\tau)\} \tag{3.46}$$

where $m, n = 0, 1, \ldots, N$ and τ is the transverse sampling interval. To calculate the statistical properties of the rough surface profile, the 'line statistics' method [Stout et al 1985] was adopted here. As shown in Fig 3.2, a one-dimensional surface profile was chosen each time from the two-dimensional surface profile by selection of the surface heights that have the same y value that is randomly selected

$$\{z_i = \zeta(i\tau, y = \text{constant})\} \tag{3.47}$$

The reference position on the z coordinate is chosen randomly during the confocal imaging process. In order to correctly calculate the surface statistical parameters, as pointed out by Bennett and Mattsson (1999), a constant was added to the one-dimensional surface profile so that its mean value equals to zero

$$\sum_{i=0}^{N} z_i = 0 \tag{3.48}$$

The root-mean-square (rms) roughness δ is obtained as the square root of the mean value of the square of the surface height of all the sampled points on the one-dimensional surface profile [Elson and Bennett 1979]

$$\delta = \sqrt{\frac{1}{N+1}\sum_{i=0}^{N} z_i^2} \tag{3.49}$$

To calculate the lateral correlation length *a*, we need to first obtain the autocovariance function $G(w)$ which measures the lateral correlation properties of the surface roughness. And function $G(w)$ can be determined from the one-dimensional surface profile [Elson and Bennet 1979]

$$G(w) = \frac{1}{N+1}\sum_{i=0}^{N-w} z_i \cdot z_{i+w} \qquad w = 0,1,2,\ldots,N-1 \tag{3.50}$$

Here the interval $w \cdot \tau$ is called the lag length. Then the lateral correlation length *a*, also called the autocorrelation length, is determined from the value of the lag length at which the autocovariance function drops to 1/e of its value at zero lag length.

Two additional parameters can be extracted from analysis of the height distribution function. For normal rough surfaces, height distribution functions generally show a Gaussian shape with its maximum at the mean surface level. This can be illustrated by comparison between the height distribution function and a Gaussian function, which is also called the equivalent Gaussian function that has the same under-the-curve area and the same rms roughness as the height distribution function (Fig 4.2).

However, if a rough surface has some special features like large bumps or holes, these large deviation points tend to slightly raise or lower the mean surface level and shift the maximum of the height distribution function below or above the mean surface level (Fig 4.4 and Fig 4.5). Besides, as long as the rms roughness (the second-order height average) is concerned, large deviation points have proportionally more weight than those closer to the mean surface level. Therefore, height distribution function will remarkably deviate from its equivalent Gaussian function (Fig 4.4 and Fig 4.5).

In general, the higher order the height average is made, the more sensitive it is to the surface points lying far from the mean surface level. The skewness is introduced as a third-order measure of the asymmetry of a surface profile about the mean surface level and is defined as [Bennett and Mattsson 1999]

$$\text{Skewness} = \frac{1}{\delta^3}\frac{1}{N}\sum_{i=1}^{N} z_i^3 \tag{3.51}$$

A positive skewness reveals that large deviation points on the rough surface are proportionally above the mean surface level (like bumps) while a negative one shows opposite (like holes, deep scratches).

The kurtosis is a fourth-order description of the peakedness or spikiness of height distribution function of a surface profile relative to Gaussian, and is defined as [Bennett and Mattsson 1999]

$$\text{Kurtosis} = \frac{1}{\delta^4}\frac{1}{N}\sum_{i=1}^{N} z_i^4 \ . \tag{3.52}$$

A perfect Gaussian height distribution function has a kurtosis of 3. When a rough surface contains some special features lying far above or below the mean surface level, the kurtosis will be greater than 3. A kurtosis less than 3 means that the rough surface has proportionally fewer high or low extreme points than a Gaussian.

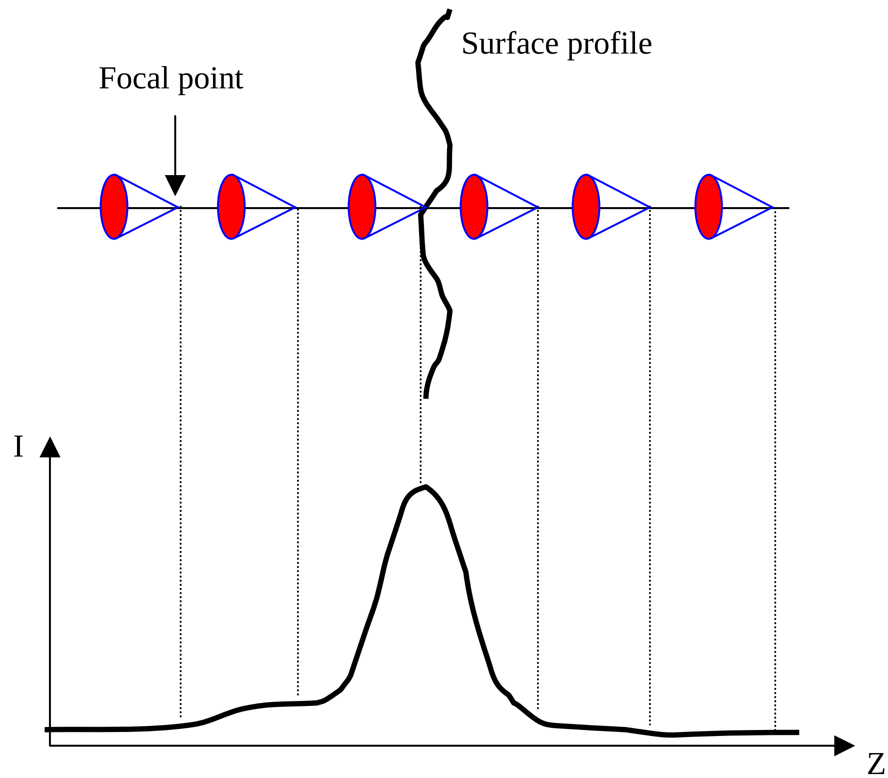

Figure 3.1 The schematic diagram that illustrates the relationship between the reflected light intensity I recorded by a confocal microscope and the focal point position of the confocal microscope relative to the rough surface.

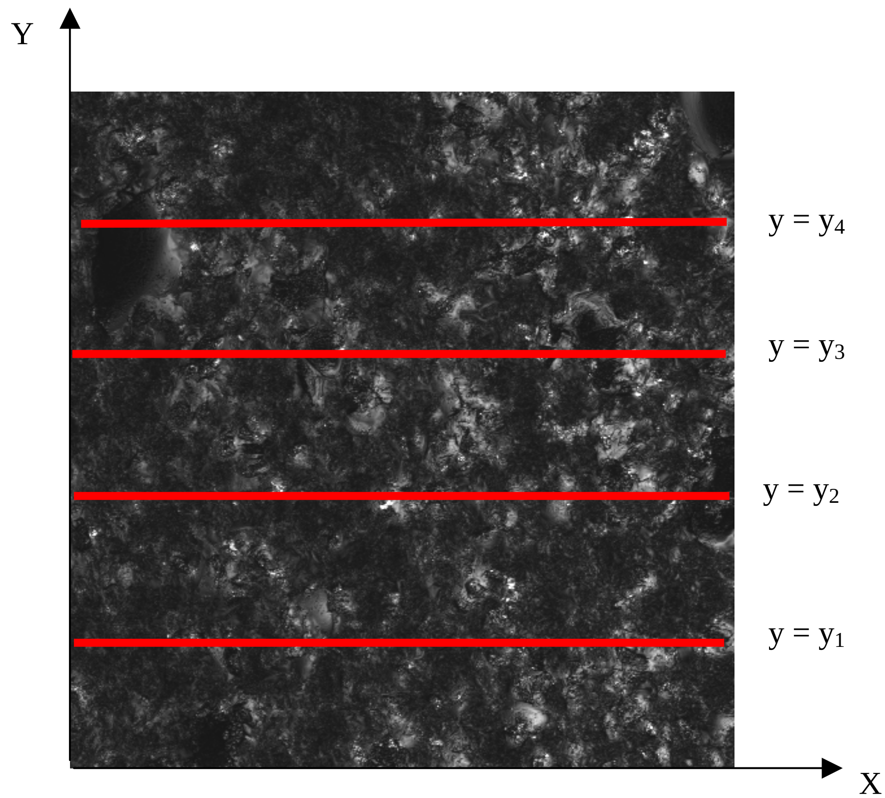

Figure 3.2 The schematic diagram to show how the one-dimensional line surface profiles are chosen to perform the statistical analysis.

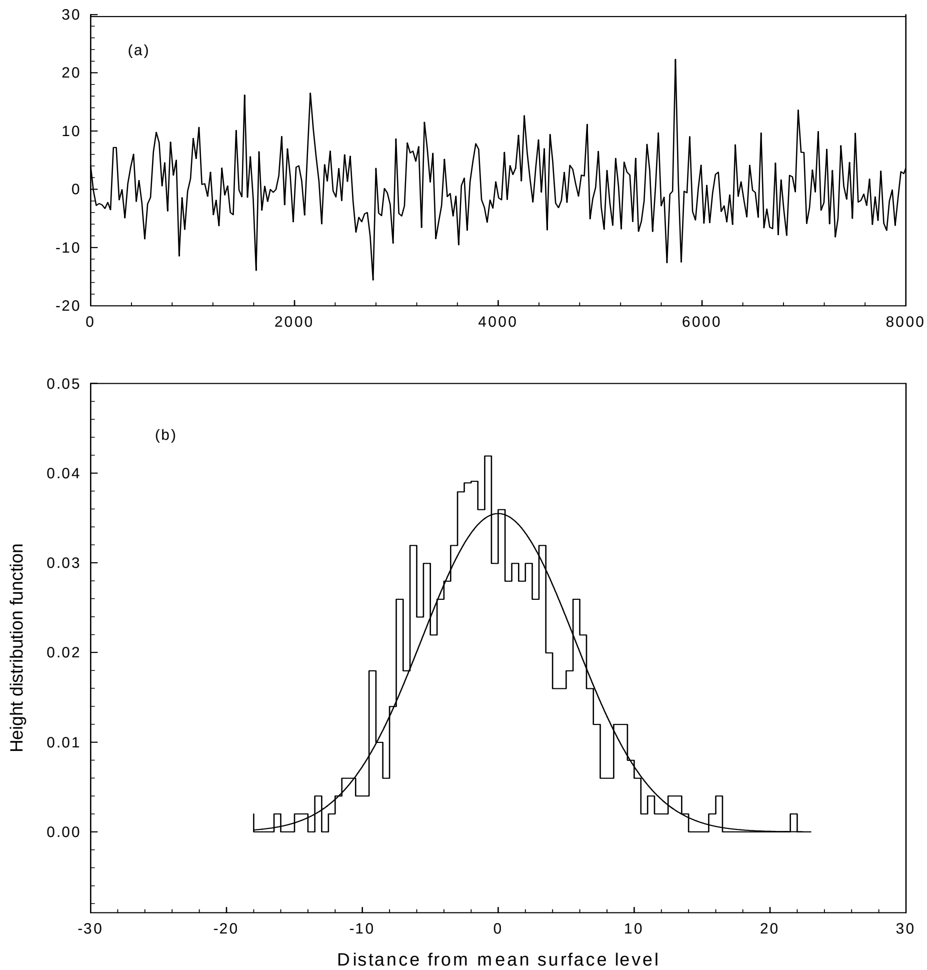

Figure 3.3 Diagraph shows (a) A normal surface profile and (b) Its height distribution function. The smooth curve in (b) is the equivalent Gaussian function.

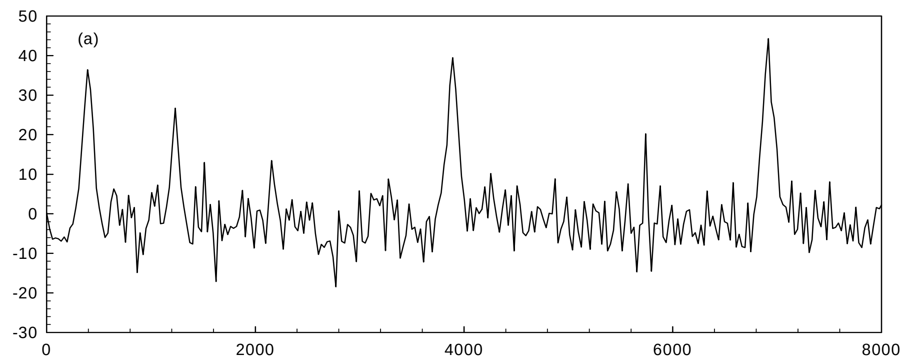

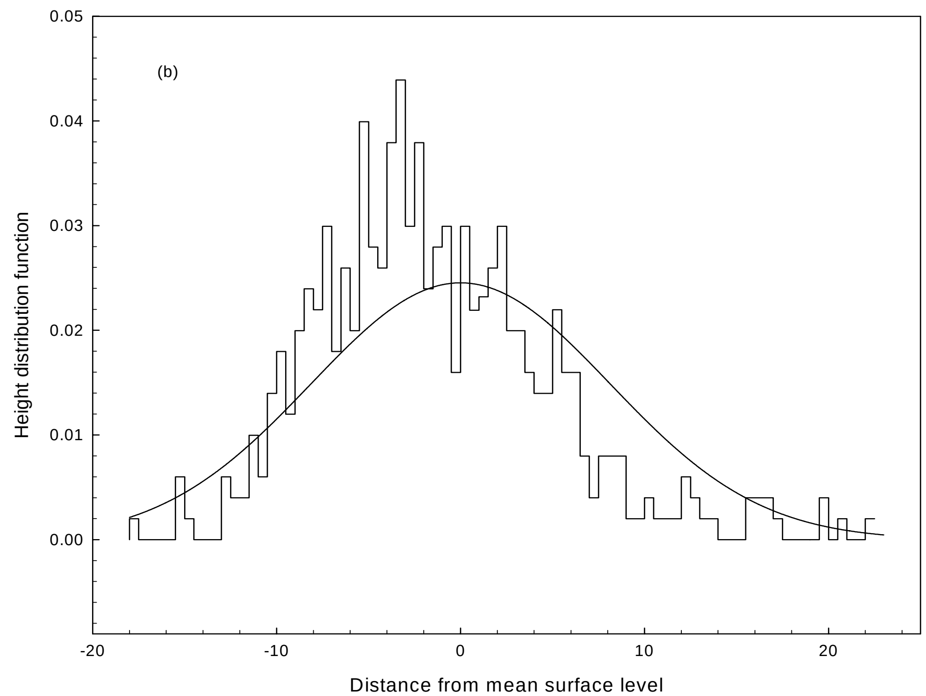

Figure 3.4 (a) A rough surface profile with bumps and (b) Its height distribution function. The smooth curve is the equivalent Gaussian function.

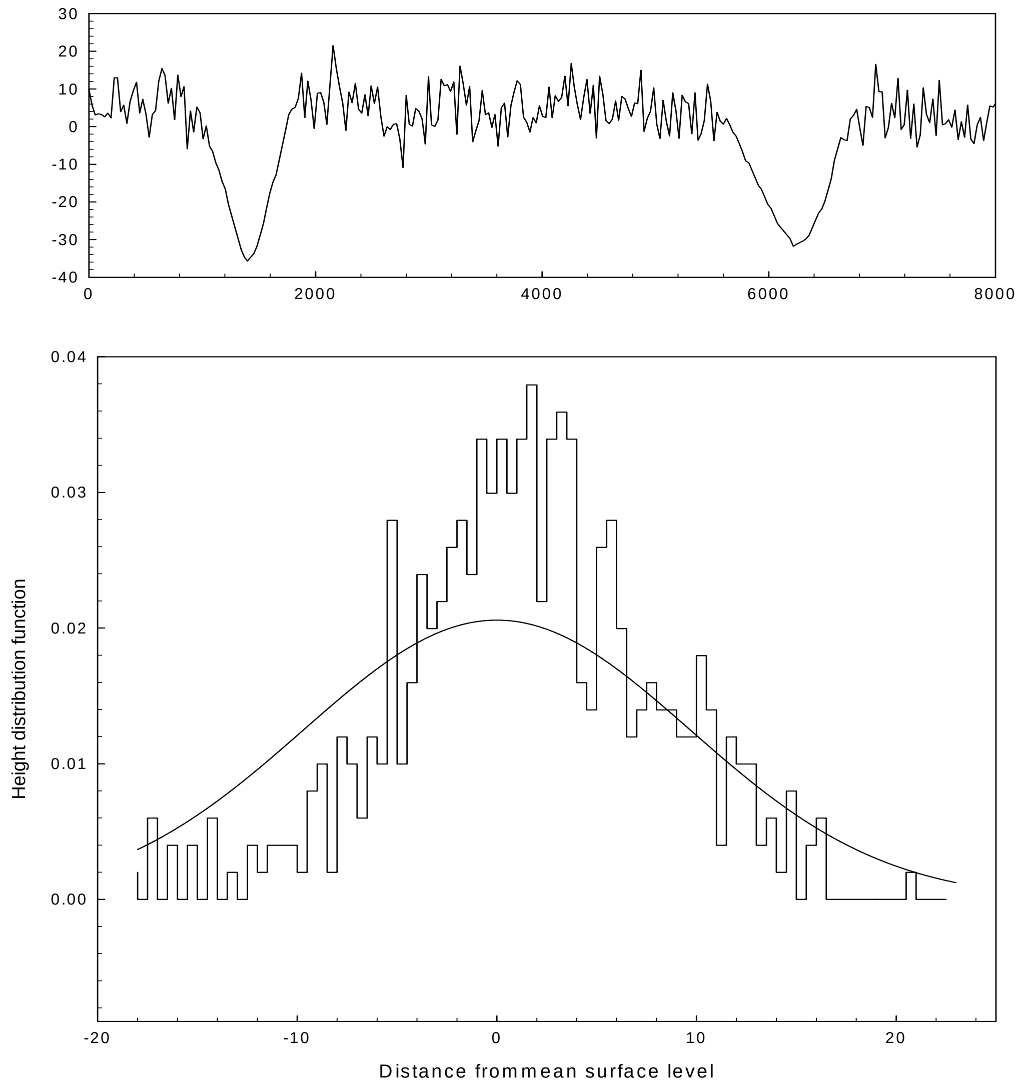

Figure 3.5 (a) A rough surface profile with holes and (b) Its Height distribution function. The smooth curve in (b) is the equivalent Gaussian function.

Chapter 4 Experimental Methods

In this chapter, the experimental designs are presented for the measurements of diffuse reflectance, diffuse transmittance and collimated transmittance for determination of optical parameters of turbid samples. We also describe the methods for preparation of slab skin tissue samples and for determination of surface profile of the samples using a confocal scanning system.

4.1 Methods for Optical Measurement

The response of a turbid sample to light can be measured through its reflectances and transmittances. In principle, the reflected light from the sample can be divided into two parts: a specularly reflected portion that obeys the reflection law and a diffusively reflected portion that emerges from the sample bulk in the backward directions relative to the direction of incident light. The ratio of the reflected radiant flux or radiance integrated over the half space facing the incident surface of the sample to that of the incident light are defined as the specular reflectance R_s for the former and diffused reflectance R_d for the latter. These definitions are useful for slab samples with flat and smooth surfaces since the two portion of the reflected light can be separated from each other by their angular distributions and hence be measured accordingly. The inherent surface roughness of soft tissue samples, however, renders these definitions as useless because the two portions of the reflected light become increasingly mixed with each other as the surface roughness increases and sample thickness decreases. In this dissertation, we define instead the specular reflectance R_s and R_d based on the integrating sphere method that was used for measurements. Experimentally, as shown in Fig 4.1, the diffuse reflectance R_d is determined by dividing the reflected light flux from the turbid sample that does not escape the integrating sphere through the entrance port by that of the incident light.

Likewise, the transmitted light from the sample can also be separated into two components: a collimated fraction that obeys the Beer's law and a diffusively fraction that emerges from the sample in the forward directions relative to the direction of incident light. The ratio of the transmitted radiant flux or radiance integrated over the half space facing the exit surface of the sample to that of the incident light are defined as the collimated transmission T_c for the former and diffused transmittance T_d for the latter. Like their counterparts, R_s and R_d, the above definitions for T_c and T_d are experimentally meaningful for slab samples with flat and smooth surfaces. The collimated light comes out of the sample without being scattered inside the sample bulk and stays in its original track while the diffusively transmitted light tends to have a uniform angular distribution in the forward directions. Therefore, they can be distinguished from each other experimentally. Like the concerns for R_s and R_d, for samples with rough surfaces, the collimated light also increasingly mixes up with the diffusively transmitted light as the surface roughness and the sample thickness increase. In the similar way, the diffuse transmittance T_d is defined as the ratio of the transmitted light flux from the turbid sample that does not escape the integrating sphere through the exit port to the incident light. By contrast, the collimated transmission T_c is defined as the portion of the incident light flux that leaves the integrating sphere through the exit port with a cone angle θ_c

relative to the direction of incident light. θ_c is experimentally decided by the focal length f of the colleting lens and radius r of pinhole (see Fig.4.4 and Fig.4.7)

$$\theta_c = \tan^{-1}\left(\frac{r}{f}\right) \tag{4.1}$$

For a lens of f = 100mm and a pinhole of r =0.05mm, $\theta_c = 5.0 \times 10^{-5}$ rad.

4.1.1 Integrating Sphere Measurements of R_d and T_d

A reflective system has been constructed to measure the diffuse reflectance R_d and the diffuse transmittance T_d of a turbid sample with an integrating sphere of 6 inch in diameter (IS-060-SF, Labsphere Inc.), as shown in Fig 4.2. This system was modified from a previous one with refractive optics (Du et al 2001) by replacing all the lenses with spherical mirrors to eliminate chromatic variation in the system over a wide spectral region. A 1/8 m monochromator of a 2 nm resolution (CM110, CVI Laser) with a 30W tungsten lamp used as a tunable light source to generate a beam with wavelength λ varying from 370 nm to 1610 nm. Two sets of photodiode and low-noise, high-gain preamplifier were constructed and used in two separate spectral regions to detect light signals with a lock-in amplifier (SR830, Stanford Research Systems Inc.): a Si photodiode for $370\text{nm} \le \lambda \le 950\text{nm}$ and a InGaAs photodiode for $920\text{nm} \le \lambda \le 1610\text{nm}$. The light out of the monochromator was modulated at 17 Hz by a chopper (SR540, Stanford Research Systems Inc.). A long-pass filter with the cut-on edge at 540nm in the former region and a long-pass filter with the cut-on edge at 840 nm in the latter region were used to remove the second-order diffraction from the monochromator.

A turbid sample was sandwiched between two window glasses and was placed inside the integrating sphere at its exit port. The diameter of the entrance and exit ports is 6.35 mm. The sample exposure area is of diameter of 14 mm. Three different positions of the integrating sphere were utilized to measure the diffuse reflectance R_d and the diffuse transmittance T_d. To collect the diffuse reflected light signal I_R from the turbid sample, the modulated light was sent into the integrating sphere through its entrance port and was incident normally on the sample (Fig 4.2a). Then the integrating sphere was rotated 180^0 relative to the position for the I_R measurement. The modulated light went into the integrating sphere through its exit port and illuminated the sample and the diffuse transmitted light signal I_T was collected (Fig 4.2b). By placing the integrating sphere 20^0 relative the position for the I_R measurement, the modulated light illuminated a part of the inner wall of the integrating sphere through its entrance port and a reference signal I_0 was recorded (Fig 4.2c). The diffuse reflectance R_d and the diffuse transmittance T_d were calculated from [Du et al 2001]

$$R_d = \frac{I_R \cdot \cos 20^0}{(1-f)\cdot I_0 + \frac{A_s}{A}\cdot I_R \cdot \cos 20^0} \tag{4.2}$$

$$T_d = \frac{R_d \cdot I_T}{I_R} \tag{4.3}$$

where A is the sphere surface area, A_s is the sample exposure area within the integrating sphere, and f is the ratio of the total area of the integrating openings (e.g., the entrance port, the exit port and the detector port) to the sphere surface area A.

The light beam out of the monochromator shows a diverging rectangular shape because of the shape of slit at the output of the monochromator. Practically it was found that one spherical mirror could only make diverged light beam out of the monochromator collimated in the short direction of the rectangle. In the long direction of the rectangle, the light beam was still divergent. Equations (4.2) and (4.3) were derived under the assumption that the incident light was completely collimated. The specular reflection R_c at the first glass-air interface left the integrating sphere through the entrance port completely (Fig 4.3a). However, for a diverged incident light, part of the specular reflection R_c will not escape the integrating sphere through entrance port and make a contribution to light intensity within the integrating sphere (Fig 4.3c). Likewise, as the collimated transmission T_c is concerned, the diverged incident light has the same effect (see Fig 4.3b and Fig 4.3d). By taking into account of effect of the incident beam divergence, the formulas to calculate R_d and T_d is modified as

$$R_d = \frac{I_R \cdot \cos 20^0 - m \cdot R_c \cdot \left(1-f\right) \cdot I_0}{(1-f) \cdot I_0 + \frac{A_s}{A} \cdot I_R \cdot \cos 20^0} \tag{4.4}$$

$$T_d = \frac{\left(R_d + m \cdot R_c\right) \cdot I_T}{I_R} - m' \cdot T_c \tag{4.5}$$

where m represents the fraction of the specular reflection R_c that does not leave the integrating sphere and m' represents the portion of the collimated transmission T_c that does not escape the integrating sphere. For a spherical concave mirror with a radius of 50 mm used to collimate the diverged beam from the monochromator, experimentally we found that at the exit port the light spot extends two times longer in vertical direction while remains unchanged in the horizontal direction by comparison with the light spot size at the entrance port. Therefore, the value of parameter m' is chosen to be 0.5. When the reflected light by the window glass at the exit port reaches the entrance port, it will become three times longer. Hence, the value of m is chosen to be 0.67.

4.1.2 Spatial Filtering for Measurement of T_c

The system constructed to measure the collimated transmission T_c of a turbid medium sample was also based on the reflective optics, see Fig 4.4. A 1/8 m monochromator of a 2 nm resolution (CM110, CVI Laser) with a 30W tungsten lamp used as a tunable light source to generate a beam with wavelength λ varying from 370 nm to 1610 nm. Two sets of photodiode and low-noise, high-gain preamplifier were constructed and used in two separate spectral regions to detect light signals with a lock-in amplifier (SR830, Stanford Research Systems Inc.): a Si photodiode for $370\text{nm} \le \lambda \le 950\text{nm}$ and a InGaAs photodiode for $920\text{nm} \le \lambda \le 1610\text{nm}$. The light out of the monochromator was modulated at 17 Hz by a chopper (SR540, Stanford Research Systems Inc.). A long-pass filter with the cut-on edge at 540nm in the former region and a long-pass filter with the cut-on edge at 840 nm in the latter region were used to remove the second-order diffraction from the monochromator.

A spherical concave mirror with a radius of 100 mm collimated the divergent light beam out of the monochromator. The collimated light emerging out of the turbid sample was collected by a spherical concave mirror of radius of 250 mm and focused on a slit of width of 0.5 mm. The photodiode recorded the light passing through the slit.

A turbid medium sample was sandwiched between two flat window glasses and was exposed to the incident light with a circle area of diameter of 6.35 mm. And the transmitted light I_C was measure behind the slit. A reference light I_0 was measured with only two window glasses exposing to the incident light. Therefore, the collimated transmission T_c of a turbid sample was calculated from

$$T_c = \frac{I_C}{I_0} \tag{4.6}$$

4.1.3 Speckle Effect

The speckle occurs when a coherent light beam is scattered, via reflection or transmission, by a randomly structured sample. The random structure of a sample can be either due to its turbid bulk property or surface roughness, or both, that fluctuates on the order of, or greater than the wavelength of the illuminating light [Francon 1979]. When such a sample is illuminated by a coherent beam, the intensity of the scattered light is found to vary randomly with position – this is known as objective speckle. When a rough surface is illuminated by a coherent light and an image of the surface is formed, the image shows a similar random intensity variation, but in this case the speckle is called subjective. Speckles are caused by the random constructive or destructive interference between the diffuse scatterings of the coherent radiation.

During the measurements of the collimated transmission T_c (see Fig 4.4 and Fig 4.6), speckle effect may significantly change in the spatial distribution of light intensity near the focal point randomly and therefore reduce the repeatability and accuracy of the Tc measurements. The speckle-induced spatial distribution could affect the spatial filtering that is used to measure Tc with a pinhole placed at the focal point of the colleting lens to remove most of the scattered light. This possibility can be investigated by the following method.

Fig 4.5 shows an experimental setup used to investigate the speckle effect under the spatial filtering configuration. A collimated beam from a Nd:YAG laser with a wavelength of 1.064 μm and a diameter of 2.5mm was used to illuminates a rough turbid sample. A convex lens of 100 mm focal length is used to collect the light transmitted through the sample. A pinhole of 1mm diameter is placed at the focal point of the colleting lens and a photodiode detector is positioned right behind the pinhole. The pinhole and the detector were first aligned with incident light beam without the sample. The turbid sample and the detector with the pinhole are mounted on two translation stages, which can be moved in the lateral direction relative to the incident beam. Two measurements were carried out to evaluate the speckle effect on the T_c measurement. The first measurement was to examine how the collimated transmission varies from place to place within the turbid sample. By moving the sample in the lateral direction, the collimated light signals were measured with the pinhole and detector aligned with the incident beam. The second measurement was to probe the light distribution in the focal plane of the signal colleting lens. By moving the detector and its pinhole laterally in the focal plane, the light intensity variations were measured with the position of the illuminated turbid sample unchanged.

4.1.4 Combination of Integrating Sphere and Spatial Filtering Techniques

The collimate-transmitted light signal is usually much weaker than the diffuse reflected or transmitted light signals because of the strong light scatterings by the turbid medium like skin tissues. When R_d and T_d are measured under the experimental configuration described in section 4.1.1 for a typical sample thickness of 0.4 mm, the collimated transmitted light signal was far below the detectable level because of the relative weak light intensity of tungsten lamp used for the monochromator. For example, the diffuse reflectance R_d and the diffuse transmittance T_d for porcine dermis sample with a thickness of 0.4 mm typically have values of 0.11 and 0.40 respectively while its collimated transmission Tc only has a value of 3.7×10^{-5} at a wavelength of 632.8 nm. The collimated light signal is about 10000 times weaker than the diffuse scattered light signals. Therefore, T_c measurement has to be carried out on different samples under the experimental configuration discussed in section 4.1.2 with small thickness typically less than 0.1 mm for skin tissues. For this purpose, skin tissue samples have to be frozen for sectioning and the integrity of a skin tissue sample with thickness under 0.1 mm is significantly reduced in comparison to the thick tissue samples sectioned freshly. Furthermore, the thickness measurements of thin slab tissue samples have larger uncertainty than those of thick samples because of the plasticity of the tissue samples. As a result, the attenuation coefficient μ_t determined from T_c from different thin cryo-sectioned samples have large uncertainty and may not correspond to the Rd and Td measured from thick freshly sectioned samples.

In an attempt to measure R_d, T_d, and T_c from the same sample, we use laser beams to increase the incident light intensity to improve the collimated light signal. Seven lasers are employed to provide CW beams at eight wavelengths: 325 nm and 433 nm from a Cd-He laser (Series 56, Omnichrome), 632.8 nm from a He-Ne laser (05-LHP-143, Melles Groit), 532 nm from a SHG Nd: YAG laser, 1640 nm from a Nd: YAG laser, 855 nm, 1310 nm, and 1550 nm from three diode laser. Fig 4.6 shows the experimental setup. The laser beam was first expanded and collimated to 6mm in diameter through two convex lenses with focal length of 50 mm and 200 mm respectively. Then the expanded laser beam was brought into the integrating sphere. Within the integrating sphere, R_d and T_d were determined the same way as in section 4.1.1. Meanwhile, the collimate-transmitted light signal left the integrating sphere through its exit port and was collected by another convex lens with a focal length of 100 mm and a pinhole of 1 mm in diameter placed at its focal point. The diameter of the entrance and exit ports of the integrating sphere was reduced from 6.35 mm to 3mm. And the diameter of the sample exposure area was reduced from 14 mm to 6mm. The incident light was modulated at 17 Hz by a chopper. The R_d, T_d, and T_c signals were measured with a lock-in amplifier. Fig.4.7 displays schematics of sample holder.

The significance of measuring R_d, T_d, and T_c from the same sample lies in the fact that the inverse Monte Carlo determination of μ_s,μ_a, and g is based on the precise knowledge for a specific sample. In contrast, if only R_d and T_d are measured for a sample, the inverse Monte Carlo determination of μ_s,μ_a, and g based on R_d and T_d has to resort on *a priori* knowledge of μ_t (=μ_s+μ_a), which comes from the average of T_c measurements of many different samples. For a specific sample, the sample-averaged μ_t may not reflect its attenuation accurately. And the inverse Monte Carlo simulations based on Rd, Td and μ_t may end up with a set of μ_s,μ_a, and g with large deviations. Furthermore, for samples with large quality variations, the large uncertainty in μ_t determination may fail the inverse Monte Carlo determination of μ_s,μ_a, and g because the search of μ_s or μ_a limits by μ_t.

4.2 Weak Signal Detection and Data Acquisition

The strong light scattering and absorption within a turbid medium make the experimental investigations often incur weak light signal detections. The technology advance over the recent years has dramatically improved the performance of photodiodes and operational amplifiers. Photodiode, combined with the preamplifier based on the operational amplifier and the lock-in amplifier, provides a solution for the low-noise, high-sensitivity weak signal detection.

4.2.1 High-Gain Preamplifier Design

Si photodiodes (S1336-44BQ, Hamamatsu) were used to detect light signals within the spectral range from 190 nm to 1100 nm and InGaAs photodiodes (FGA10, Thorlabs Inc.) were used to measure light signals within the spectral range from 800 nm to 1800 nm. Table 4.1 lists their characteristic parameters.

The photodiode is operated either in the current source mode without a bias voltage or in the reverse bias mode. The response of the diode has a linear relationship to the light energy received. Fig 4.8 shows the circuit details of the preamplifier [Ronnow and Veszelei 1994]. The output voltage of the amplifier is proportional to the photocurrent from the diode with a gain factor determined by the product of the feedback resistor R_f and M (= R_1/R_2). Here M is an extra gain that is brought up by reducing the feedback voltage through the resistive divider. Under the current selections of resistors, the amplifier produces a total transimpedance gain of 10^{11} (V/A). The cut-off frequency of the low-pass filter at the output end of the amplifier is 50 Hz.

4.2.2 Lock-in Detection Principle

Lock-in amplifier is widely used in research and engineering to detect and measure very small AC signals. Precise measurements can be realized even when the small signal is obscured by noises thousands of times larger. Lock-in amplifier use a technique known as phase-sensitive detection to single out the signal at a specific reference frequency and phase. Noise signals at frequencies other than the reference frequency are rejected and have no effect on the measurement.

For lock-in measurements, a reference frequency is required. Assume that the frequency reference signal is a square wave at frequency ω_r, as shown in Fig 4.9. The signal that we attempt to measure can be modulated at the reference frequency ω_r. Assume further that the modulated signal has the sin waveform: $V_{sig}\sin\left(\omega_r t+\theta_{sig}\right)$ where V_{sig} is its amplitude and θ_{sig} is its phase.

Firstly, the lock-in amplifier utilizes a technique called phase-locked-loop to lock the internal reference oscillator to the frequency reference signal provided to the lock-in amplifier, resulting in a sine wave known as the lock-in reference at frequency ω_r with a fixed phase shift of θ_{ref}: $V_{ref}\sin\left(\omega_r t+\theta_{ref}\right)$ where V_{ref} is the amplitude of the lock-in reference. Secondly, the lock-in amplifier amplifies the modulated signal and multiplies it by the lock-in reference using a phase-sensitive detector (PSD) or multiplier. The result of PSD V_{PSD} is

$$\begin{aligned} V_{PSD} &= V_{sig}\sin\left(\omega_r t+\theta_{sig}\right)\times V_{ref}\sin\left(\omega_r t+\theta_{ref}\right) \\ &= \frac{1}{2}V_{sig}V_{ref}\cos\left(\theta_{sig}-\theta_{ref}\right)-\frac{1}{2}V_{sig}V_{ref}\cos\left(2\omega_r t+\theta_{sig}+\theta_{ref}\right) \end{aligned} \tag{4.7}$$

Thirdly, when PSD output V_{PSD} is passed through a low-pass filter, the AC signal is removed. And the filtered PSD output $\bar{V}_{PSD}$ is

$$\bar{V}_{PSD} = \frac{1}{2} V_{sig} V_{ref} \cos\left(\theta_{sig} - \theta_{ref}\right) \tag{4.8}$$

This is a DC signal proportional to the signal amplitude that we attempt to measure.

Now suppose that the input to the lock-in amplifier is made up of signal plus noise. The PSD and the low-pass filter only detect signals whose frequencies are very close to the reference frequency. Noise signals with frequencies far away from the reference frequency are blocked by the low-pass filter because they are still AC signals after PDS. Noises at frequencies very close to the reference frequency result in very low frequency AC outputs from PSD. Their attenuation depends on the bandwidth of the low-pass filter.

The low-pass filter bandwidth of the lock-in amplifier is determined by setting the time constant on the front panel. The time constant is $1/\left(2\pi f_{cut-off}\right)$ where $f_{cut-off}$ is the –3dB frequency of the low-pass filter. The low-pass filters are 6 dB per octave roll off (also called the slope), RC type filters. The output of the low-pass filter is expected to be a DC signal. Therefore a small time constant that corresponds a narrow bandwidth is desirable. However, the noise signals at the input of the low-pass filter tend to induce more fluctuations on the DC signal with a narrower bandwidth. By increasing the time constant, the output becomes more steady. But the trade-off is the low-pass filter takes a relative long time for a variation in the input signal to be reflected in its output. Typically a single RC filter requires about 5 time constants to settle to its final value. The time constant reflects how slowly the output of low-pass filter responds a change in its input.

There are four successively low-pass filters for each PSD resulting in a roll off or slope from 6 dB up to 24 dB. An increase in the slope can help reduce the time constant needed to reach a stable output of the low-pass filter.

To determine the background noise in a measurement with the lock-in amplifier, we simply block the incident light getting into the measuring system. There is no modulated incident light illuminating the sample. The detector picks up the environmental radiation. For a detector that has a preamplifier with a 10^{10} gain, the lock-in amplifier typically has a reading within 100 μV range and a varied phase angle with a time constant of 300 ms and a slope of 24 dB. When a measurement is performing, the intensity of the modulated light is adjusted so that the lock-in amplifier has a reading above 1 mV and a stable phase angle. Therefore, the signal-to-noise ratio at most of situation is lager than 10.

4.3 Sample Preparation

The optical properties of two types of turbid media were experimentally and theoretically investigated in this dissertation: aqueous suspensions of polystyrene microspheres and the porcine dermis tissue. The preparation techniques are described below.

4.3.1 Skin Tissue Structure

Skin tissue is composed of two major layers: epidermis and dermis (Fig 4.10). The epidermis forms the external surface of the skin and mainly consists of keratinocytes which differentiate to form 4 layers: the Stratum Basale (basal layer), the Stratum Spinosum (prickle or squamous cell layer), the Stratum Granulosum (granular layer), and the Stratum Corneum (corneal layer). The basal layer is the innermost layer of epidermis. This layer houses one layer of small round cells called basal cells. Basal cells attach to the basement membrane which separates the epidermis layer from the underlying dermis layer. These cells constantly divide with the new cells constantly pushing older ones on a migration toward the surface of the skin. The basal layer also contains melanocytes, which produce a pigment called melanin. Above the basal layer is the prickle cell layer. Here lie the basal cells that have been pushed up from the basal layer. These mature basal cells are now called the prickle cells, or keratinocytes. Protein synthesis occurs in this layer, producing a fibrillar protein keratin, a tough, protective protein that makes up of a large part of the structure of the skin, hair, and the nail. Keratin aggregates to form tonofibrils. These tonofibrils migrate into its above layer called the granular layer. In the granular layer, each keratinocyte contains basophilic keratohyalin granules. The protein filaggrin is the major component of these granules. These granules bond to the keratin filaments, which evolved from the tonofibrils to form the keratin complex. Within the outmost layer, the corneal or horny layer, keratinocytes enlarge, flatten, and bond together, then eventually become dehydrated and die. The thickness of epidermis varies between 50 μm and 150 μm [Anderson et al 1981].

Dermis lies beneath epidermis and consists of the dense fibro-elastic connective tissues. Its main components are collagen and elastin. Several structures are also found in the dermis: the sweat glands, the sebaceous glands, nerve endings, hair follicles, blood and lymph vessels. The dermis layer is divided into 2 layers: the papillary dermis and the reticular dermis. The papillary dermis is a thin junction layer immediately beneath epidermis. It is composed of the interlocking rete ridges and dermal papillae. The reticular dermis extends most of dermis. It is mad up mainly of fibrous proteins. Collagen is its main structural component accounting for 70% of the dry weight of skin. Bundles of collagen molecules pack together and are responsible for the skin's strength. Collagen fibers are composed of thinner microfibrils. There are two major types of collagens. Type I collagen fibers are arranged in a dense orthogonal network up to 15 μm wide. Type I collagen microfibrils have a distinctive cross banding with a periodicity of 68 nm. Type III collagen also called reticulin. Another fibrous protein is elastin, which gives skin its elasticity. Elastin fibers constitute about 3% of the dry weight of the skin. A variety of cells are scattered inside the dermis. These cells are fibroblasts (synthesize collagens and elastin), histiocytes, mast cells, lymphocytes, Langerhan's cells. In average, the dermis is about 3 mm thick. Underneath the dermis, there is a subcutaneous layer or hypodermis, which contains mainly the adipose (fat) tissues. It acts as a protective cushion to the skin.

4.3.2 Porcine Dermis Sample Preparation

Porcine skin has a structure that shows the closest similarity to that of the human skin among mammals and has been widely used as the model of human skin [Lavker et al 1991]. Large patches of full-thickness skin (about 10cm by 10cm) were removed from the back of the neck of 6-month-old white domestic pigs at the Department of Comparative Medicine, Brody School of Medicine, East Carolina University after the animals were sacrificed for medical classes. Immediately after the removal from the animal, the skin tissue was kept within the crushed ices in an ice bucket. And the ice bucket was stored in a refrigerator with the temperature maintained around 2^0 C to 4^0 C.

Two methods were employed to obtain the porcine dermis samples: fresh tissue sectioning and frozen tissue sectioning. For the fresh tissue sectioning, a 20 mm square of porcine skin tissue was glued (super glue or cyanoacrylate) on a specially designed microtome on its epidermis at room temperature. The dermis samples were sectioned with a small razor blade and the thicknesses of sectioned dermis samples ranged from 0.2mm to 1.0 mm. The whole processing period lasted typically about 10 minutes. For the frozen tissue sectioning, the skin tissue specimen of about 20×20 mm^2, covered by OTC to preserve its biological activity (Lembares et al 1997), were frozen at a temperature of -18^0 C. We used an Ames Lab-tek cryostat microtome to section the skin tissue to obtain dermis samples with thickness in a range from 0.03 mm to 0.2 mm. Each frozen dermis sample was warmed up to the room temperature in physiological saline solution.

A micrometer with a precision of 0.003 mm was used to measure the thickness of a sample sandwiched between two optical windows of known thickness. For each sample, its thickness was measured five times successively and the averaged value was used as the sample thickness.

4.3.3 Polystyrene Microsphere Suspensions Preparation

Polystyrene microspheres of diameter of 0.966 μm were purchased as a suspension in deionized water with a nominal concentration of 10% by weight (5095B, Duke Scientific Corporation). By diluting with deionized water, we prepared three different microsphere suspensions with nominal number densities of $1.108\times10^6\ \mathrm{mm}^{-3}$, $2.056\times10^6\ \mathrm{mm}^{-3}$, and $5.054\times10^6\ \mathrm{mm}^{-3}$ based on the nominal concentration of the original suspension from the manufacturer.

Since the suspension concentration is a critical factor in determination of the absorption and scattering coefficients for suspensions from the Mie derived absorption and scattering cross sections for a single microsphere, values of the suspension concentrations have to be measured. A small portion of each prepared microsphere suspension was weighed by an electronic balance with a resolution of 0.1 mg. Then the water in the suspension was evaporated completely at 60^0C to obtain the dry microspheres to have their mass measured. The number densities of the three polystyrene suspensions were calculated from the masses of the microspheres and suspensions, the diameter of microsphere (=0.966 μm), and polystyrene mass density (= 1.05 g cm^{-3}). And these were found to be $1.569\times10^6\ \mathrm{mm}^{-3}$, $2.709\times10^6\ \mathrm{mm}^{-3}$, and $6.186\times10^6\ \mathrm{mm}^{-3}$, respectively.

4.4 Scanning Confocal Imaging System

A scanning confocal imaging system was constructed to map the surface profile of skin tissue samples used for measurements of its optical properties (Fig 4.11). The laser beam of wavelength 632.8nm was expanded and collimated through two convex lenses and a 100 μm pinhole (P1 in Fig 4.11). The collimated laser beam was focused through a 63×, 0.85 NA microscope objective (160/0.17, Melles Griot) (Objective A in Fig 4.11) and fell on the sample surface. The sample was mounted on a PZT (HPSt 1000, Piezomechanik GmbH), which was fixated on a translation stage controlled by a stepping motor. With the help of the computer-controlled PZT, the sample can move in the vertical direction in a range of 0 –17 μm in steps as small as 0.02 μm. The computer-controlled stepping motor drove the translation stage to make a line scan in the x direction with steps as small as 0.15 μm. The reflected light was separated by a 10% splitter and was collected by another 63×, 0.85 NA microscope objective (160/0.17, Melles Griot) (Objective B in Fig 4.11). A 10 μm pinhole mounted right before a photodiode was placed on the focal point of Objective B to detect the reflected light signal. The light was modulated at 17 Hz by a chopper (SR540, Stanford Research Systems Inc.). A lock-in amplifier (SR830, Stanford Research Systems Inc.) was used to measure the photodiode signals. At each point, a z-scan was conducted through the PZT. Then the translation stage moved to next position through stepping motor. A computer monitored the whole process including x and z scans and data acquisitions.

The diameter of pinhole P2 plays an important role in determining the resolutions of the confocal imaging. The diffraction-limited focus spot or "Airy disk" decides the lateral resolution of confocal microscope, which has a diameter of

$$d_{Airy} = \frac{1.22\lambda}{NA}. \tag{4.9}$$

If the pinhole diameter $D_{PH} > 1 \times d_{Airy}$, the lateral resolution is given by the Full Width at Half Maximum of Airy disk [Visscher and Struik 1994]:

$$W_{50\%} \approx \frac{0.51 \cdot \lambda}{NA}, \tag{4.10}$$

and the axial resolution (in the optical axis direction) is a function of pinhole diameter:

$$Z_{50\%} = \sqrt{\left(\frac{0.45\lambda}{n(1-\sqrt{1-NA^2/n^2}}\right)^2 + \left(\frac{\sqrt{2} \cdot n \cdot D_{PH}}{NA}\right)^2}. \tag{4.11}$$

where NA is the numerical aperture of objective. For example, when $\lambda = 0.6328\,\mu m$ and NA = 0.85, $W_{50\%} = 0.37\,\mu m$; when $\lambda = 0.488\,\mu m$ and NA = 0.85, $W_{50\%} = 0.29\,\mu m$; when $\lambda = 0.488\,\mu m$ and NA = 1.30, $W_{50\%} = 0.19\,\mu m$.

When the diameter of pinhole P2 is less than $0.25 \times d_{Airy}$, the lateral resolution becomes:

$$W_{50\%} \approx \frac{0.37 \cdot \lambda}{NA}, \tag{4.12}$$

and the axial resolution is given by [Gordon and Timothy 1989]

$$Z_{50\%} = \frac{0.45\lambda}{n(1-\sqrt{1-NA^2/n^2}}, \tag{4.13}$$

where n is the refractive index of the immerging medium for the objective. For Carl Zeiss LSM 510 Confocal Laser Scanning Microscope with a 40×/1.3 objective, the overall magnification of the imaging and detection optical system is 132, therefore, the diameter of pinhole P2 that corresponds to $1 \times d_{Airy}$ is 60.8µm. For confocal microscope we constructed, 3 µm, 10µm, 25µm, 75µm, 100µm pinholes were tested and 10 µm showed the good signal-noise ratio and good axial resolution.

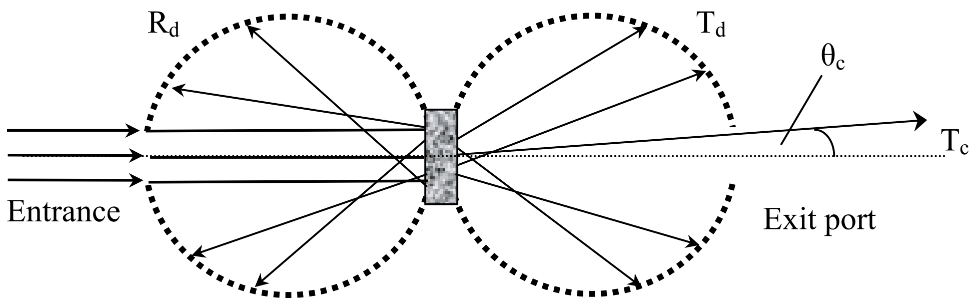

Figure 4.1 Diagram showing the definitions of the diffuse reflectance R_d, the diffuse transmittance T_d and the collimated transmission T_c.

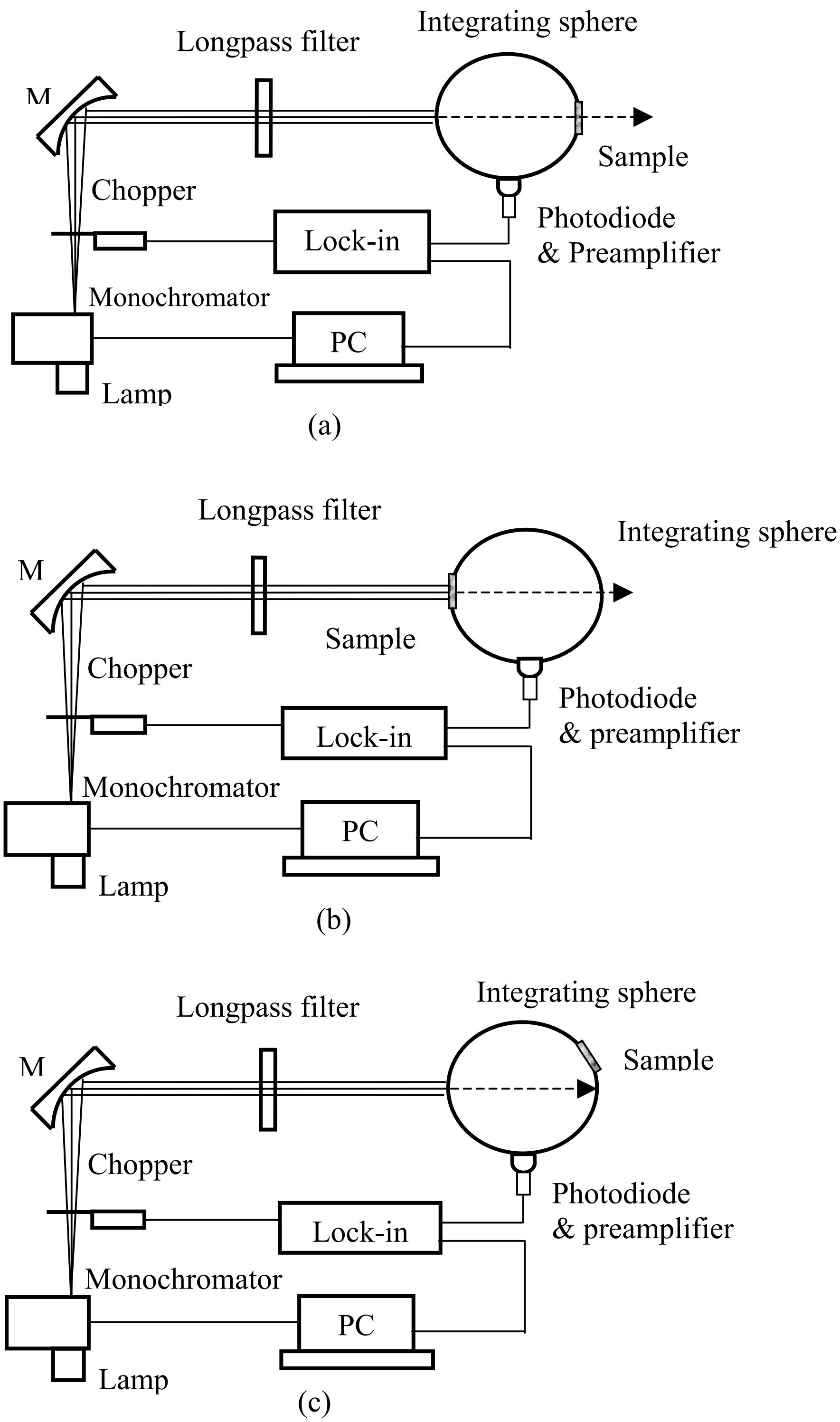

Figure 4.2 Schematics for measurement of (a) the diffuse transmittance T_d and (b) the diffuse reflectance Td and (c) the reference.

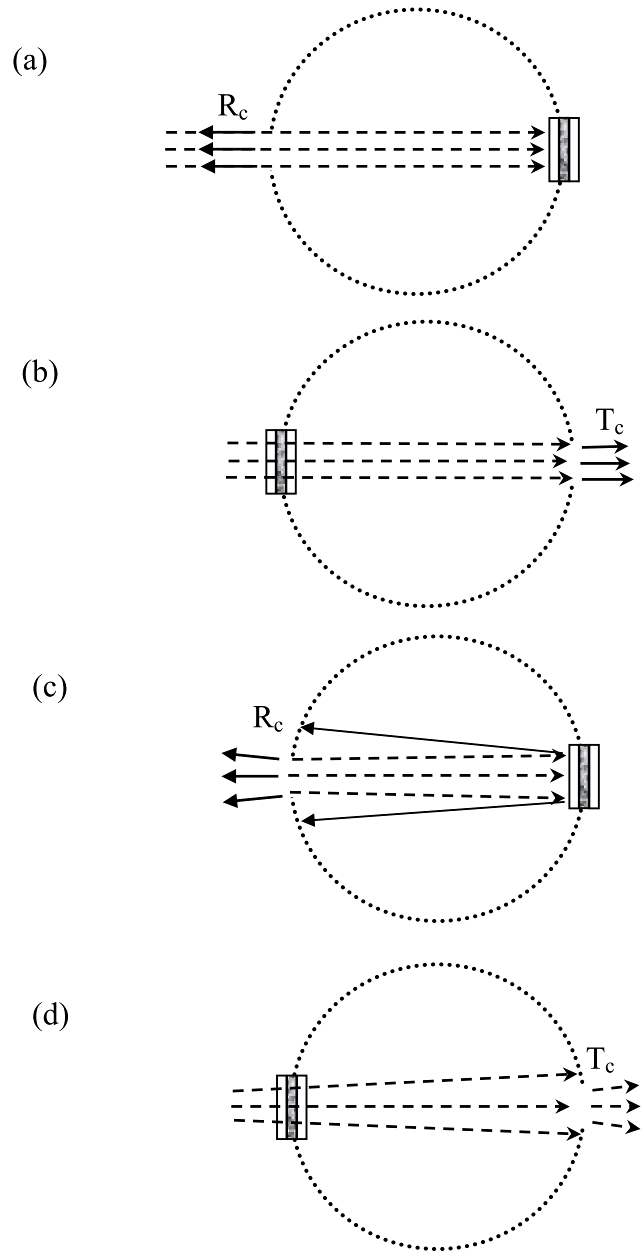

Figure 4.3 Differences between collimated incident beam and diverged incident beam. (a) and (b) are the collimated incident beam for the specular reflection R_c and the collimated transmission T_c respectively; (c) and (d) are the diverged incident beam for the specular reflection R_c and the collimated transmission T_c respectively.

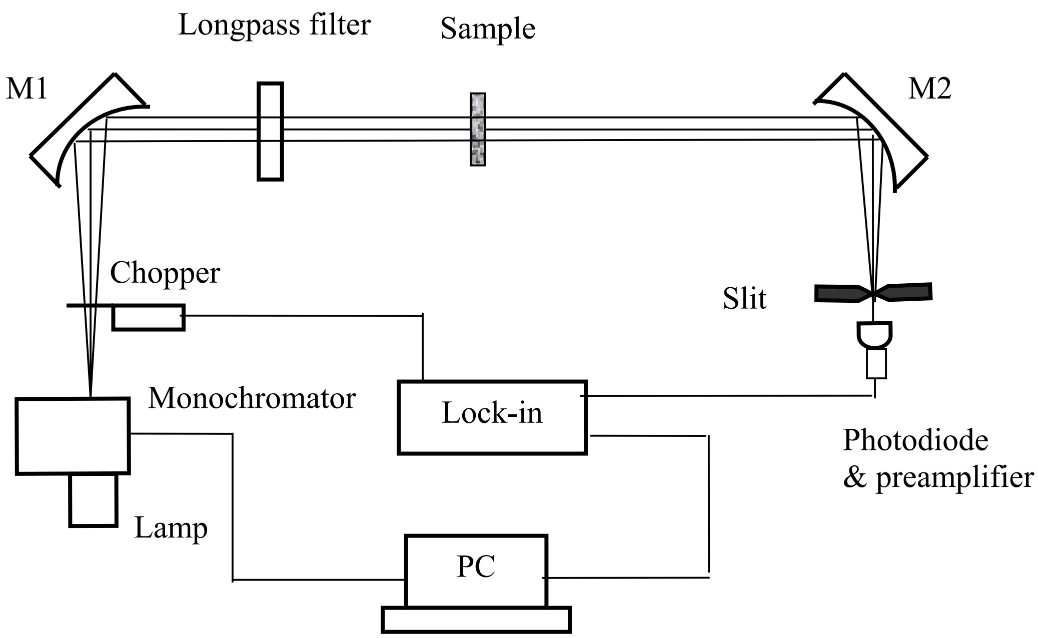

Figure 4.4 Experimental setup for measurement of the collimated transmission T_c with two concave mirrors M1 and M2.

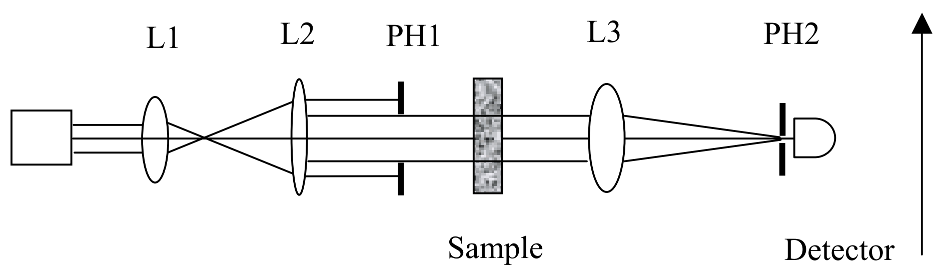

Figure 4.5 Experimental setup to investigate the speckle effect in Tc measurement. L1 and L1 are two convex lenses to expand the laser beam; PH1 is an aperture with a diameter of 2.5 mm; L3 is light colleting convex lens with a focal length of 100 mm; PH2 is a pinhole with diameter of 1 mm. Both sample and detector set (detector plus pinhole PH2) can move in the lateral direction shown as arrow in graph.

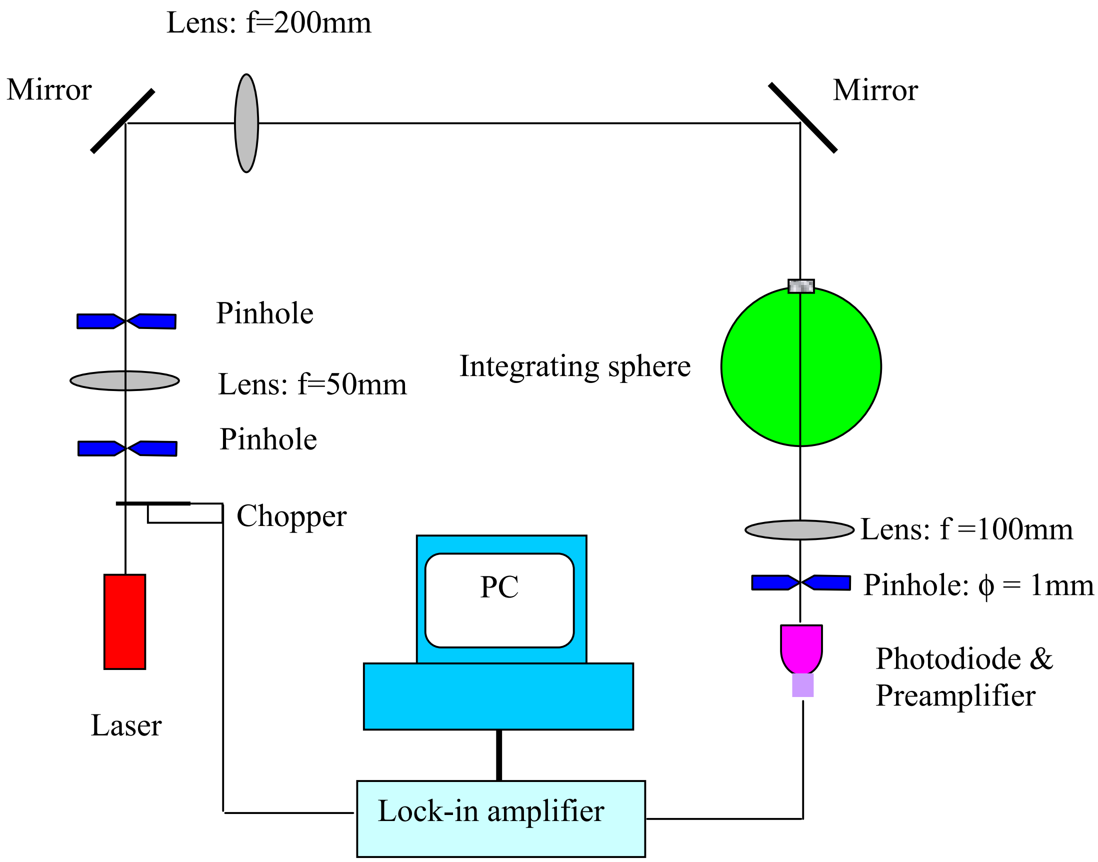

Figure 4.6 Experimental setup for measurements of R_d, T_d and T_c on a same sample.

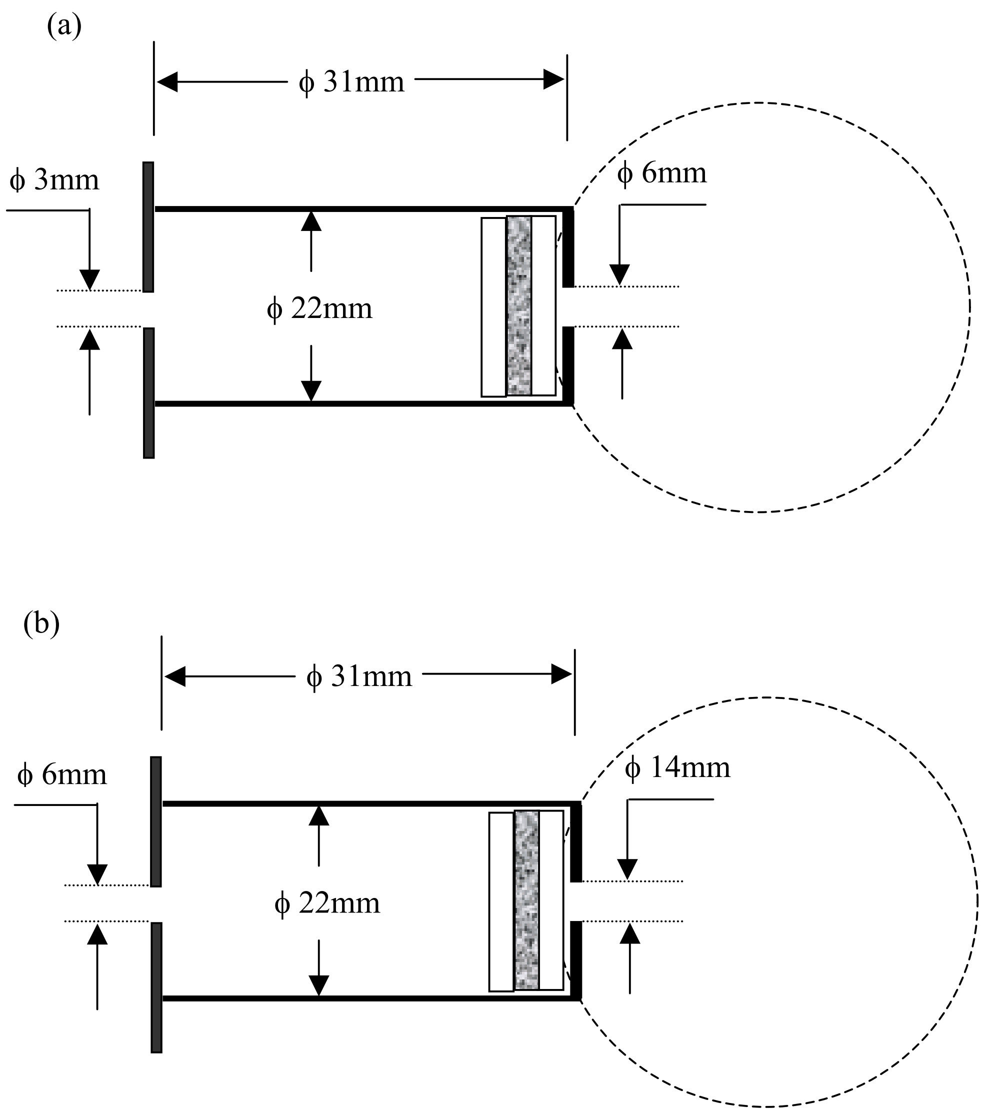

Figure 4.7 Sample holders for integrating sphere: (a) for R_d, T_d, and T_c from the same sample; (b) for R_d and T_d only.

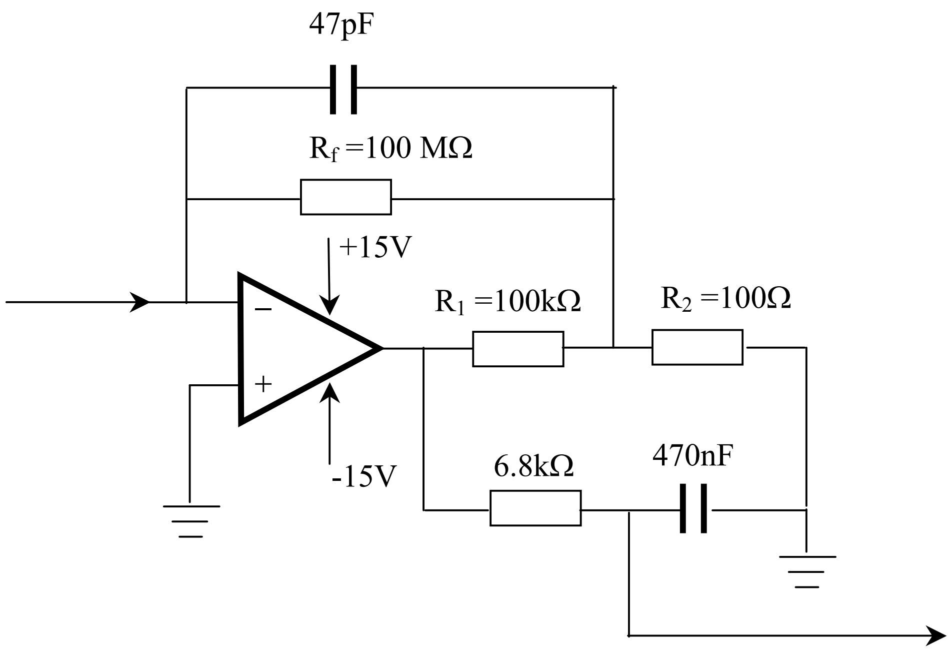

Figure 4.8 Circuit of preamplifier.

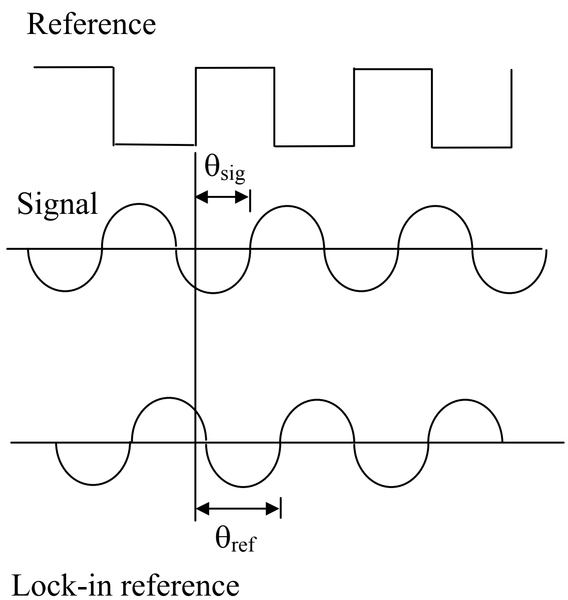

Figure 4.9 Relationship between the reference signal, signal, and the lock-in reference.

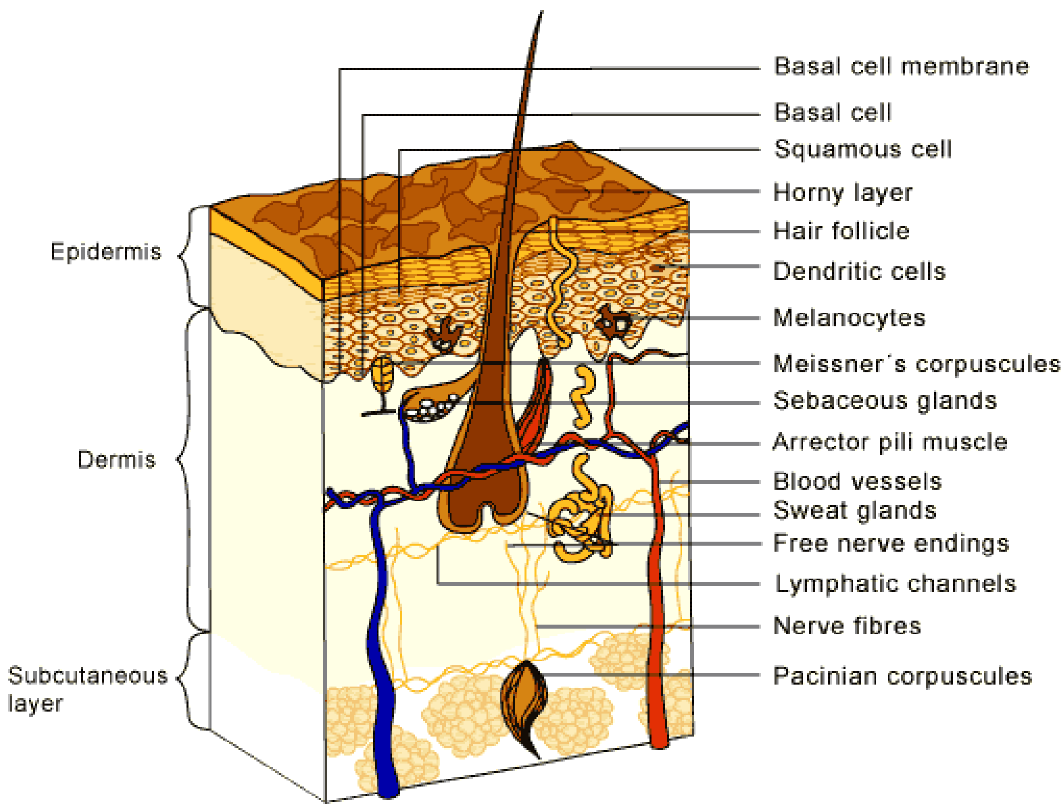

Figure 4.10 The Structure of skin tissue (adapted from http://skincancer.dermis.net).

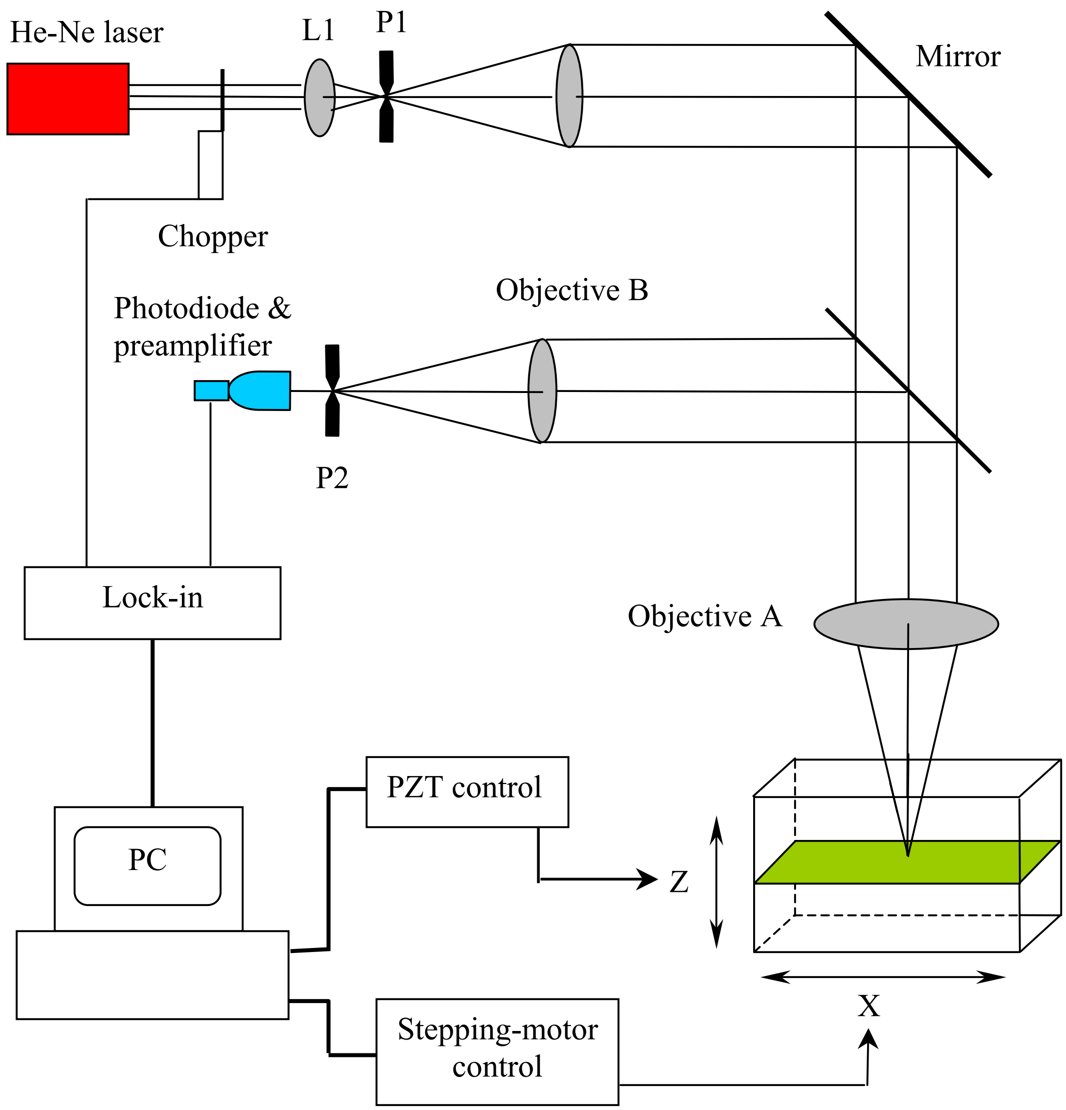

Figure 4.11 Schematics of the scanning confocal imaging system. P1 is a 100 μm pinhole, P2 is a 10 μm; Not shown above, the sample is mounted on the top surface of PZT and PZT is placed on a translation stage moved by a stepping motor.

Table 4.1 Parameters of Si and InGaAs photodiodes.

	Si photodiode	InGaAs photodiode
Active area (mm^2)	3.6 × 3.6	1.0 × 1.0
Spectral response range (nm)	190 to 1100	800 to 1800
Peak wavelength (nm)	960	--------
Photo sensitivity (A/W)	0.5	-------
Maximum dark current (nA)	0.05	100
Shunt resistance (GΩ)	0.6	-------
Rise time (μs)	0.5	5.0
Terminal capacitance (pF)	150	85

Chapter 5 Results

In this Chapter, we summarize the results of the inversely determined parameters that characterize the optical properties of polystyrene microspheres and porcine dermis tissue in vitro. The calibrations of the experimental systems and the validations of the Monte Carlo codes are first presented. The complex refractive index of polystyrene microspheres and the values of μ_s, μ_a, and g for porcine dermis tissue have been determined without considering the sample surface roughness in a spectral region between 370 nm and 1610 nm. The effects of surface roughness on the inverse determination of the bulk optical parameters were studied through numerical investigations and experimental measurements on intralipid solutions. The surface roughness of fresh porcine dermis samples were measured and the μ_s, μ_a, and g were determined by taking into account of tissue surface roughness at eight wavelengths between 325 and 1550nm.

5.1 Calibration of Optical Setups and Validation of Codes

The optical systems to measure the diffuse reflectance R_d and the diffuse transmittance T_d were calibrated with the reflection standards. The calibration of the spatial filtering systems for the collimated transmission T_c measurements was established by comparison between the measured attenuation coefficient μ_t and μ_t calculated from Mie's theory based on the known optical and geometrical parameters for a polystyrene microsphere suspension. The Monte Carlo codes that we developed to simulate light transportation within a turbid medium with flat or rough interfaces were validated by the comparison of the attenuation coefficient μ_t derived from the linear regression of the Monte Carlo produced ln (T_c) at different sample thickness based on the preset parameters, μ_s, μ_a, and g with the preset μ_t (= μ_s+μ_a).

5.1.1 Calibration of Integrating Sphere Setup

The reflective optical system with an integrating sphere employed to measure the diffuse reflectance and transmittance, R_d and T_d of a turbid sample, as well as the data process method (see section 4.1.1) has been calibrated via two diffuse reflection standards of 50% and 40% (SRS-50-010 and SRS-40-010, Labsphere Inc.) from 370 nm to 1700 nm. We also calibrated the experimental systems from 200 nm to 420 nm. Fig 5.1 plots the measured reflectances of 50% and 40% reflectance standards in comparison with the manufacturer's calibrated values between 370 nm and 1700nm. Fig 5.2 displays the measured reflectances of 50% and 40% reflectance standards in comparison with the manufacturer's calibrated values from 200 nm to 420nm. Based on these results, we estimated that the experimental errors in measured R_d and T_d were within ±5%.

Fig 5.3 shows the transmissions of two longpass filters with cut-on edges at 540 nm and 840 nm respectively.

5.1.2 Calibration of Spatial Filtering Setup

To calibrate the spatial filtering experimental setup (Fig 4.4), we measured the collimated transmission T_c of a polystyrene microsphere suspension at number density of $c_{sp} = 6.186\times10^6$ mm^{-3} for three sample thicknesses: 0.102 mm, 0.150 mm, and 0.246 mm with a collimated beam from a He-Ne laser at the wavelength of 632.8 nm. The attenuation coefficients μ_t was determined by a linear regression of ln (T_c) and was found to be 10.7 mm^{-1}, as shown in Fig 5.4.

On the other hand, from the known microsphere's diameter of 0.986 μm and the published polystyrene refractive index of 1.5867 at 632.8 nm [Nikolov 2000], Mie's theory predicts that the attenuation coefficient μ_t equals 11.1 mm^{-1} for this polystyrene microsphere suspension. By comparison, we conclude that μ_t determined by the optical system we constructed to measure the collimated transmission T_c reveals an excellent agreement with Mie's theory and has a relative error of 4%.

5.1.3 Speckle Effect

A patch of fresh-cut porcine dermis sample of 2 × 2 cm^2 was employed in the study of the speckle effect on the collimated transmission T_c measurement (see section 4.1.3). The thickness of the dermis sample used is 0.54 mm. The dermis sample was sandwiched between two window glasses. The experimental setup employed to evaluate the speckle effect is presented in Fig 4.5, which is similar to spatial filtering configuration used to measure T_c. Fig.5.5 (a) shows the variation of the collimated transmission when different parts of the dermis sample were illuminated in the lateral direction relative to the incident light by moving the dermis sample 0.5 mm each time. Fig.5.5 (b) displays the light distribution in the focal plane of the signal colleting lens by moving the pinhole and the detector in the lateral direction with a step size of 0.5 mm.

As being discussed in section 4.1.3, speckles result from the randomly constructive or destructive interferences between scatterings of the illuminating light at rough surface and in the bulk, and between scatterings and the collimated light. Taking into account of the fact that the optical properties of the dermis sample itself may fluctuate from location to location, results shown in Fig 5.5 suggest that the pinhole at the focal point of the colleting lens effectively remove majority of diffuse scatterings and the speckle effect, if still exist, does not tends to severely affect T_c measurement under the current experimental condition.

5.1.4 Validation of the Monte Carlo Codes

Numerical "experiments" were conducted in an attempt to validate the Monte Carlo codes developed to simulate the propagation of photons through a turbid medium with flat or rough surfaces. We used six different kinds of turbid media in the validation: two sets of optical parameters: (μ_s = 5.0 mm^{-1}, μ_a = 0.02 mm^{-1}, g = 0.7) and (μ_s = 10.0 mm^{-1}, μ_a = 0.02 mm^{-1}, g = 0.7) were selected to model two types of the turbid medium bulk and its surfaces were assumed either flat or rough with two different kinds of roughness characterized by two sets of parameters: (δ = 0.5 μm, *a* = 10 μm) and (δ = 1.0 μm, *a* = 10 μm). Here δ stands for rms height variation of a rough surface and *a* is its lateral correlation length. The refractive index for all the modeled turbid media was set to be 1.325. Monte Carlo simulations were conducted to calculate the collimated transmission T_c for each modeled sample in the slab configuration sandwiched between two flat window glasses with a refractive index of 1.509. The sample thicknesses for the T_c simulations were set as 0.05 mm, 0.1 mm, 0.2 mm, 0.3 mm, 0.4 mm, and 0.5 mm. The results of Monte Carlo simulated T_c are displayed in Fig 5.6. Linear regressions of the ln (T_c) were carried out to unearth the corresponding attenuation coefficient μ_t for each modeled turbid medium. For flat surfaces, T_c–derived μ_t is 5.026mm^{-1} for the modeled bulk optical parameters (μ_s = 5.0 mm^{-1}, μ_a = 0.02 mm^{-1}, g = 0.7) and 10.029mm^{-1} for the modeled bulk optical parameters (μ_s = 10.0 mm^{-1}, μ_a = 0.02 mm^{-1}, g = 0.7) (red group in Fig 5.6). For rough surfaces with (δ = 0.5 μm, *a* = 10 μm), T_c–derived μ_t is 5.013mm^{-1} for the modeled bulk optical parameters (μ_s = 5.0 mm^{-1}, μ_a = 0.02 mm^{-1}, g = 0.7) and 9.851mm^{-1} for the modeled bulk optical parameters (μ_s = 10.0 mm^{-1}, μ_a = 0.02 mm^{-1}, g = 0.7) (blue group in Fig 5.6). For rough surfaces with (δ = 1.0 μm, *a* = 10 μm), T_c–derived μ_t is 4.996mm^{-1} for the modeled bulk optical parameters (μ_s = 5.0 mm^{-1}, μ_a = 0.02 mm^{-1}, g = 0.7) and 9.844mm^{-1} for the modeled bulk optical parameters (μ_s = 10.0 mm^{-1}, μ_a = 0.02 mm^{-1}, g = 0.7) (pink group in Fig 5.6). By comparison, we found that the Monte Carlo codes successfully recovered the preset μ_t (= μ_s + μ_a) under either flat or rough surface conditions and thus validated.

5.2 The Complex Refractive Index of Polystyrene Microsphere.

The complex refractive index, $n = n_r + i n_i$, of polystyrene microspheres were determined from the measurements of the diffuse reflectance R_d and diffuse transmittance T_d of the polystyrene microsphere suspensions. The derivation of n_r and n_i was based on the Monte Carlo simulation which was similar to the previous one used to determine the optical parameters (μ_s, μ_a, g) from tissue sample [Peters et al 1990, Du et al 2001]. The main modifications introduced were the choice of Mie's phase function, instead of Henyey-Greenstein function as the scattering phase function, and a new procedure to sample the scattering angles according to Mie's phase function (see section 3.2).

5.2.1 Experimental Method

Three different polystyrene microsphere suspensions were under our investigations, which have number densities of $1.569\times10^6\ \mathrm{mm}^{-3}$, $2.709\times10^6\ \mathrm{mm}^{-3}$, and $6.186\times10^6\ \mathrm{mm}^{-3}$ respectively (see section 4.3.3). All the suspension samples were examined under an optical microscope to make sure that the microspheres were not clustered together. Every sample was rigorously shaken before the start of measurements to ensure the homogeneity of the suspension. A suspension sample of polystyrene microspheres was contained within a spacer that covered by two sapphire windows of 0.5 mm thick. The diffuse reflectance R_d and diffuse transmittance T_d for each polystyrene microsphere suspension were measured at wavelengths λ between 370 nm and 530 nm with a step size of 10 nm and between 530 nm and 1610 nm with a step size of 30 nm by a system described in section 4.1.1. The sample thickness for the Rd and Td measurements has the same value of D = 0.246 mm for three polystyrene microsphere suspensions.

For the purpose of validation of the integrating measurements and the Monte Carlo based inverse calculations, the collimated transmission T_c was measured for a suspension sample of $c_{sp} = 6.186\times10^6\ mm^{-3}$ with a system described in section 4.1.2. Three different sample thickness values of D = 0.112 mm, 0.246mm, 0.463 mm were used to obtain the dependence of $\ln(T_c)$ on D at the same sequence of wavelength steps. The attenuation coefficient μ_t was derived from the slope at each wavelength

$$\mu_t = -\frac{\Delta(\ln T_c)}{\Delta D} \tag{5.1}$$

All the measurements of R_d, T_d, and T_c were conducted at room temperature of about 24 ^{0}C. The experimental errors were estimated to be ±5% for R_d and T_d and ±3% for T_c.

5.2.2 Modelling Method

The optimal values of n_r and n_i were approached through the Monte Carlo simulations and optimization iterations with a least-square criterion. For a set of trial values of n_r and n_i, the scattering cross section σ_s, the absorption cross section σ_a, and the scattering phase function $p(\theta)$ of a sphere were firstly calculated from the Mie theory (see section 2.2) with the known diameter of sphere (= 0.966 μm) and the published complex refractive index of water $n_w = n_{rw} + i\,n_{iw}$ [Hale and Querry 1973]. Here $p(\theta)$ is also called Mie's phase function where θ is the scattering angle. Then we assume that the optical responses of a suspension, the scattering coefficient μs and the absorption coefficient μa, are related to the scattering and absorption cross sections, σ_s and σ_a of a single sphere through

$$\mu_s = c_{sp} \cdot \sigma_s \tag{5.2}$$

$$\mu_a = c_{sp} \cdot \sigma_a + \mu_{aw} \tag{5.3}$$

where c_{sp} is the number density of the microsphere suspension and $\mu_{aw} = 4\pi n_{iw}/\lambda$ is the absorption coefficient of the water at wavelength λ. The above assumption is based on the dominance of single scattering regime in light transportation through the suspension samples of small microsphere concentration. Subsequently, with a Monte Carlo code that has been validated extensively [Song et al 1999, Du et al 2001], the diffuse reflectance and transmittance, $(R_d)_{cal}$ and $(T_d)_{cal}$, were obtained through accurately tracking the incident photons according to the suspension's optical parameters (μ_s, μ_a, and $p(\theta)$), the sample's geometry, the sapphire windows, and the integrating sphere. The iteration process for inverse determination of n_r and n_i stopped when an error function Σ defined as

$$\Sigma = \left(\frac{(R_d)_{cal} - R_d}{R_d} \right)^2 + \left(\frac{(T_d)_{cal} - T_d}{T_d} \right)^2 \tag{5.4}$$

satisfied the condition: $\Sigma \le \Sigma_c$. We employed a value of 4×10^{-4} for Σ_c, which corresponds to a relative error of about 1.4% for $(R_d)_{cal}$ and $(T_d)_{cal}$.

In the region of $370\,\text{nm} \le \lambda \le 950\,\text{nm}$, water was treated as a transparent immersion medium, i.e. without absorption. The Mie calculations for the Monte Carlo simulations were carried out using a version of Mie code for transparent immersion medium [Bohren and Huffman 1983]. Since water shows an absorption peak near λ = 1450 nm, a version of the Mie code for absorbing immersion medium had been developed [Yang et al 2002] and was used in our study to generate μ_s, μ_a and $p(\theta)$ in the region of $920\text{nm} \le \lambda \le 1610\text{nm}$ (see section 2.2.2).

A technique that samples the scattering angles according to the Mie's phase function was adopted in the Monte Carlo simulation, which was first proposed by Toublanc (1996) (see section 3.2). This technique can help reduce computing time tremendously.

All simulations were carried out on our parallel computing cluster consisting of 32 PCs with Celeron CPU of 500MHz. Each Monte Carlo simulation tracked 3×10^5 photons with statistical fluctuations negligible to the experimental errors of R_d and T_d and took about five minutes to complete on one PC.

5.2.3 Results

Fig 5.7 shows the measured diffuse reflectance Rd and transmittance Td from two polystyrene microsphere suspensions with the same sample thickness d = 2.46mm from 370 nm to 1700nm. The number densities of the two suspensions in Fig 5.7 are 1.569×10^6 mm^{-3} and 2.709×10^6 mm^{-3} respectively.

The real and imaginary refractive indices of the polystyrene microspheres are presented in Fig.5.8 as functions of the wavelength. The mean values were obtained by averaging over data determined from the three samples of different concentrations with the error bars indicating the standard deviations. For comparison, we included previously reported values of n_r for polystyrene [Matheson and Saunderson 1952, Nikolov and Ivanov 2000] in Fig.5.8 (a).

The wavelength dependence of n_r has been fitted to the Cauchy dispersion relation [Matheson and Saunderson 1952, Nikolov and Ivanov 2000]

$$n(\lambda) = A + \frac{B}{\lambda^2} + \frac{C}{\lambda^4} \tag{5.5}$$

for the transparent region of λ ranging from 390 to 1310nm, as shown by the solid line in Fig.5.8 (a). With λ in the unit of micrometer, we found A = 1.5725, B = 0.0031080, C = 0.00034779 based on a least-square fitting.

The uniqueness of the determined complex refractive index is critical in validating the use of the error function Σ as the metric for guiding iteration. We have studied the dependence of Σ on n_r and n_i at two wavelengths of 950 and 1430nm with stepsizes of 1×10^{-4} in n_r and 1×10^{-4} in n_i for λ = 950 nm and 1×10^{-3} for λ = 1430 nm, as shown in Fig.5.9 for one sample. These results established that a unique absolute minimum of Σ exists in the ranges of n_r and n_i investigated at both wavelengths of weak and strong absorption. The well-behaved error function Σ demonstrated that the employed inverse algorithm leads to a unique solution of complex refractive index of polystyrene microspheres from the measured data of R_d and T_d. The errors in n_r using the criteria of $\Sigma < 4\times10^{-4}$ were estimated to be about 0.002 or less.

To examine the consistency of the inverse calculations, we compared the attenuation coefficients $\mu_t = \mu_a + \mu_s$ determined from the measurements of T_c, based on Eq.(5.1), and from the refractive indices of microsphere and water, based on Eq.(5.2) and Eq.(5.3), for one sample with the microsphere concentration of $c_{sp} = 6.186\times10^6$ mm^{-3}. The results are shown in Fig.5.10 that demonstrate the excellent agreement between the two methods of determining μ_t. The signal-to-noise ratio of the Tc data became less than 10 for wavelength between 370 and 450nm because of the reduced light intensity and sensitivity of the Si photodiode and thus no μ_t data were derived from T.

The comparison between the calculated and measured values of R_d and T_d is shown in Fig 5.11 for a polystyrene microsphere suspension with a concentration of 1.569×10^6 mm^{-3} as an example. The agreement established between the calculated and the measured R_d and T_d provides an additional validation of the inverse calculations.

5.3 Optical Parameters of Porcine Dermis under the Smooth Surface Assumption

The optical properties of porcine dermis tissue were investigated in a spectral region between 370 nm and 1700 nm. Optical parameters, μ_s, μ_a, and g were inversely determined through Monte Carlo simulations under an assumption that the surfaces of the dermis tissue samples were flat and smooth.

5.3.1 R_d and T_d Measurements

The diffuse reflectance R_d and the diffuse transmittance T_d were measured with an integrating sphere (see section 4.1.1) at wavelengths λ between 370 nm and 530 nm with a step size of 10 nm and between 530 nm and 1610 nm with a step size of 30nm. The thickness of fresh-sectioned dermis samples ranged from 0.5 mm to 1.17 mm. All the Rd and Td measurements were completed within 30 hours after the animal death. A dermis sample was sandwiched between two flat window glasses with one drop of physiological saline solution placed between the glass and tissue to help to remove air bubbles.

Diffuse reflectance R_d and transmittance T_d as a function of wavelength between 370 nm and 950 nm from two porcine dermis samples with sample thickness of 0.56 mm and 1.15mm respectively are shown in Fig 5.12. Fig 5.13 presents the diffuse reflectance R_d and transmittance T_d as a function of wavelength from 890 nm to 1700 nm from two porcine dermis samples with sample thickness of 0.65 mm and 1.07 mm respectively.

5.3.2 Tc Measurements

The measurements of the collimated transmission T_c for porcine dermis samples with different thickness were conducted through the spatial filtering setup (see section 4.1.2). Each dermis sample was sandwiched between two window glasses with one or two drops of physiological saline solution to help get rid of air bubbles and was illuminated by a beam of 6.35 mm in diameter. A step size of 10 nm for wavelength λ between 370 nm and 530 nm and a step size of 30 nm for wavelength λ from 530 nm to 1610 nm were used. The sample thickness varies from 0.05 mm up to 0.4 mm.

The attenuation coefficient μ_t is usually derived from the thickness dependence of the collimated transmission T_c by means of the linear regression to ln (T_c) [Peters et al 1990, Du et al 2001]. However, it is only in the so-called single scattering regime that the plot of ln (T_c) versus the sample thickness *d* is a straight line and μ_t can be determined accurately from the slope. The existence of multiple scatterings in the sample tends to mix part of scatterings with the collimated light and that cannot be separated from each other experimentally. The dependence of ln (T_c) on the thickness *d* gradually becomes nonlinear as *d* increases. When multiple scatterings exist, linear regression to ln (T_c) always underestimates the value of μ_t.

As pointed out by Wilson (1995), it is only when the sample thickness $d \ll 1/\mu_s$ that the effect of multiple scatterings in the sample is negligible. In order to reach this requirement, for skin tissues of which the scattering coefficients are about 20mm^{-1}, the thickness of samples is in the range of 50 μm. Practically we found that skin tissues have to be frozen to get such thin a sample and the integrity of a skin tissue sample with thickness under 0.1 mm is remarkably reduced in comparison with thick samples.

In order to utilize thick samples, a diffusion model to calculate the collimated transmission of a slab was discussed in section 2.3.1 of Chapter 2. Instead of linear regression, the thickness dependence of T_c was fitted to a nonlinear equation, Eq. (2.83) to retrieve μ_t. An example is displayed in Fig 5.14 for experimental data at 1010nm.

For each sample, its thickness *d* was measured 5 times successively with a micrometer of 0.003 mm in precision. And we found the average relative error of the thickness measurements were ± 15% for sample thickness $d < 0.1$ mm, ± 8% for 0.1 mm $< d < 0.2$ mm, ± 5% for 0.2 mm $< d < 0.5$ mm, ± 1% for $d > 0.5$ mm.

5.3.3 Results of Dermis Tissue Optical Parameters

Monte Carlo simulations were performed for each sample with the measured R_d and T_d to inversely determine the value of μ_s, μ_a, and g as a function of wavelength. The refractive index of dermis tissue was assumed to be 1.41 for all the wavelengths. Using Tc-determined μ_t as a limitation to μ_s and μ_a ($\mu_t = \mu_s + \mu_a$), optimal values of μ_s, μ_a, and g were approached through the inverse Monte Carlo simulations (see section 3.3).

Combining the results from 10 porcine dermis samples, we obtained the average values of the optical parameters as a function of wavelength from 370 nm to 1700nm, as shown in Fig 5.15. The error bars represent the standard deviations of the corresponding parameters among the samples.

The typical result of the calculated R_d and T_d in comparison with the measured R_d and T_d for a sample is illustrated in Fig 5.16 as a function of wavelength from 370 nm to 950 nm. An agreement between the calculated and the measured data of R_d and T_d has been approved.

§5.3.4 Convergence Test of the Inverse Calculations

The uniqueness of the inversely determined optical parameters, μ_s, μ_a, and g from the measured Rd and Td was examined. The behavior of error function Σ was investigated at two wavelengths of 500 nm and 1460nm with step sizes of 1×10^{-3} in g and 2×10^{-4} in μ_s for 500nm, as well as 1×10^{-3} in g and 2×10^{-3} in μ_s for 1460 nm, as displayed in Fig 5.17. These results clearly indicate that absolute minimum of Σ exists uniquely in the regions of μ_s and g investigated at both wavelengths of weak and strong absorption. The convergence of the error function demonstrates that the employed inverse algorithm leads to a unique solution of μ_s, μ_a, and g from the measured R_d and T_d.

5.4 Effect of Surface Roughness on Bulk Optical Parameters

The optical parameters μ_s, μ_a, and g for a turbid medium cannot be measured directly. The determination of these parameters from the measurements like the diffuse reflectance R_d, the diffuse transmittance T_d, and the collimated transmission T_c relies on how accurately the light distributions can be modeled. The *in vitro* measurements of Rd, Td, and Tc in section 5.3, as well as previous reports [Peters et al 1990, Beck et al 1997, Simpson 1998, Du et al 2001] involved the use of thin slab tissue with thickness varying from 50μm to 2mm and the surfaces of the slab tissue were assumed flat and smooth in the inverse determination of μ_s, μ_a, and g. However, all the tissue sample surfaces possess a certain degree of roughness, which is on the scale of light wavelength. It has been proved that even a moderate index mismatch at the rough tissue interfaces can significantly affect light distribution in skin phantoms [Lu et al 2000]. In order to evaluate the effect of surface roughness on the inverse determination of the optical parameters of tissue sample, which has not been studied yet before, a theoretical analysis is carried out in this section (section 5.4) through numerical "experiments" based on a new version of Monte Carlo code that takes surface roughness into account. Optical parameters μ_s, μ_a, and g for porcine dermis tissue, which were determined from the measured R_d, T_d, and T_c with surface parameter δ and *a* measured in section 5.5 will be presented in section 5.6.

5.4.1 Modelling Method

We adapted an extensively tested MC code for modeling light distribution in rough tissue samples to calculate R_d, T_d and T_c [Song et al 1999, Lu et al 2000, Du et al 2001]. The assembly of a rough tissue slab between glass plates was modeled by a 3-layer structure of cylindrical slabs. We employed the Henyey-Greenstein phase function to describe scattered light distribution [Flock et al 1992]. The photons emerging from the assembly were registered separately to obtain R_d, T_d and T_c according to their positions on the outside surfaces of the holder plates and exit directions, as depicted in Fig. 4.1. Note here that the T_c was defined in our simulations as the portion of the incident photons leaving the integrating sphere through the exit port within a cone angle θ_c (= 5.00×10^{-3} rad) from the direction of incident light [Peters et al 1990, Du et al 2001]. The simulation began with a photon incident normally on the smooth air-plate interface and then followed its trajectory through the rough interface of plate-tissue. Most of the tracked photons transported into the tissue sample and some, if not absorbed, exited from the sample and holder plates through the side surfaces or the air-plate interfaces. The profile function of each rough interface between the plate and sample was generated numerically through a stationary Gaussian stochastic process characterized by a rms height δ and a transverse correlation length a [Lu et al 2000]. For each configuration of the sample assembly, R_d, T_d and T_c were calculated using the bulk parameters of μ_a, μ_s, g and surface parameters δ and a with predetermined refractive indices of n_h and n for the sample holder and sample, respectively. To study the effect of surface roughness on inverse determination of optical parameters, we define a squared error function

$$\Sigma = \left(\frac{R_d - R_{d0}}{R_{d0}}\right)^2 + \left(\frac{T_d - T_{d0}}{T_{d0}}\right)^2 + \left(\frac{T_c - T_{c0}}{T_{c0}}\right)^2 \tag{5.6}$$

where R_{d0}, T_{d0} and T_{c0} are either the calculated signals for a reference configuration or the measured ones, and R_d, T_d and T_c are those for the investigated configuration. Σ is used as a metric for the iterative process to converge on an optimized set of parameters which stops when $\Sigma \leq \Sigma_c$. The value of Σ_c is chosen to be 4×10^{-4} corresponding to relative errors of about 1% in measuring T_d, T_c or R_d. The inversely determined parameter set can be either that of the bulk (μ_s, μ_a, g) or of the surface (δ, a) with the other set treated as known.

5.4.2 Results

We started by investigating first the effect of surface parameters on the inverse determination of bulk parameters with n = 1.41 and $n_h = 1.52$ for samples of skin dermis and glass holder, respectively, near the light wavelength $\lambda = 1\mu m$. It was confirmed that the inverse solution of (μ_s, μ_a, g) can be uniquely determined by minimizing Σ for each of different sets of surface parameters so that the updated values of (R_d, T_d, T_c) approach to the reference values. As an example, we considered a case using $\mu_{s0} = 5.00mm^{-1}$, $\mu_{a0} = 0.20mm^{-1}$, g_0=0.900, $\delta_0 = 10.0\mu m$ and a_0=100μm for the reference configuration. When the transverse correlation length is changed from the reference value a_0 to $a = 200\mu m$ with $\delta=\delta_0$, the bulk parameters can be uniquely determined to be $\mu_s = 11.3mm^{-1}$, $\mu_a = 0.40mm^{-1}$ and g = 0.95 by minimizing Σ in the ranges of $10.0 < \mu_s < 12.0mm^{-1}$, $0.30 < \mu_a < 0.50mm^{-1}$ and $0.90 < g < 1.00$. Furthermore, we found that the relative role of δ and a on the values of bulk parameters can be combined approximately into a single slope factor of δ/a. The effect of surface roughness in term of δ/a on the inverse determination of bulk parameters is shown in Fig.5.18. We note that the two groups of data presented in Fig. 5.18 were obtained with the reference configurations set at $\delta/a = 0.10$ (a_0=100μm,

δ_0=10μm), corresponding to different optical thickness {= (μ_{a0} + μ_{s0})d} of 1.02 and 3.04 for a sample of 0.2mm thickness. The responses of μ_s'= (1-g)μ_s to the roughness are shown in the inserts of Figs.5.13 (c) and (f).

To verify our numerical results, we measured T_d, T_c and R_d of intralipid samples between two BK7 windows of 3mm thickness (WNL0103, Casix). One pair of windows was made rough on one side with Al_2O_3 particles of nominal sizes of 9.5μm (Optical polishing powder, Universal Photonics). 20% intralipid solution (Baxter Healthcare) was diluted with deionized water by a ratio of 1:7 to obtain samples of $\mu_s \approx 15mm^{-1}$ [Flock et al 1992]. The refractive index of the intralipid sample n_s was determined to be 1.34 at λ= 633nm using a refractometer built for turbid samples. Optical measurements of the identical intralipid samples in two pairs of windows, smooth and rough, were carried out with a laser beam with λ= 633nm, modulated at 17Hz and detected using a Si-photodiode and a lock-in amplifier. The T_d and R_d were measured with an integrating sphere and T_c was measured with a spatial filtering setup within the cone angle θ_c as shown Fig. 4.1 [Du et al 2001]. For the sample between the smooth windows, we obtained T_d = 32.5%, R_d = 8.44%, and T_c = 4.16% for a sample thickness of 0.20mm and these were used as the reference values in Eq. (5.6) to determine the bulk parameters of the intralipid samples by assuming δ = 0. This produced $\mu_s = 14.0mm^{-1}$, $\mu_a = 0.94mm^{-1}$ and g = 0.76. For the sample between rough windows, the measured values changed to T_d =32.4%, R_d =9.23% and T_c =0.038% for the same thickness and they were used as the reference values to determine possible values of surface parameters by calculating Σ as a function of δ and a. Identical bulk parameters of μ_s, μ_a and g were used as the input parameters since the intralipid samples were identical. The results are plotted in Fig. 5.19 which clearly demonstrates that δ and a cannot be uniquely determined in this process except the ratio δ/a ($\approx$ 0.11). We also determined the bulk parameters from measured T_d, T_c and R_d and found that they became μ_s=38.8mm^{-1}, μ_a=1.3mm^{-1} and g=0.89 if the roughness was neglected by assuming δ=0. These results agree with the data in Fig. 5.18.

The digital microscope images shown in Fig 5.20 are the rough surfaces of the glass grounded with 9.5 μm Al_2O_3 polishing power [Fig 5.20(a)], as well as glasses grounded with 5μm [Fig 5.20 (b)] and 3 μm [Fig 5.20(c)] Al_2O_3 polishing power.

5.5 Surface Roughness Parameters of Porcine Dermis Samples

Porcine dermis samples used for surface roughness measurements with a laser scanning confocal microscope were fresh sectioned from skin tissue in the same as ones used for optical measurements (see section 4.3.2). Each dermis sample was sandwiched between two No.1 cover slides with glass thickness about 0.17mm. One or two drops of physiological saline solution were placed between the cover slide and dermis to help to get rid of air bubbles. The typical sample size is about 2 cm × 2 cm × 0.3 mm. For each dermis sample, two different surface locations were probed using a procedure described in section 3.4.3.1.

Fig 5.21 shows the confocal images of the rough surface of a dermis tissue sample taken sequentially at different vertical levels. Fig 5.22 displays a one-dimensional line profile that is chosen randomly within a rough surface. Five such one-dimensional line surface profiles were randomly chosen from each dermis sample to conduct the statistical analysis. Fig 5.23 gives an example of the height distribution function of a rough dermis sample surface and its equivalent Gaussian function which defines as a Gaussian function that has the same under-the–curve area as the height distribution function. The autocovariance function that is used to determine the lateral correlation length *a* is graphed in Fig 5.24 for a one-dimensional line surface profile with the results of a = 10.39 μm and δ = 8.10 μm.

Table 5.1 lists the statistic data of surface roughness for three porcine dermis samples. The mean values and its standard deviations were calculated from four locations within each sample. Table 5.2 summarizes the statistical parameters of surface roughness averaged among three porcine dermis samples.

The surface profile measuring procedure was validated by an optical flat window glass, as well as three BK7 optical glasses (WNL0103, Casix) grounded with Al_2O_3 particles of nominal size of 9.5 μm, 5 μm, and 3 μm (Optical polishing powder, Universal Photonics), as well as a rough surface sample (Mexico-6024) of which the surface roughness were examined by Atomic Force microscopy (AFM). Fig 5.25 exhibits the reconstructed surface profile for an optical flat surface. Table 5.3 presents the statistical results for the grounded glass surfaces measured by confocal microscope. Comparison between the confocal microscope and AFM is displayed in Table 5.4.

5.6 Optical Parameters of Porcine Dermis under the Rough Surface Assumption

Laser has an advantage over an incoherent light source to provide large irradiance. The high irradiance of incident light enables the measurements of the diffuse reflectance R_d, the diffuse transmittance T_d and the collimated transmission T_c from the same turbid sample of thickness up to 1.5 mm by means of an integrating sphere. For a dermis sample, the simultaneously measured Tc are more accurate than the T_c obtained from thin samples which leads to large error in thickness measurements and additional damage to the tissue integrity due to the freezing process for sectioning. This approach ensures the employment of the inverse determination we developed in section 5.4 to take into account of the surface roughness of the dermis samples. Therefore, we can improve significantly the accuracy of the optical parameters inversely determined from the simultaneously measured R_d, T_d, and T_c.

5.6.1 Experimental Method

A modified integrating sphere system was employed to measure the diffuse reflectance R_d, the diffuse transmittance T_d, and the collimated transmission T_c directly from the same turbid sample, as shown in Fig 4.6. Seven lasers provide the incident light separately at eight wavelengths: 325 nm and 433 nm from a Cd-He laser (Series 56, Omnichrome), 532 nm from a SHG YAG laser, 632.8 nm from a He-Ne laser (05-LHP-143, Melles Groit), 1640 nm from a YAG laser, 855 nm, 1310 nm, and 1550 nm from three diode laser. The diameter of the entrance and exit ports of the integrating sphere was 3.0 mm. The diameter of sample exposure area was 6.0 mm. The incident laser beam was modulated at 17 Hz by a chopper. Dermis samples were fresh sectioned from the porcine skin tissue. The sample thickness is within the range between 0.2 mm and 0.5 mm for wavelengths 325 nm, 532nm, and 632.8 nm and between 0.4 mm and 1.0 mm for wavelengths 850nm, 1064nm, 1310nm, and 1550nm. At each wavelength, five dermis samples with different thickness were used for R_d, T_d, and T_c measurements.

5.6.2 Results

Under the assumption that surfaces of the samples were flat, optical parameters, μ_s, μ_a, and g were firstly determined from each set of R_d, T_d, and T_c through the inverse Monte Carlo simulations. Then using the surface roughness parameters: $\delta = 8.17$ μm and a = 8.96 μm which were determined with the confocal imaging method, optical parameters, μ_s, μ_a, and g were inversely calculated under the assumption that surfaces of the sample were rough. The least-square criterion Σ for the optimization of μ_s, μ_a, and g was defined as

$$\Sigma = \left(\frac{(R_d)_{cal} - R_d}{R_d} \right)^2 + \left(\frac{(T_d)_{cal} - T_d}{T_d} \right)^2 + \left(\frac{(T_c)_{cal} - T_c}{T_c} \right)^2 \tag{5.7}$$

where $(R_d)_{cal}$, $(T_d)_{cal}$, and $(T_c)_{cal}$ are the Monte Carlo simulated diffuse reflectance, diffuse transmittance, and the collimated transmission for a trial set of μ_s, μ_a, and g.

Fig 5.26 presents the average values of μ_s, μ_a, and g for porcine dermis tissue under the condition that surfaces are smooth (circles in Fig 5.26) or rough with δ = 8.17 μm and a = 8.96 μm (squares in Fig 5.26).

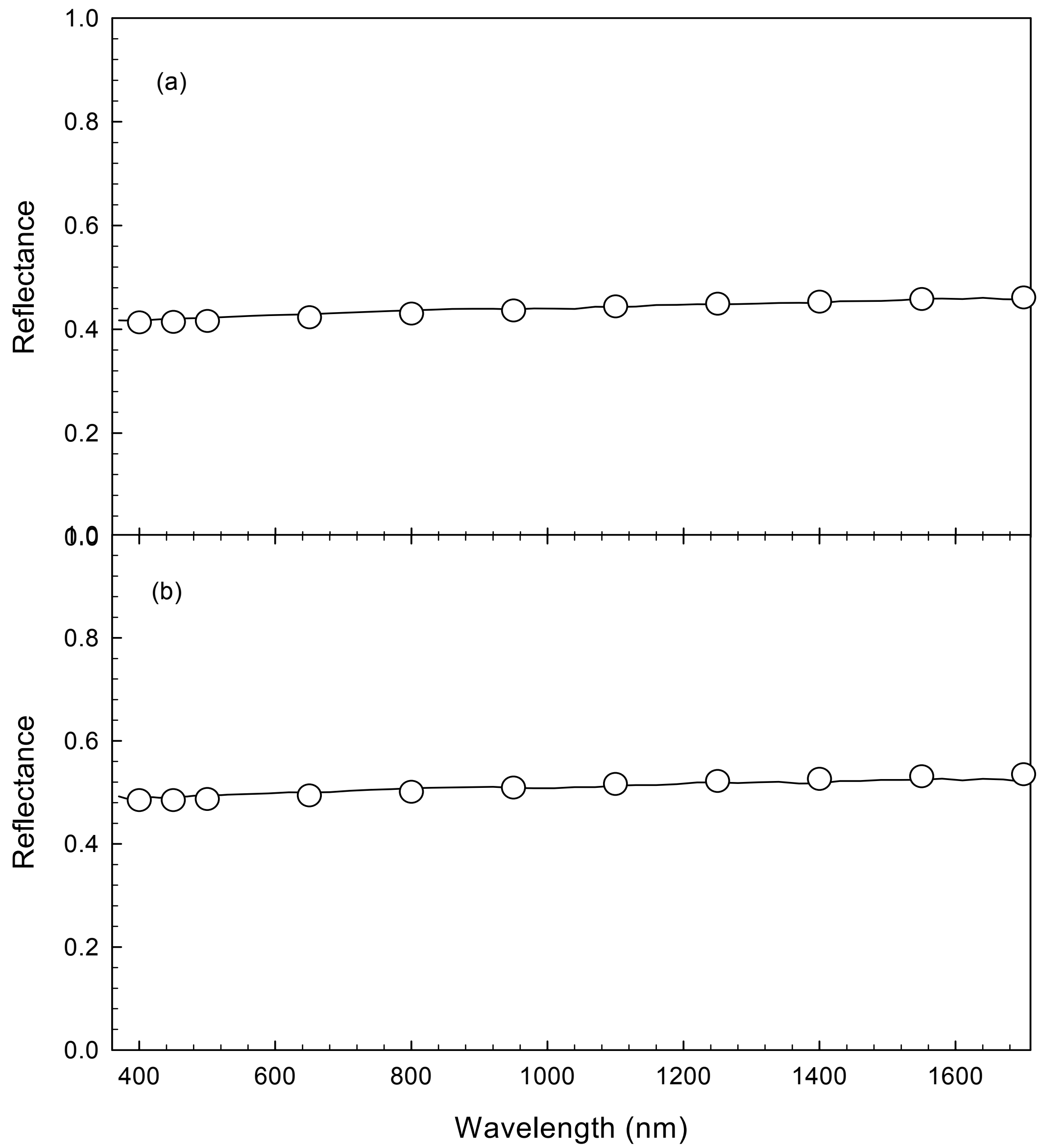

Figure 5.1 Calibration of integrating sphere setup with two reflectance standards: (a) 40% and (b) 50%. The solid lines are the measured reflectance values of two reflectance standards respectively by the integrating sphere. The circles are the manufactory's calibrated reflectance values.

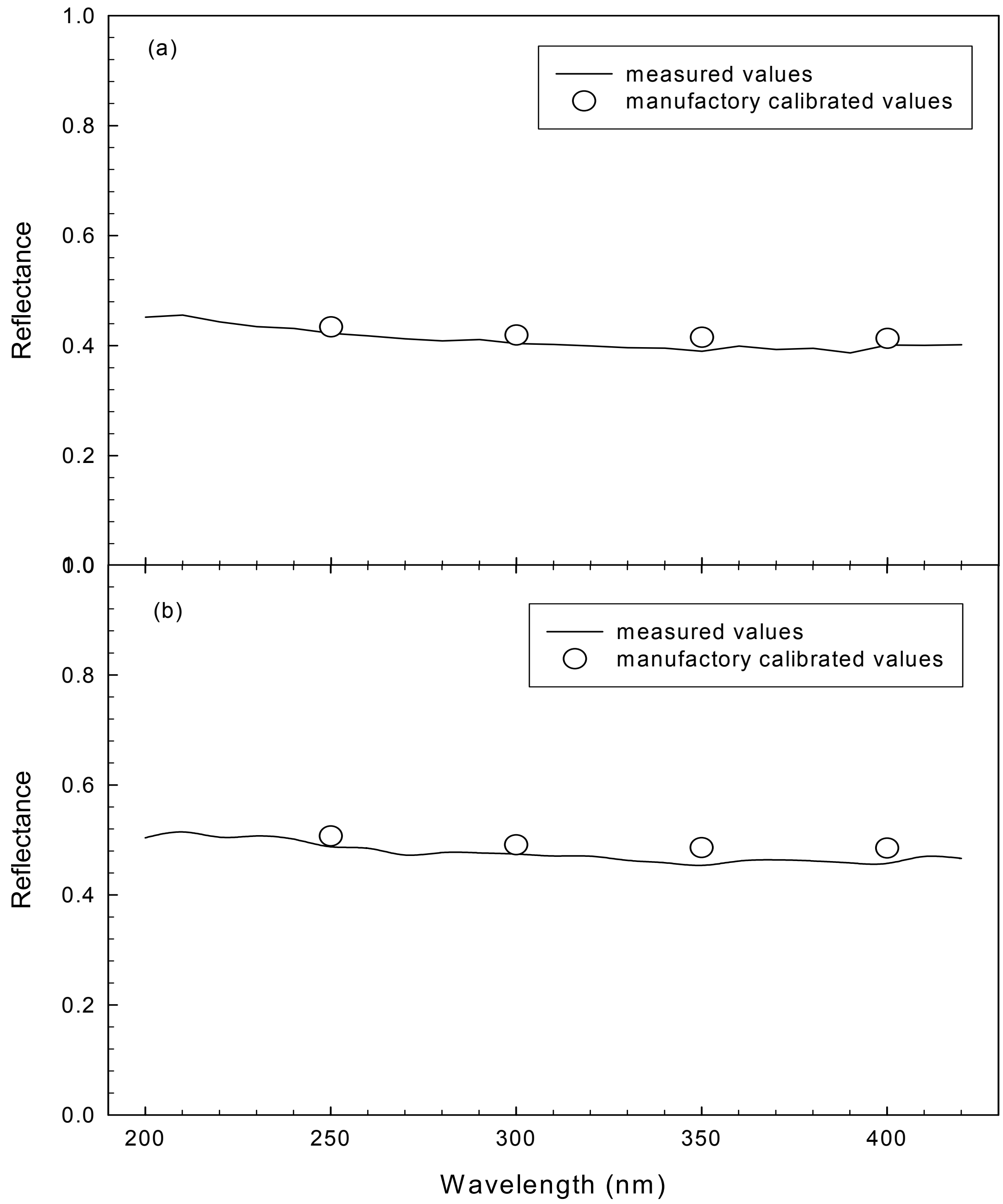

Figure 5.2 Calibration of integrating sphere setup with two reflectance standards: (a) 40% and (b) 50%.

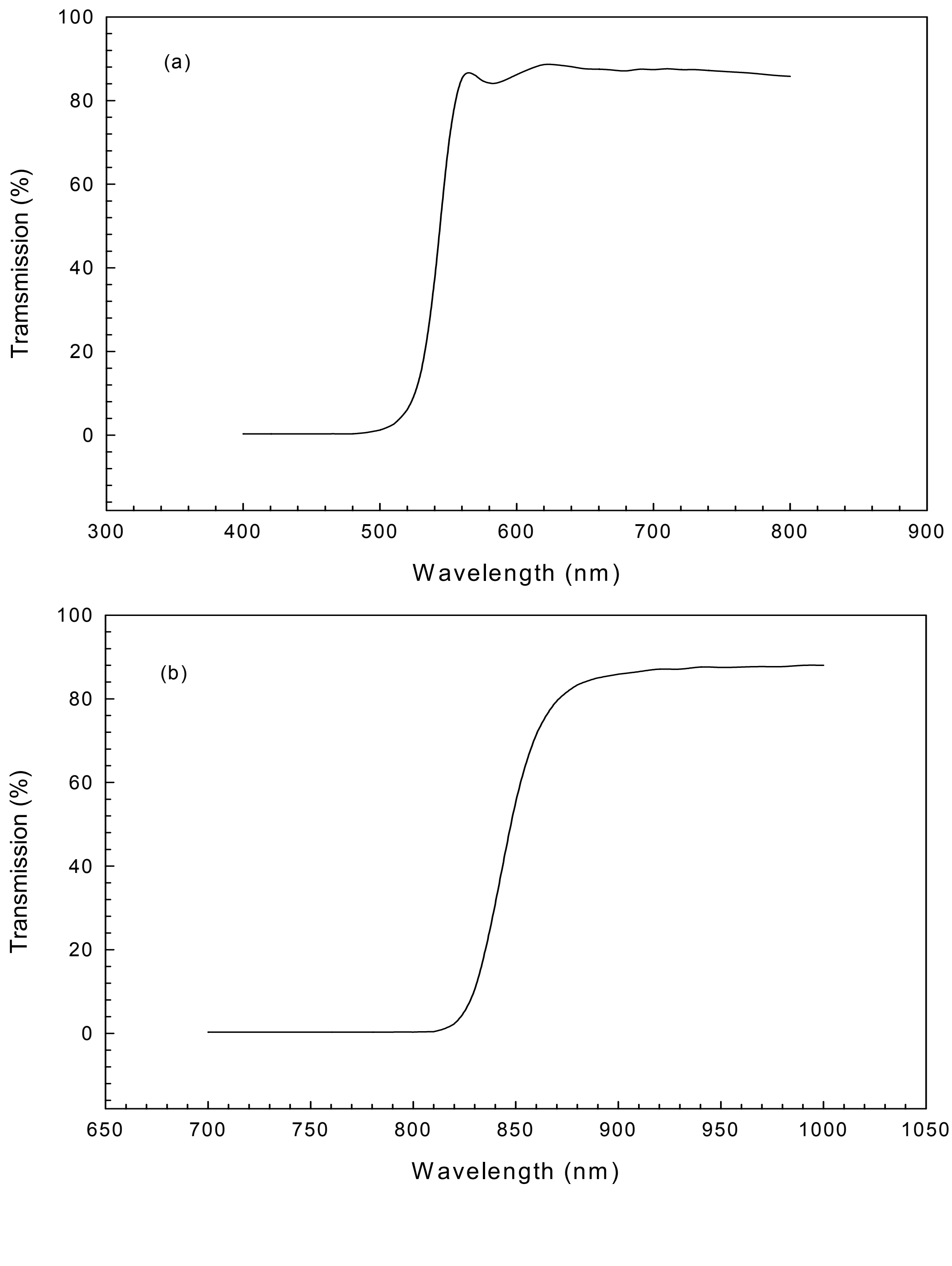

Figure 5.3 Transmission of a longpass filter with a cut-on edge at (a) 540 nm and (b) 840 nm.

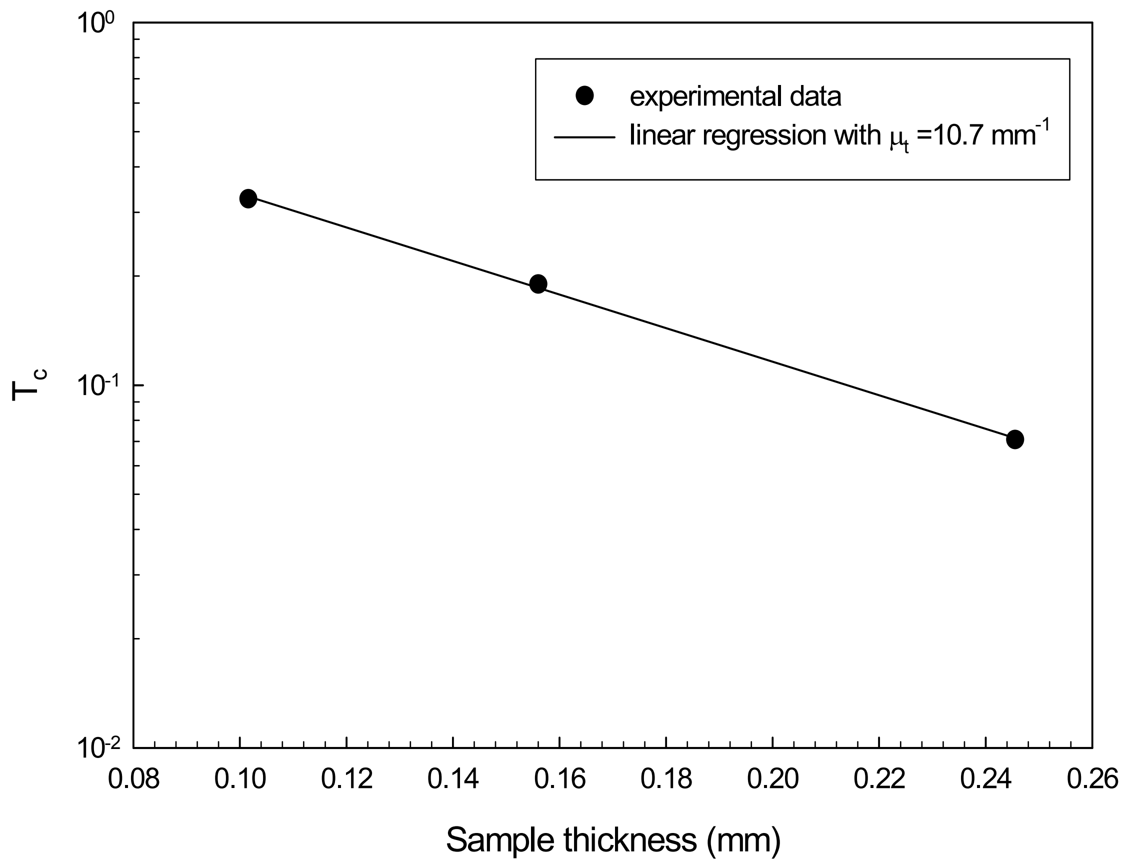

Figure 5.4 Determination of the attenuation coefficient μ_t of a polystyrene microsphere suspension with microsphere concentration of $c_{sp} = 6.186\times10^6$ mm^{-3}. Tc is plotted in log scale.

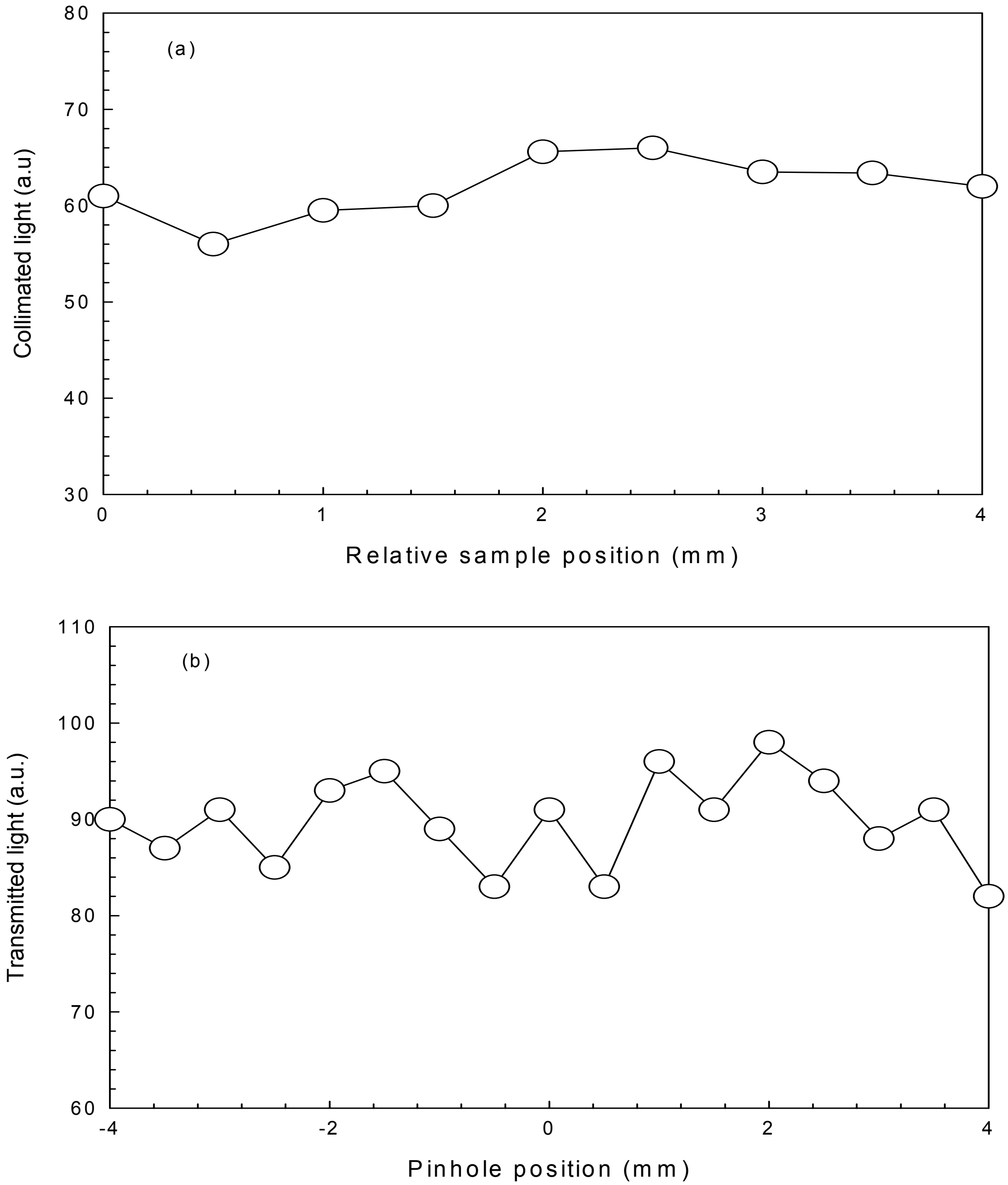

Figure 5.5 (a) the collimated transmission for a porcine dermis sample of 0.54 mm thick at different lateral positions and (b) the light intensity distribution on the focal plane.

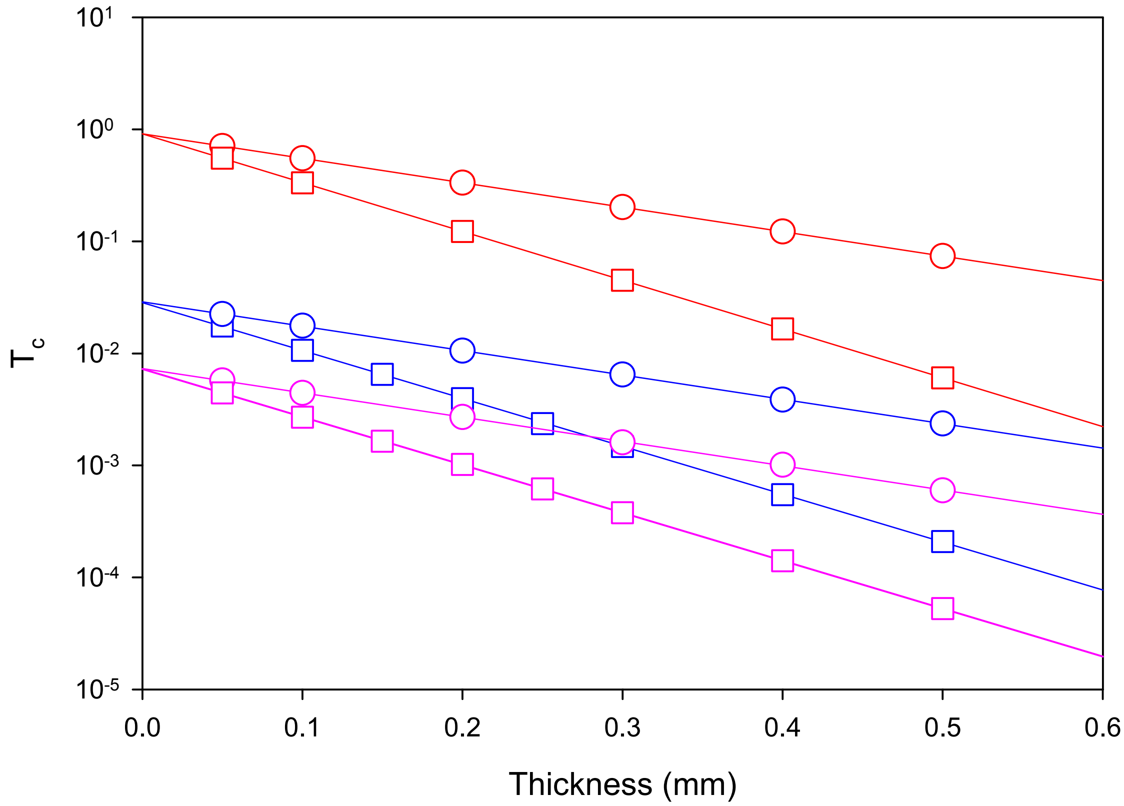

Figure 5.6 Collimated transmission T_c produced by Monte Carlo simulations for flat (red group) and rough (blue group and pink group) surfaces. The Circles within each group represent Tc at the corresponding sample thickness for a set of bulk optical parameter: (μ_s = 5.0 mm^{-1}, μ_a = 0.02 mm^{-1}, g = 0.7) and the squares for a set of bulk optical parameters: (μ_s = 10.0 mm^{-1}, μ_a = 0.02 mm^{-1}, g = 0.7). The surface roughness parameters are (δ = 0.5 μm, a = 10 μm) and (δ = 1.0 μm, a = 10 μm) for blue group and pink group respectively. The solid lines represent the linear regressions with μ_t = 5.026 mm^{-1} and 10.029 mm^{-1} for red group, 5.013 mm^{-1} and 9.851 mm^{-1} for blue group, and 4.996 mm^{-1} and 9.844 mm^{-1} for pink group. T_c is plotted in log scale.

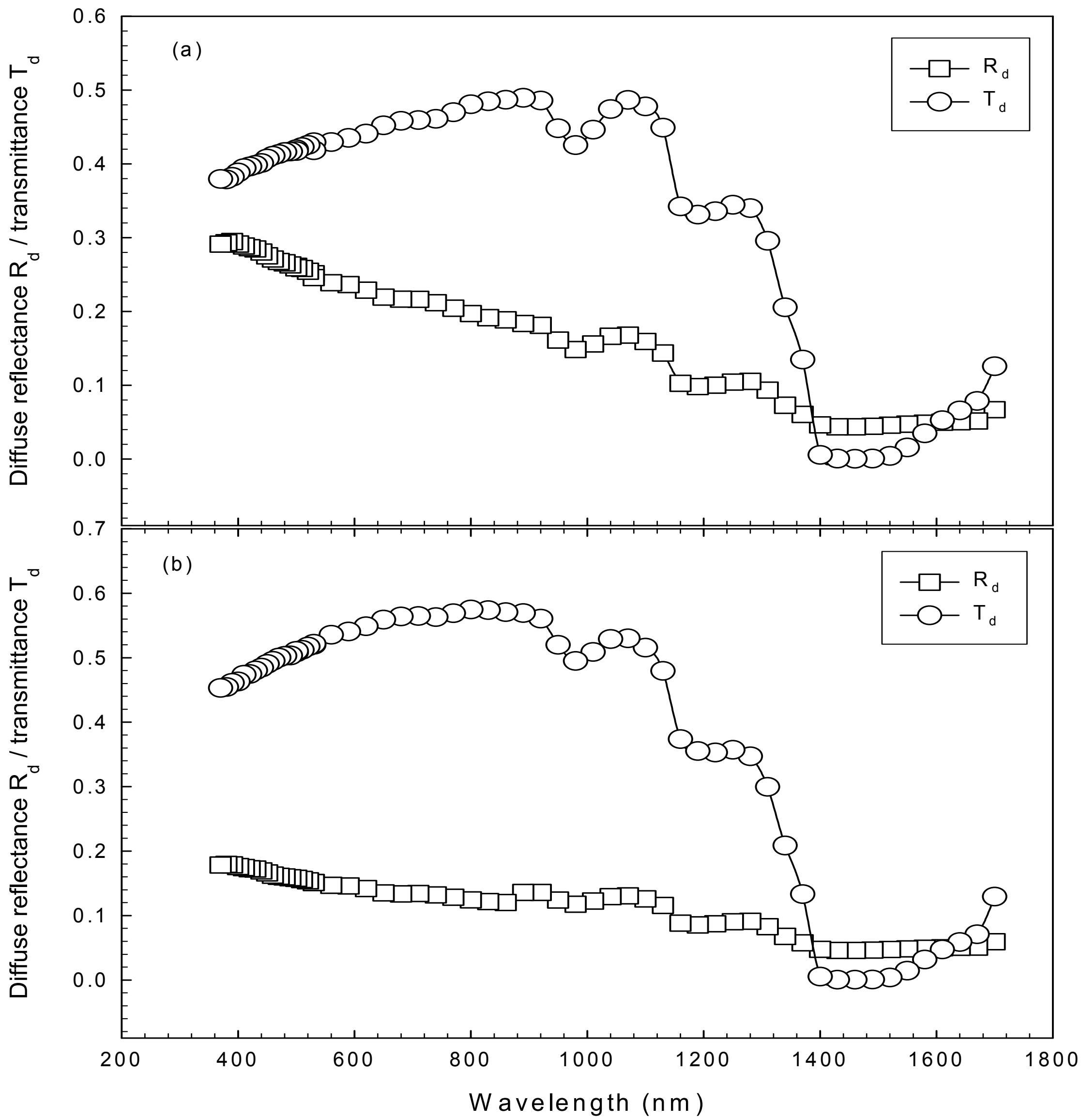

Figure 5.7 Measured diffuse reflectance R_d and transmittance T_d from a polystyrene suspension with microspheres' concentration of (a) 2.709×10^6 mm^{-3} and (b) 1.569×10^6 mm^{-3}. The solid lines are for guide of eye.

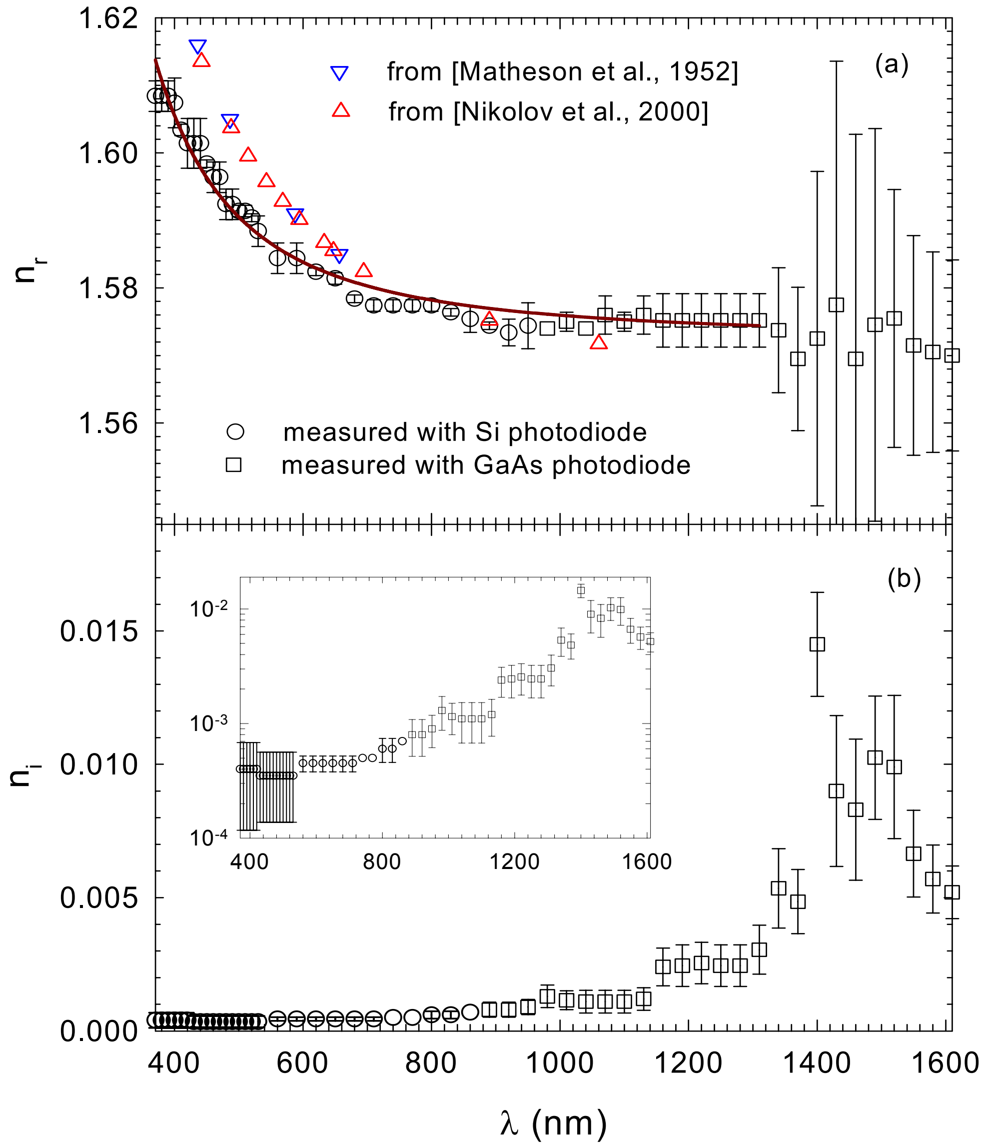

Figure 5.8 Inversely determined refractive indices of the polystyrene microspheres as functions of wavelength: (a) n_r with solid line as the fitting curve based on the Cauchy dispersion formula; (b) n_i, inset: n_i in a log-scale.

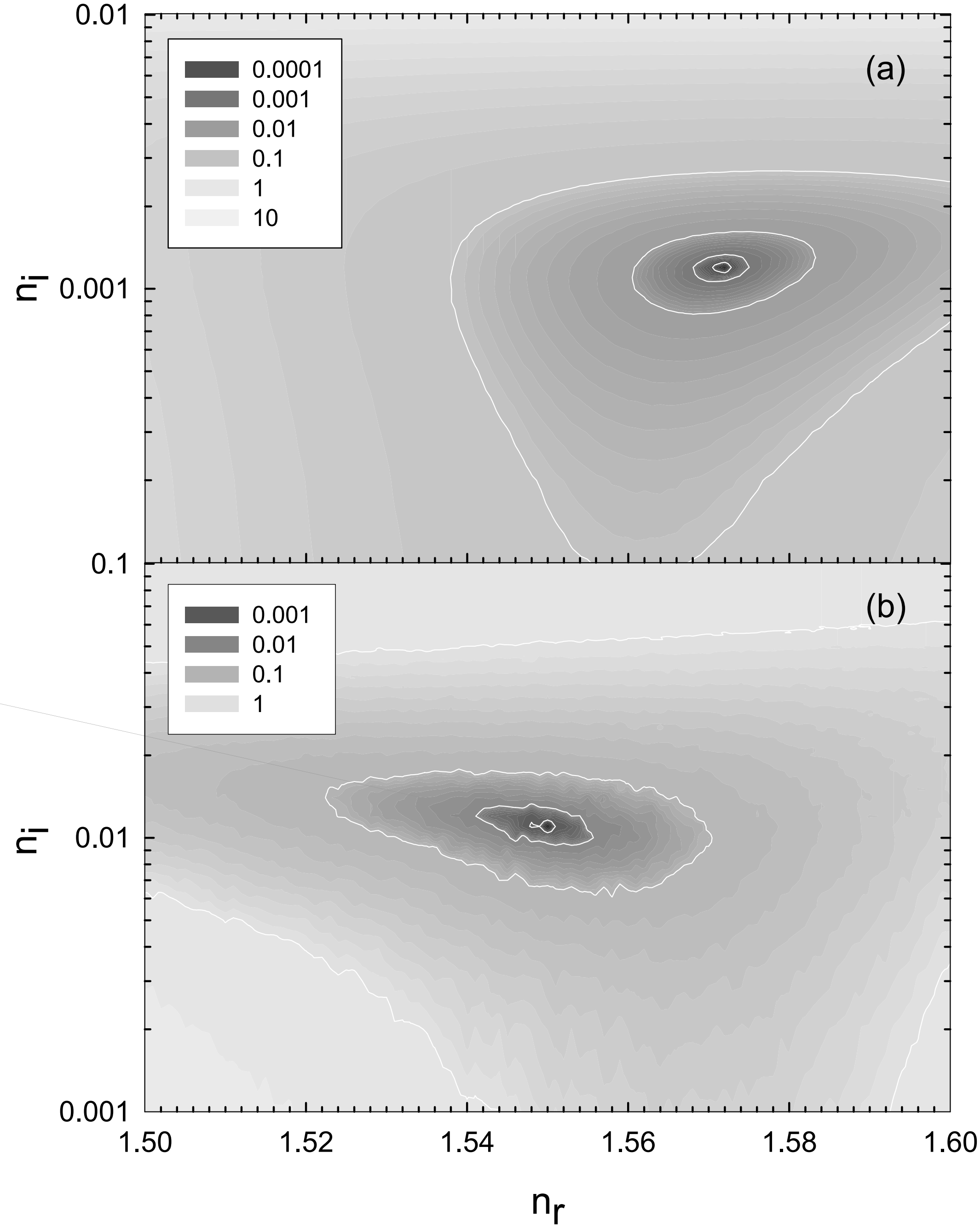

Figure 5.9 Contour plot of the error function Σ in the plane of nr and ni of the polystyrene microsphere in a suspension with $c = 6.186 \times 10^6\ \mathrm{mm}^{-3}$: (a) λ = 950nm; (b) λ= 1430 nm.

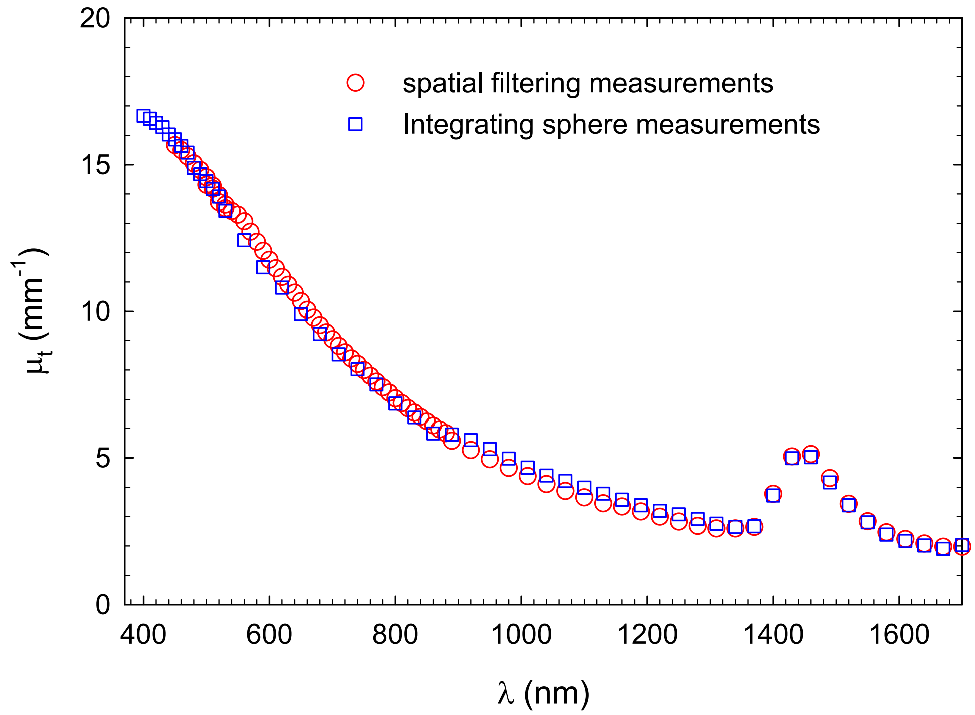

Figure 5.10 Comparison of the attenuation coefficients determined by T_c from the spatial filtering measurements and by R_d and T_d from the integrating sphere measurements for a suspension with concentration $c = 6.186 \times 10^6 \; mm^{-3}$

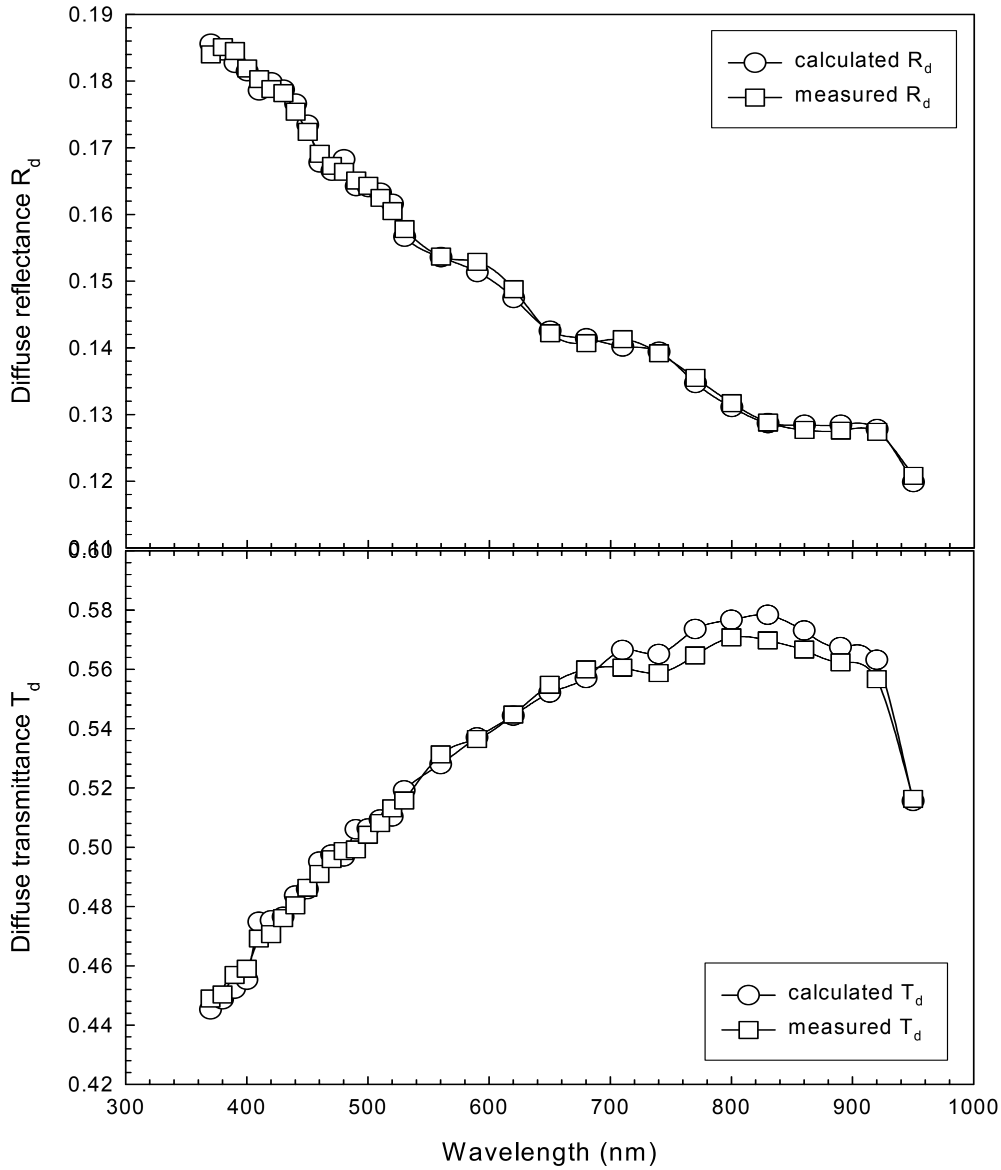

Figure 5.11 Comparison between the calculated and measured (a) R_d and (b) T_d for a polystyrene suspension with a concentration of 1.569×10^6 mm^{-3}. Solid lines are for guide of eye.

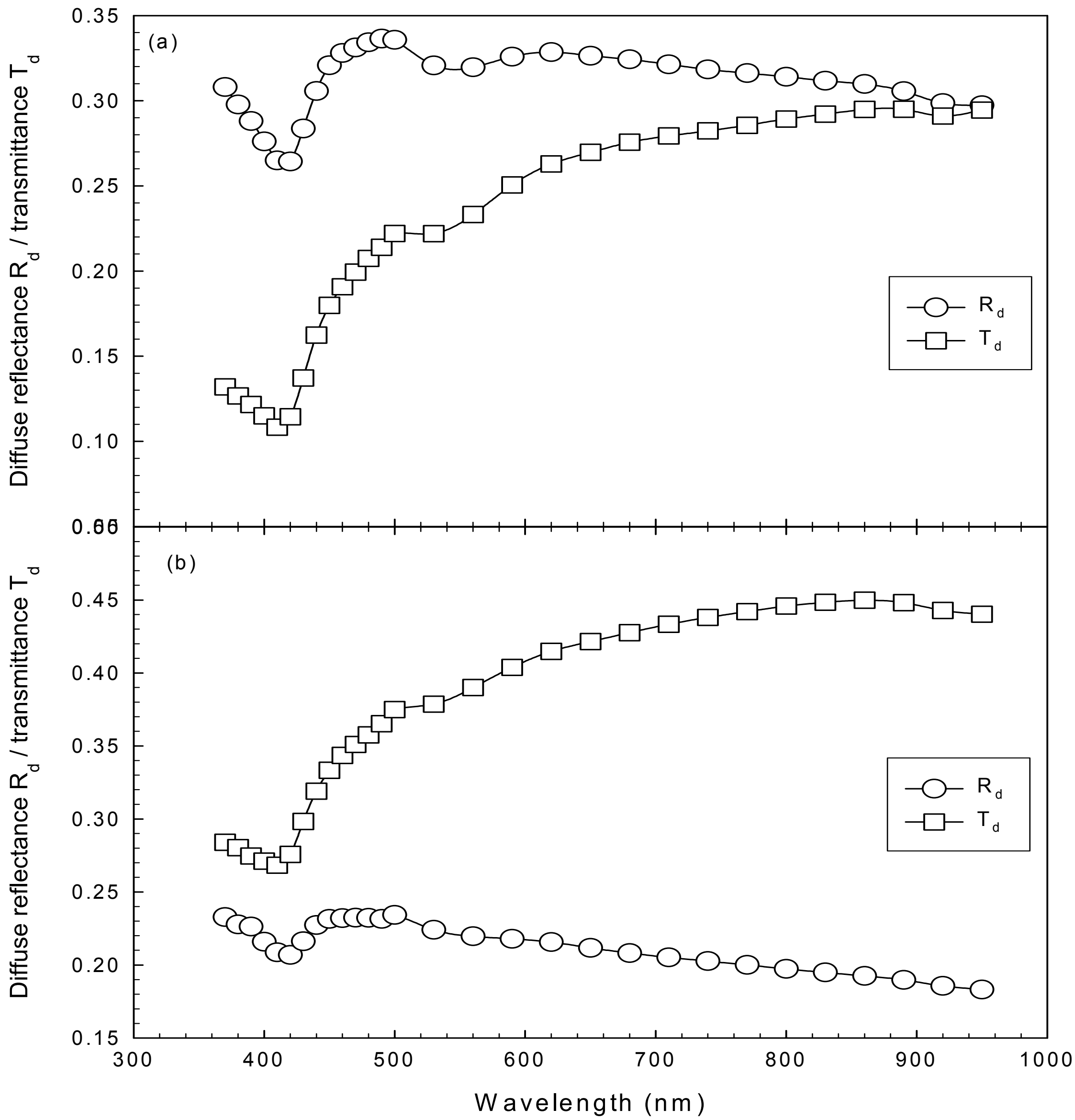

Figure 5.12 Diffuse reflectance R_d and transmittance T_d of two porcine dermis samples with thickness of (a) 1.15 mm and (b) 0.56 mm. The solid lines are for guide of the eye.

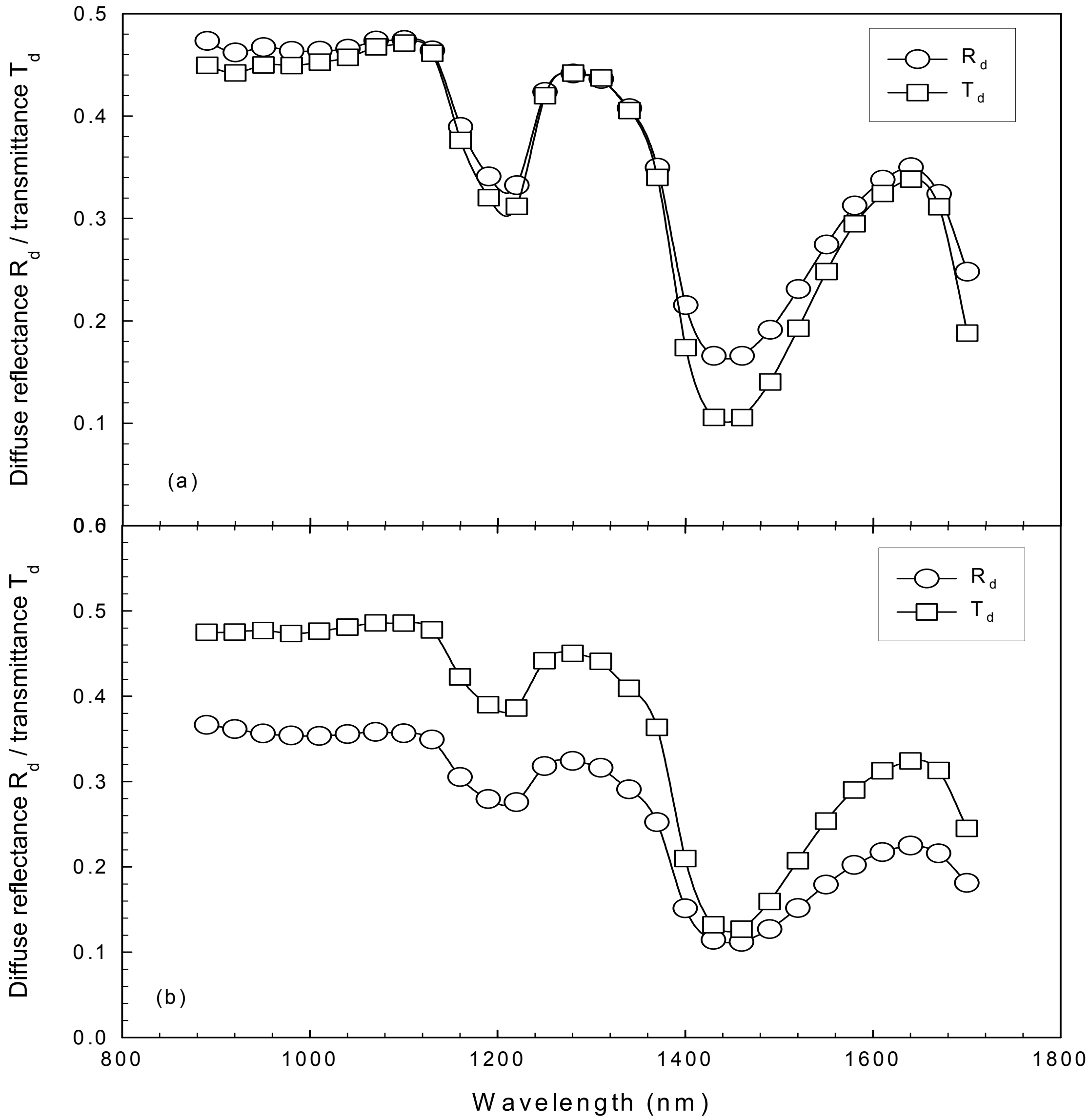

Figure 5.13 Diffuse reflectance Rd and transmittance Td for two porcine dermis samples with thickness of (a) 1.07mm and (b) 0.65mm. The solid lines are for guide of the eye.

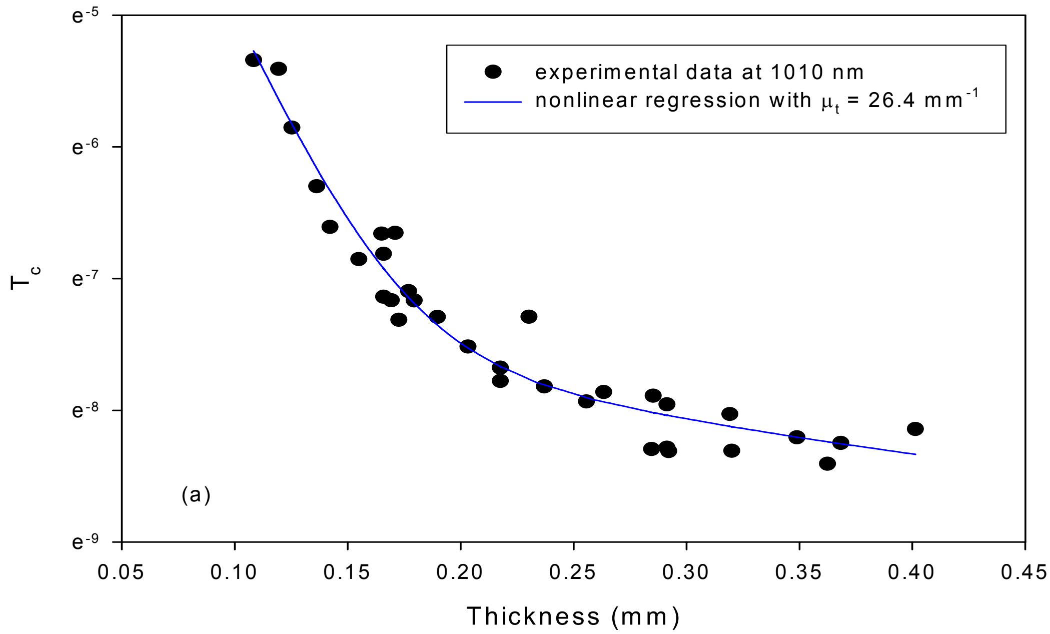

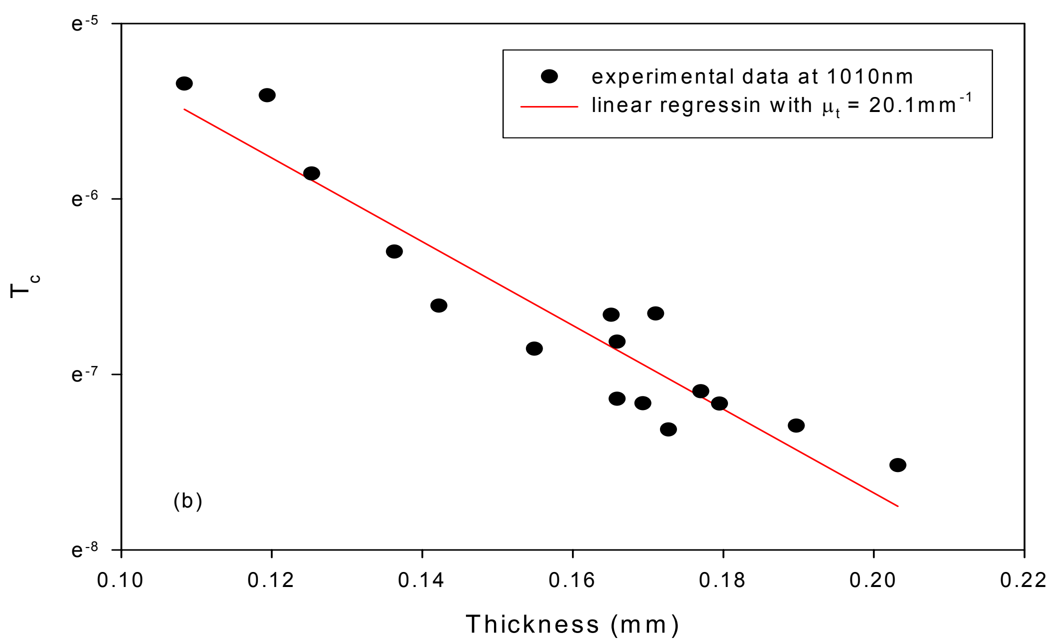

Figure 5.14 Comparison between linear regression and nonlinear regression for the determination of μt from Tc. Tc is plotted in ln scale.

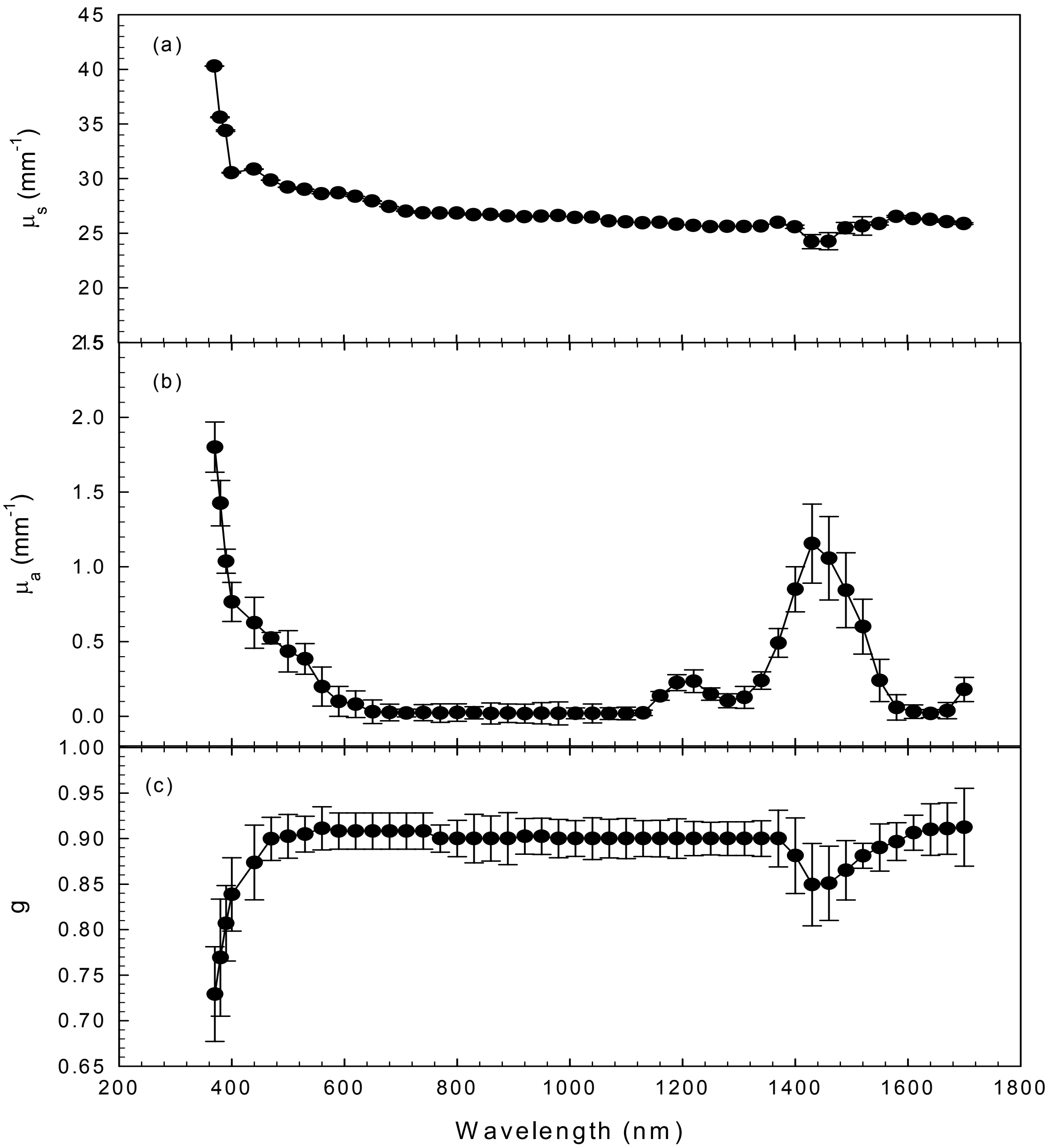

Figure 5.15 The average values of the optical parameters determined under smooth surface assumption for porcine dermis tissue. The error bars represent the standard deviation among 10 samples. The solid lines are for guide of eye.

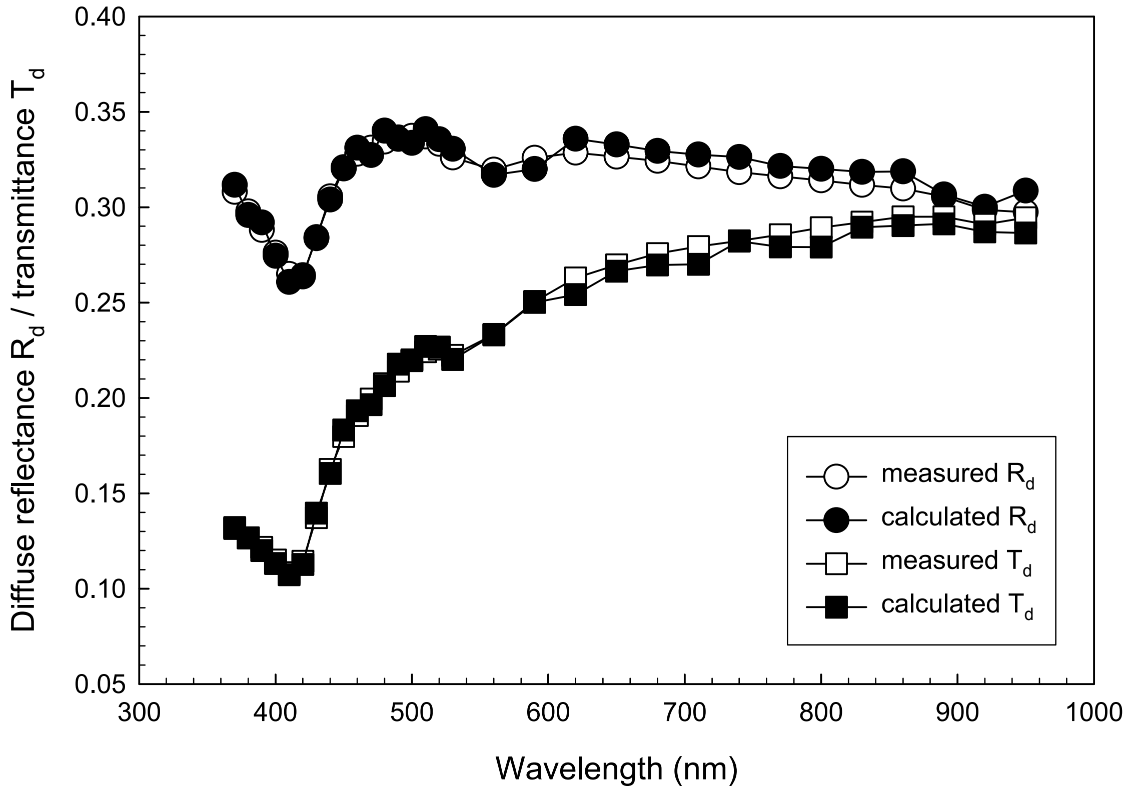

Figure 5.16 Comparison between the calculated and the measured values of R_d and T_d for sample of 1.154 mm thick. The solid lines are for guide of the eye.

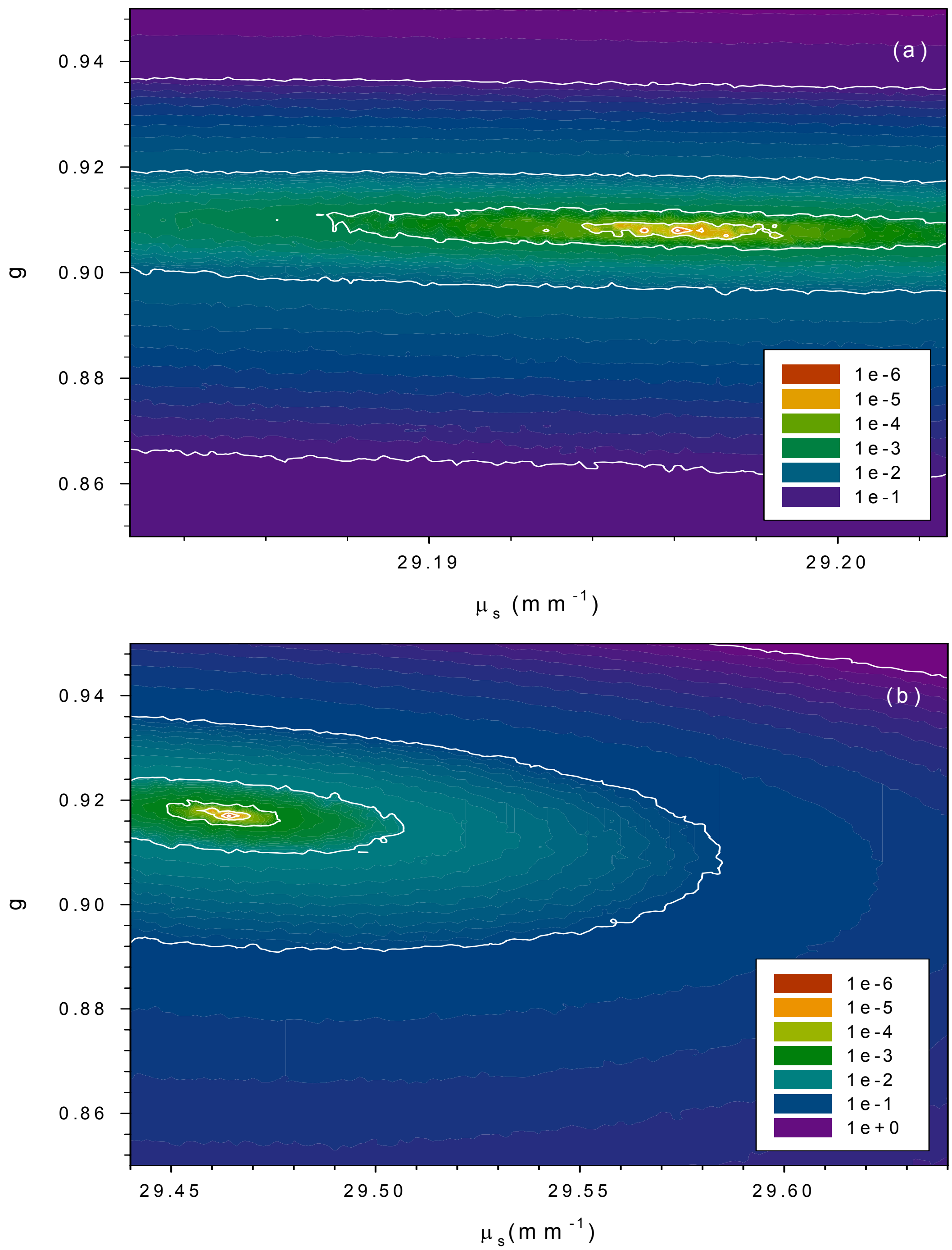

Figure 5.17 Contour plot of the error function Σ in the plane of μs and g for porcine dermis sample of 0.246 mm thick at (a) 500 nm and (b) 1460 nm.

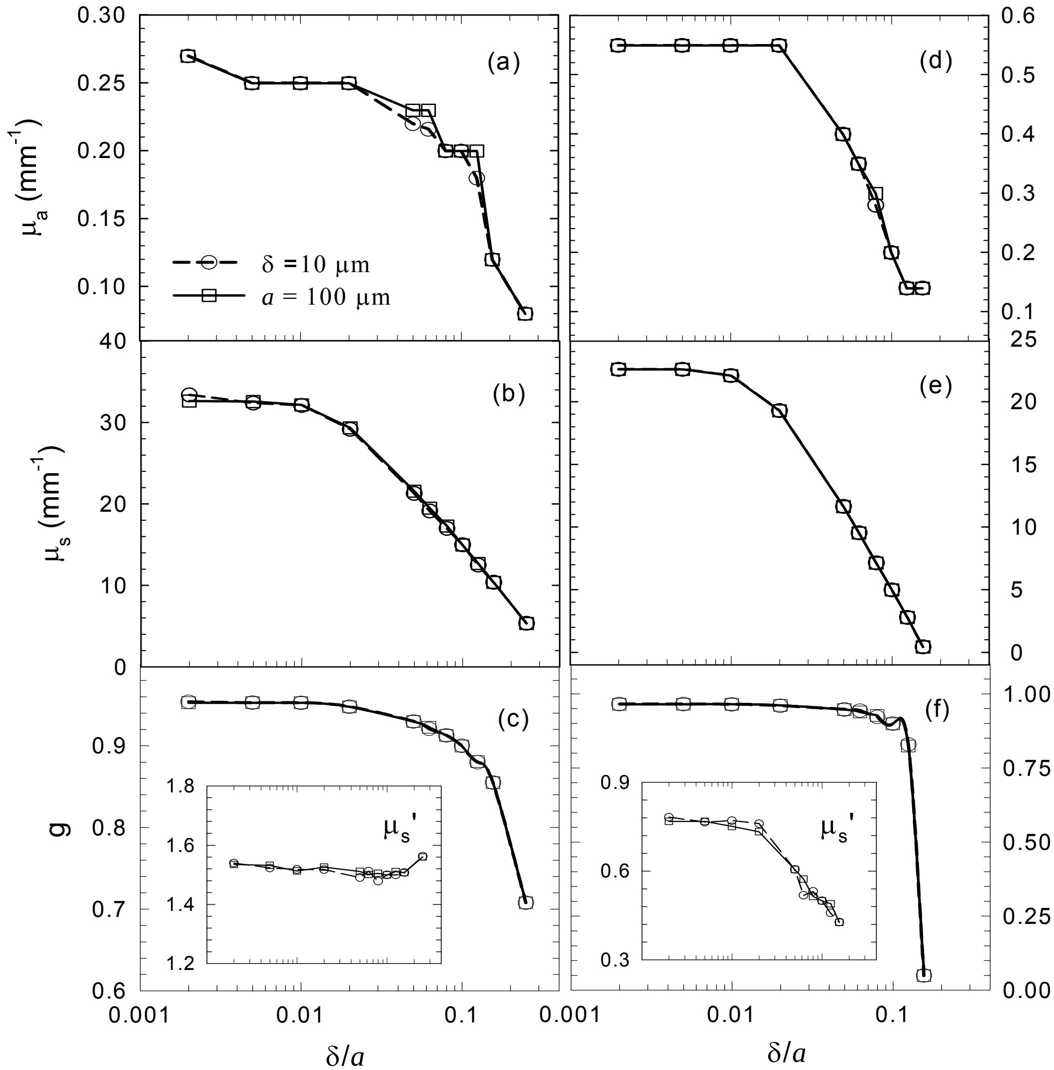

Figure 5.18 Dependence of μ_a, μ_s and g on δ/a. The bulk parameters of the sample for the reference configuration are: μ_{a0} = 0.2 mm^{-1}, g_0=0.90 and (a)-(c): μ_{s0} = 15mm^{-1}; (d)-(f): μ_{s0} = 5mm^{-1}. Other parameters are: thickness=0.20mm, diameter=14mm, n=1.41 for the sample and 3mm, 22mm and 1.51 for the holder plates, respectively. Inserts in (c) and (f): μ_s' as functions of δ/a. Two groups of data are compared in each figure with either δ or *a* kept as a constant and solid lines are for the guide of eyes.

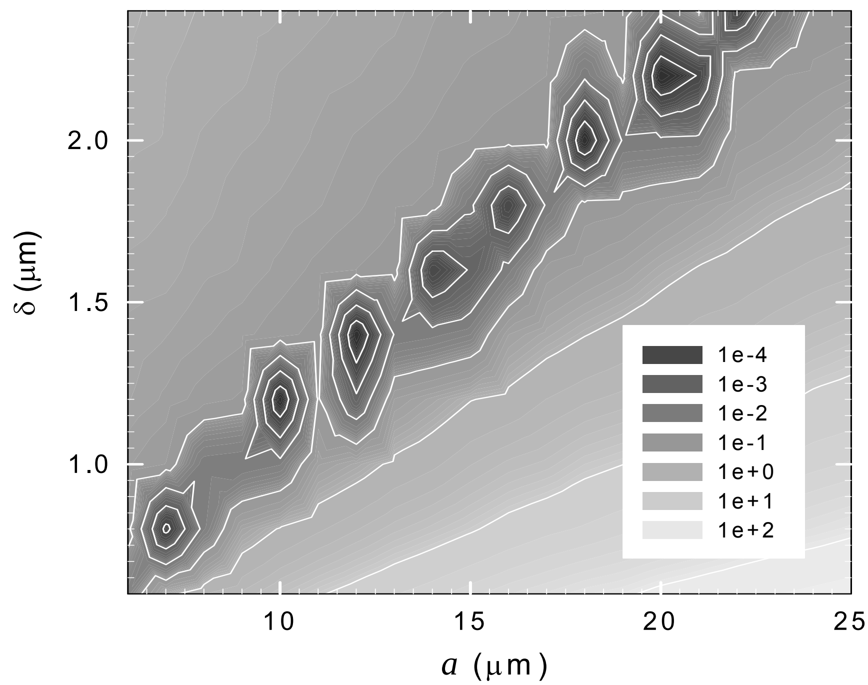

Figure 5.19 Contour plot of the error function Σ versus surface parameters δ and *a* for the intralipid sample between rough windows

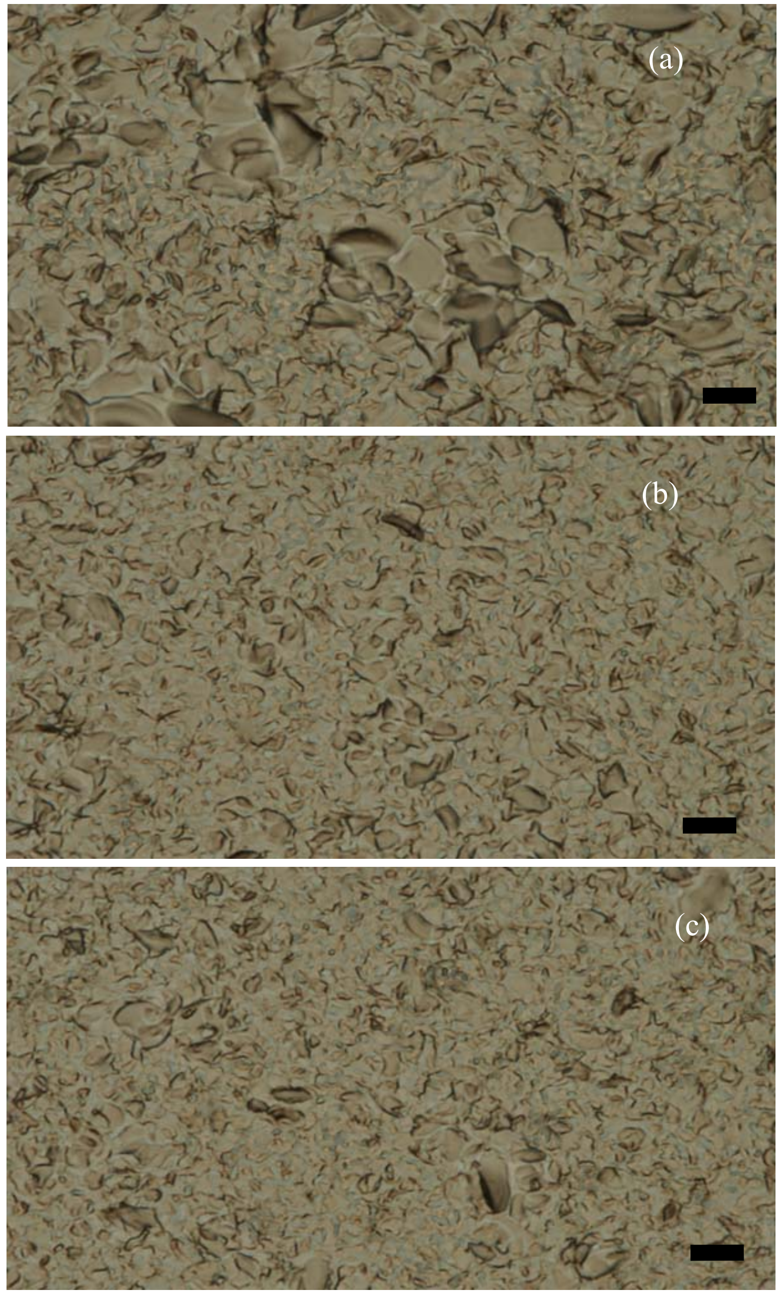

Figure 5.20 Digital microscope images of rough surfaces of glasses grounded with (a) 9.5 μm, (b) 5 μm, and (c) 3μm polishing powder. The black bar in each graph represents 10 μm long.

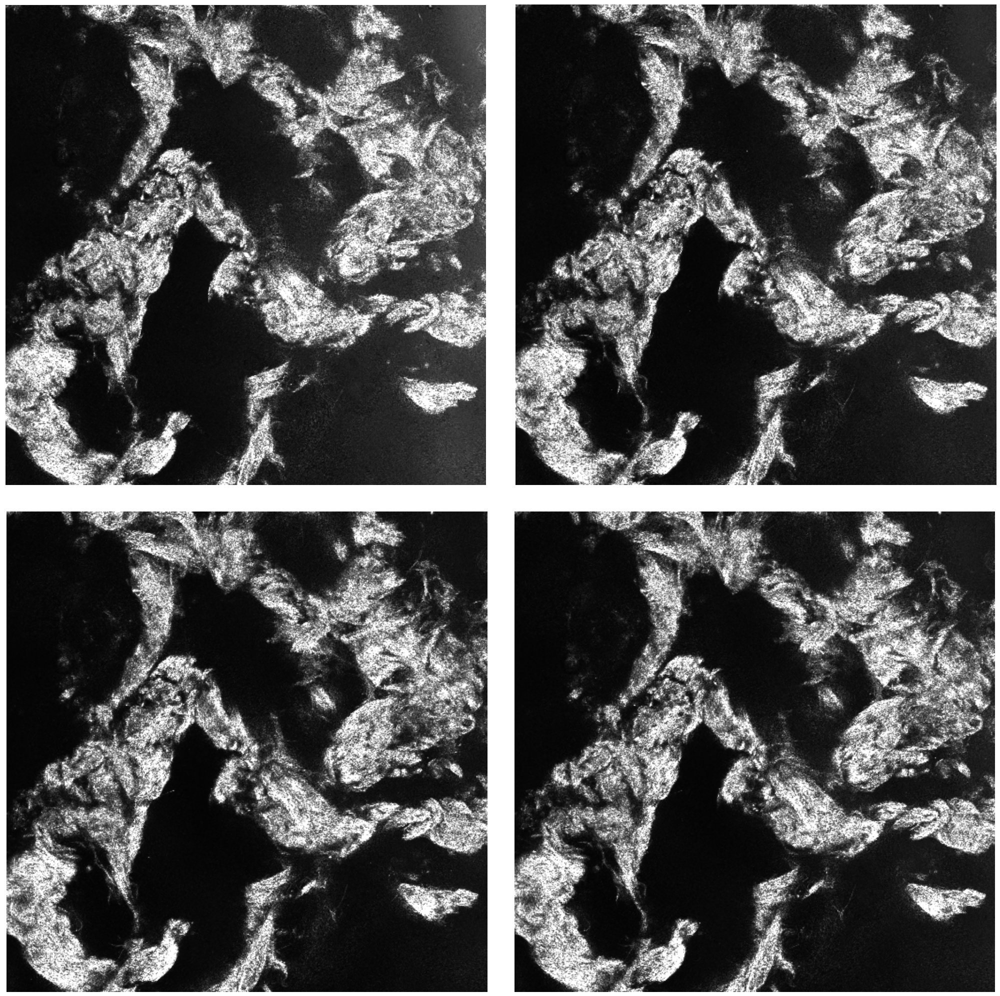

Figure 5.21 Confocal images of a porcine dermis sample.

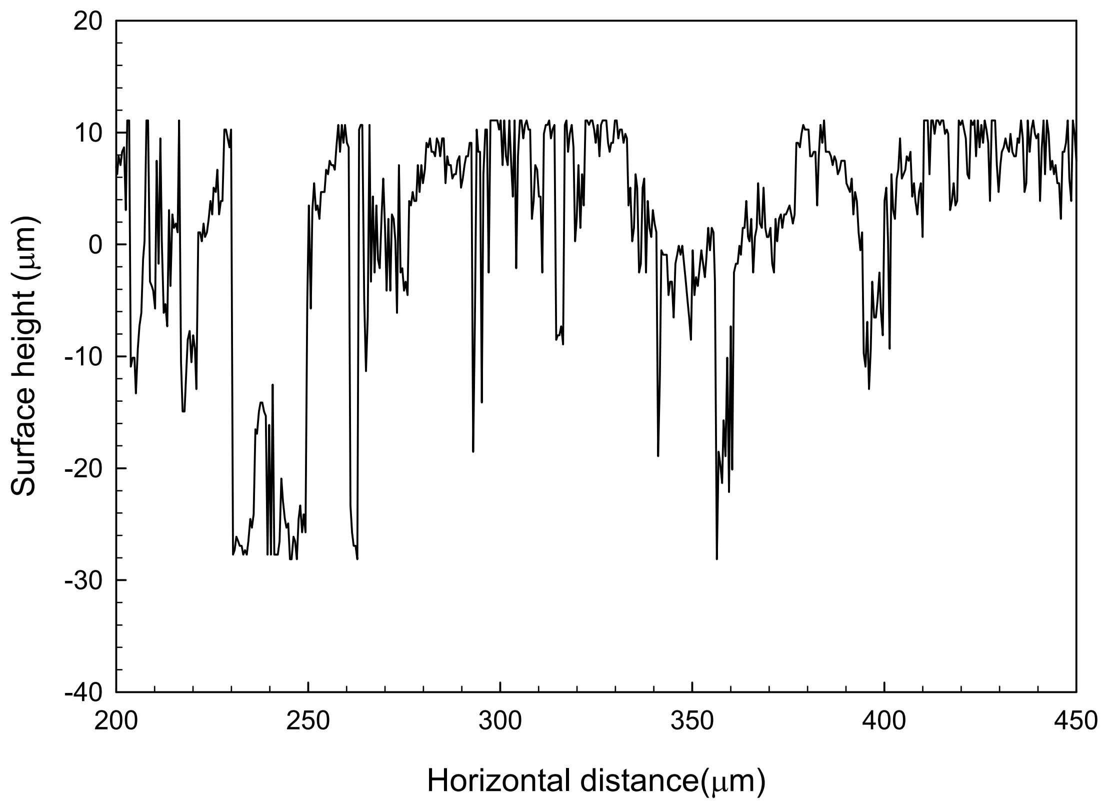

Figure 5.22 A line surface profile for a rough surface with $\delta = 10.39$ μm and $a = 8.10$ μm.

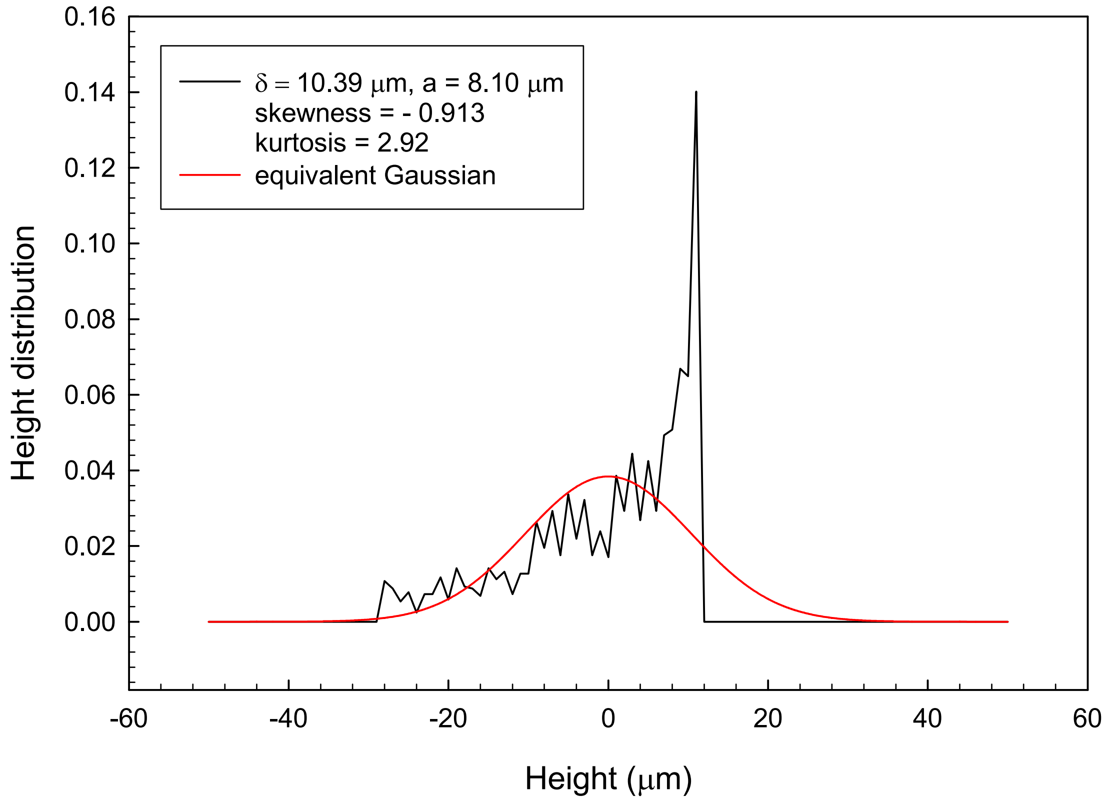

Figure 5.23 Surface height distribution function (black line) with its equivalent Gaussian function (red line) for a rough surface profile.

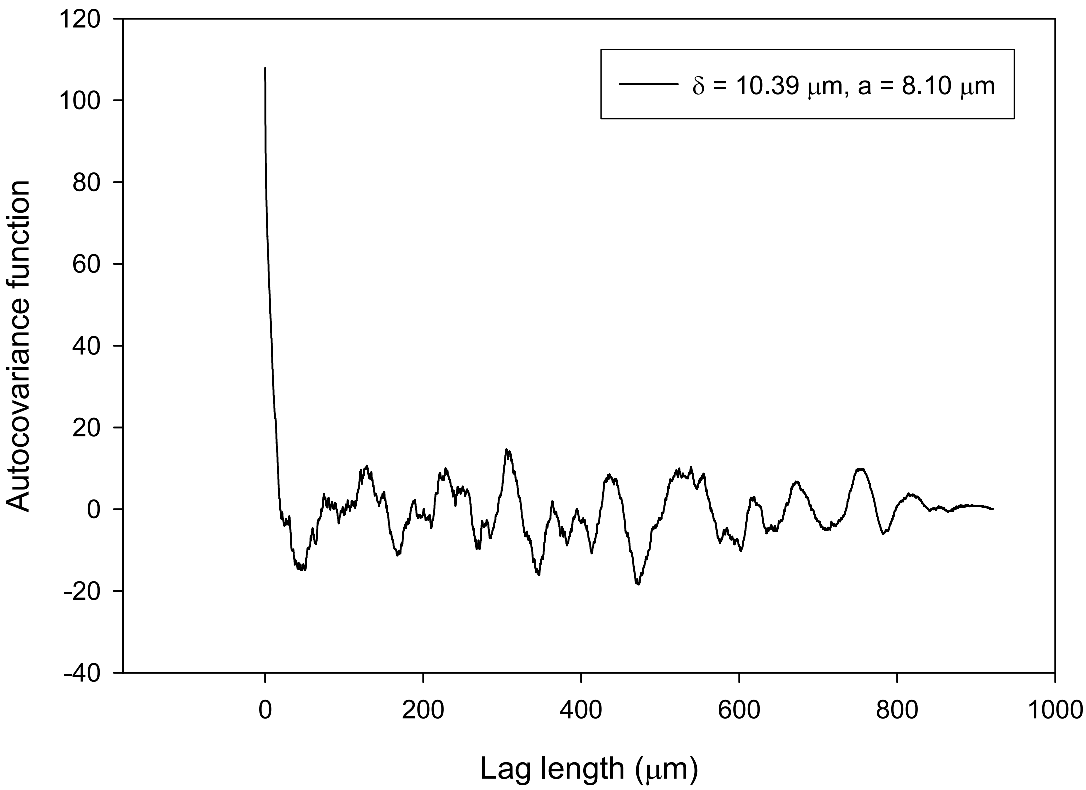

Figure 5.24 Autocovariance function for a rough surface with δ = 10.36 μm and a = 8.10 μm.

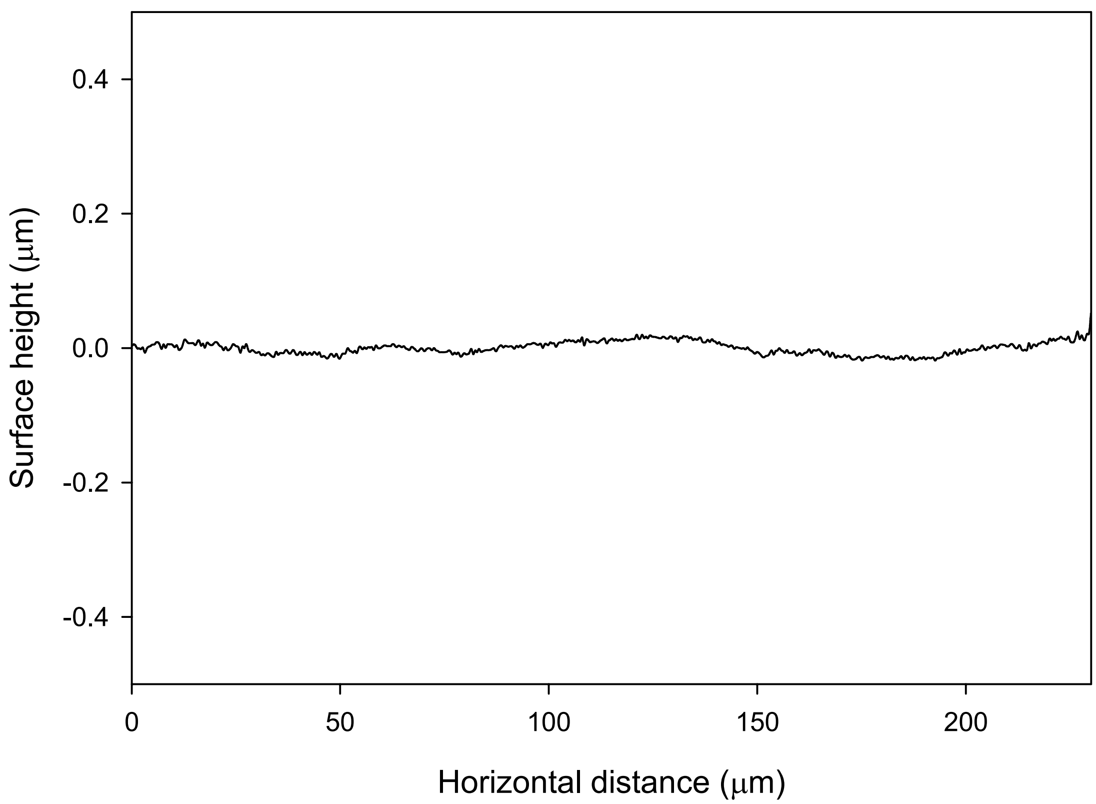

Fig 5.25 Surface profile for an optical flat widow glass reconstructed by confocal imaging.

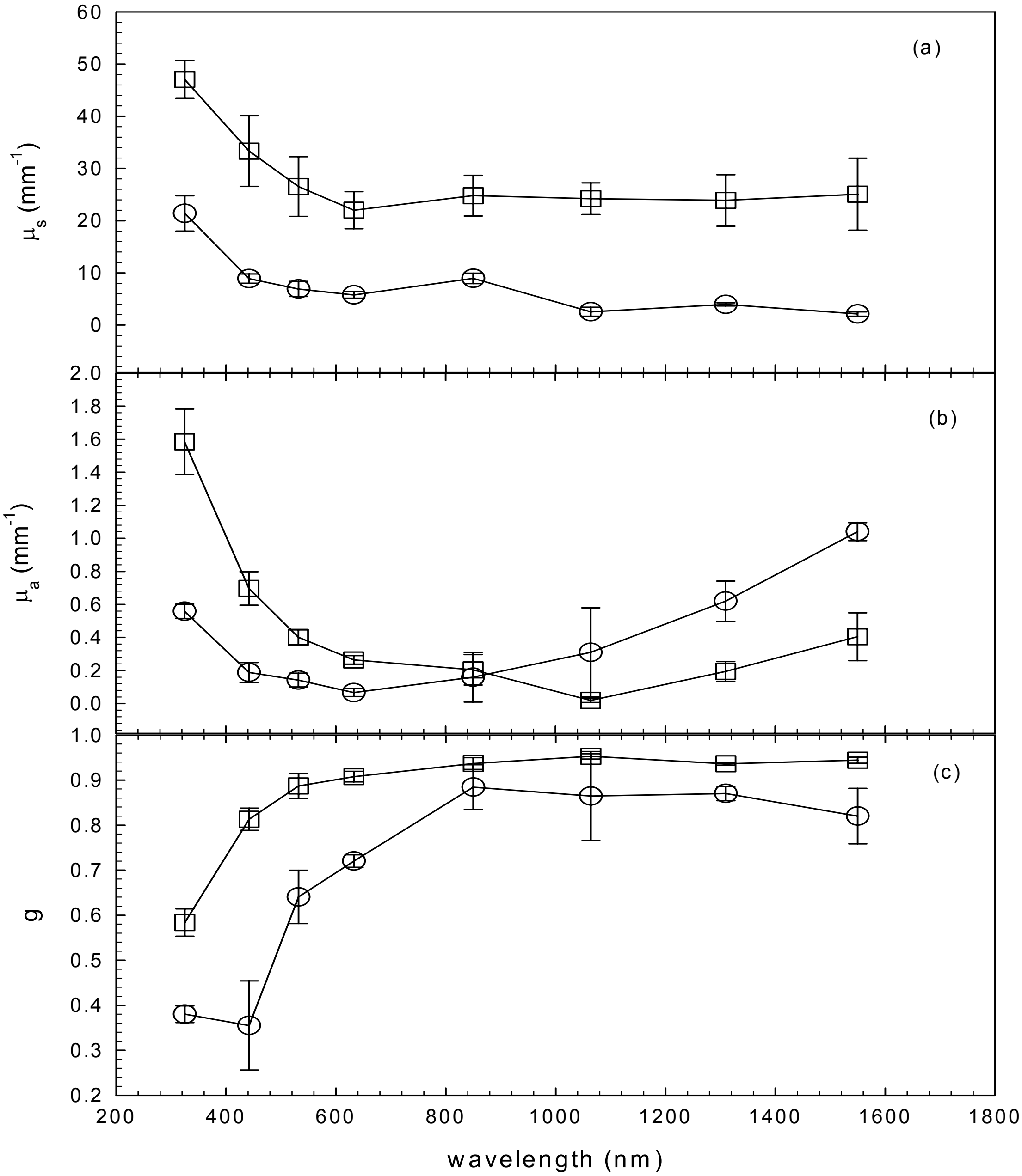

Figure 5.26 Mean values of (a) μ_s, (b) μ_a, and (c) g for porcine dermis tissue. The circles represent data determined under flat surfaces while the squares represent data obtained under rough surfaces. The solid lines are for guide of eye and the error bars are the standard deviation.

Table 5.1 Statistics of surface roughness for three porcine dermis samples

	δ (μm)	a (μm)	Skewness	Kurtosis
Sample 1	5.58 ± 0.42	4.49 ± 1.94	-1.16 ± 0.11	3.71 ± 0.27
Sample2	7.36 ± 1.36	9.98 ± 6.64	-1.03 ± 0.14	3.79 ± 0.30
Sample3	11.59 ± 2.41	12.4 ± 4.97	-0.12 ± 0.35	2.43 ± 0.16

Table 5.2 Sample averaged statistic data of surface roughness for porcine dermis

δ (μm)	8.17 ± 3.01
a (μm)	8.96 ± 5.63
Skewness	-0.7676 ± 0.5262
Kurtosis	3.3067 ± 0.6903

Table 5.3 Statistics of surface roughness for polishing powder grounded glass measured by confocal microscope

Power size (μm)	9.5	5	3	Mexico-6024
δ (μm)	1.46	0.8	0.9	2.23
a (μm)	7.20	4.50	1.80	4.20
Skewness	-2.81×10^{-2}	-1.55	-4.75	0.948
Kurtosis	3.98	3.67	3.33	5.05

Table 5.4 Statistics of surface roughness of polishing powder grounded glasses and a sample (Mexico-6024) measured by AFM

Powder size (μm)	9.5	5	3	Mexico-6024
δ (μm)	0.52	0.34	0.29	0.708
a (μm)	6.75	5.56	4.31	8.00

Chapter 6 Discussions and Summary

The goal of this dissertation research is to develop a system of methods to inversely determine the optical parameters of skin dermis tissues *in vitro* and various tissue phantoms. We have achieved this goal by developing different Monte Carlo codes based on the radiative transfer theory to extract these parameters from the experimental data and investigated the effect of surface roughness on the results of inverse determination.

6.1 Complex Refractive Index of Polystyrene Microsphere

For the real refractive index shown in Fig.5.5 (a), we observe differences between our data of the microspheres and the early results from bulk samples in the visible region, which increases as the wavelength decrease. It has been reported that the magnitude of strain-induced birefringence in elongated polystyrene films increases as the wavelength decreases from 800 to 400nm [Inoue, et al. 1998]. On the basis of these facts we speculate that the difference in n_r is due to the process related residue strain within the microspheres through the photoelastic effect.

An absorption peak can be seen near 1400nm in Fig.5.5 (b) through the wavelength dependence of the imaginary refractive index and is the causes of the anomalous dispersion in the real refractive index. The increased fluctuation, represented by the large error bars, in the real refractive index in the region near 1400nm is attributed to the larger errors in R_d and T_d due to the increased absorption of water near 1450nm

(Hale and Querry 1973) and reduced sensitivity of the GaAs photodiode near 1610nm. We have also found that the absorption of water has a significant effect on the inverse determination of microsphere index for the near-infrared region and its effect has to be taken into account by using the Mie code for absorbing medium. For example, the relative difference between the inversely determined indices of microspheres is increased from $\Delta_r = \left|\frac{n_r^{'} - n_r}{n_r}\right|$ = 0.13% and $\Delta_i = \left|\frac{n_i^{'} - n_i}{n_i}\right|$ = 37% at λ=950nm to Δ_r = 3.0% and Δ_i = 90% at λ=1400nm with $n^{'} = n_r^{'} + i\,n_i^{'}$ as the refractive index determined with the Mie-code without considering water absorption.

6.2 Effects of Surface Roughness on Determination of Bulk Optical Parameters

As shown in Fig. 5.13 the effect of surface roughness is significant on the inverse determination of the bulk parameters of μ_s, μ_a and g. This is especially the case for samples of small optical thickness: μ_s decreases from about 22 to 1mm^{-1} and μ_a from 0.55 to 0.1mm^{-1} when the slope factor δ/a varies between 0.01 and 0.20. The change in μ_s (μ_a) can be understood since the scattering (absorption) coefficient is defined as the probability of photon being scattered (absorbed) per unit of pathlength. For rough samples, more photons are deflected out of the original path at the surfaces than smooth samples. To keep the updated values of R_d and T_d close to the reference, μ_s has to be reduced for rough samples. As a result, average pathlength of tracked photons within the rough sample is increased and μ_a has to be reduced as well to keep the portion of absorbed photons same as the reference configuration. The anisotropy factor g was found to decreases significantly as the surface of the tissue sample become rough and a moderate index mismatch of $\Delta n=0.11$ can severally distort the angular distribution of the light signals. While the effects of roughness on μ_s, μ_a and g are similar for both samples of different optical thickness, the responses of $\mu_s' = (1-g)\mu_s$ to the roughness are profoundly different. As demonstrated by the inserts of Figs.5.13 (c) and (f), μ_s' for the optical thick sample is insensitive to the roughness and μ_s' of the optical thin sample changes with roughness similar to that of μ_s, indicating that in the single scattering or nondiffusive regime light signals are significantly affected by the surface roughness. These results strongly suggest that the effect of surface roughness needs to be carefully analyzed even for *in vivo* determination of bulk tissue optical parameters from the reflectance measurement where the nondiffusive regime dominates the light remitted from superficial layer of the tissue near the light source.

6.3 Optical Parameters for Porcine Dermis Tissue

Optical parameters determined under the assumption that sample surfaces are flat and smooth for porcine dermis tissue, as presented in Fig 5.15 show the similar results with the previous reports in the near infrared from 900 nm to 1700 nm [Du et al 2001]. As expected, the response of the dermis tissue to the near infrared light is dominated by scattering. And the anisotropy factor g remains approximately constant around 0.9 from 900 nm to 1400nm and that indicates the forward tendency of light scattering by dermis. An absorption peak located between 1400 and 1500 nm is believed to associate with water absorption [Hale and Querry 1973]. In the spectral region between 370 nm and

900nm, dermis still shows scattering dominant feature and g as well as remains approximately constant until about 600nm. Both the scattering coefficient μ_s and the absorption coefficient μ_a start increase while the anisotropy factor g begins to decrease.

As shown in Fig 5.26, the surface roughness corrected optical parameters for dermis tissue exhibit. Both μ_s and g decrease significantly by comparison with their counterparts determined under the assumption of flat surfaces, as predicted by our numerical analysis in section 5.4. However, surface roughness corrected μ_a decrease in comparison with the flat surface derived μ_a below 850nm, but increase above 850nm.

The current version of Monte Carlo code requires a big static memory to store the 2-dimentional surface profile generated according to Gaussian distribution. For example, about 1Gbyte memory is required to generate a rough surface profile with a lateral resolution of 3 μm on a square area of 6×6 mm. For a rough surface with a 10 μm lateral correlation length, 1 GB memory barely reaches the minimum requirement to sample a surface profile. From a surface maximum to its minimum only three points are sampled.

6.4 Summary

In this dissertation, a theoretical and experimental investigation of optical properties of skin tissue and polystyrene microsphere suspensions is presented. This research is part of the ongoing research efforts in the Biomedical Laser Laboratory at East Carolina University to develop a system of experimental methods and theoretical models for accurate determination of optical parameters of mammalian tissues, which are fundamental to many biomedical applications of optical technologies. As a result of this investigation, the complex refractive index of polystyrene in the form of microsphere is obtained as a function of wavelength from 370 nm to 1610nm for the first time to our knowledge. We have developed a Monte Carlo based inverse procedure to extract the bulk optical parameters from the measured light signals with surface roughness on scales close to the wavelength of light. It has been shown clearly that the surface roughness can significantly affect the values of bulk tissue optical parameters (including μ_a) inversely determined from *in vitro* or *in vivo* measurements even for a moderate index mismatch. As a consequence, surface roughness corrected optical parameters of porcine dermis tissue have been determined at 325, 442, 532, 632.8, 850, 106.4, 1330, and 1550 nm in comparison with ones as a function of wavelength between 370 nm to 1700nm without considering the surface roughness. In the future, we plan to upgrade our Monte Carlo code to use the dynamic rough surface generation procedure to reduce the memory requirement and improve the lateral simulation resolution. Other methods of fast Monte Carlo and efficient inverse algorithms should be developed in order to achieve *in vivo* determination of tissue optical parameters and clinical applications.

Bibliography

Alfano R R (1994). Advances in Optical Imaging and Photon Migration vol.21 of OSA Proceeding Series (Optical society of America, Washington, DC).

Anderson R R and Parrish J A (1981). "The optics of human skin", J. Invest. Dermato. 77, 13-19.

Baumberger J P, Suntzeff V and Cowdry E V (1942). "Methods for the separation of epidermis from dermis and some physiologic and chemical properties of isolated epidermis", *J. Natl. Cancer. Inst.* 2, 413-23.

Beck J F, Van Staveren M J, Posthumus P, Sterenborg H J and Van Gemert M J (1997). Phys. Med. Biol. 42, 2263.

Bennett J M and Mattsson L (1999). "Introduction to Surface Roughness and Scattering", 2nd Edition, Optical Society of America.

Bohren C F and Huffman D R (1983). "Absorption and scattering of light by small particles", New York, Wiley.

Born M and Wolf E (1999). *Principles of Optics* (7th edition) (UK: Cambridge University Press).

Cashwell E D and Everett C J (1959). "A Practical Manual on the Monte Carlo Method for Random Walk Problems", Pergamon Press, New York.

Chan K P, Yamada M, Devaraj B and Inaba H (1995). "Optical imaging through highly scattering media by use of heterodyne detection in the 1.3 µm wavelength region", Opt. Lett. 20, 492-4

Chandrasekhar S (1950). *Radiative Transfer* (London: Oxford University Press)

Cheong W F, Prahl S A, And Welch A J (1990). "A review of the optical properties of biological tissues", *IEEE J. Quantum Electron.* 26, 2166-85.

Chylek P (1977). "Light scattering by small particles in an absorbing medium", J. Opt. Soc. Am. 67, 561-3.

Du Y (2000). "Optical properties of porcine dermis in the near infrared region between 900 nm and 1500 nm", MS Thesis, Department of Physics, East Carolina University

Du Y, Hu X H, Cariveau M, Ma X, Kalmus G W and Lu J Q (2001). “Optical properties of Porcine skin dermis between 900 nm and 1500 nm”, *Phys. Med. Biol*. 46, 167-81

Elson J M and Bennett J M (1979). “Relation between the angular dependence of scattering and the statistical properties of optical surfaces”, J.Opt.Soc.Am. 69, 31- 47.

Flock S T, Jacques S L, Wilson B C, Star W M and Van Gemert M J (1992). Lasers Surg. Med. 12, 510.

Francon M (1979). ‘Laser Speckle and Applications in Optics’, Academic Press, New York.

Fu Q and Sun W B (2001). “Mie theory for light scattering by a spherical particle in an absorbing medium”, Appl. Opt. 40, 1354-61.

Gordon S K and Timothy R C (1989). “Confocal scanning microscopy”, Physics Today. 9, 55-62.

Graaff R, Dassel A C M, Koelink M H, De Mul F F M and Aarnoudse J G (1993). “Optical properties of human dermis *in vitro* and *in vivo”*, Appl. Opt. 32, 435-47.

Groenhuis R A J, Ferwerda H A and Bosch J J T (1983). “Scattering and absorption of turbid materials determined from reflection measurements. 1: Theory”, Appl. Opt. 22, 2456-62.

Hale G and Querry M (1973). “Optical constants of water in 200 nm to 200 micrometer wavelength region”, Appl.Opt.12, 555-63.

Hardy J D, Hammel H T and Murgatroyd D (1956),” Spectral transmission and reflectance of excised human skin”, *J. Appl. Physiol.* 9, 257-264

Hee M R, Izatt J A, Jacobson J M, Fujimoto J G and Swanson E A (1993). “Femtosecond transillumination optical coherence tomography”, Opt. Lett. 18, 950-2

Henderson B W and Dougherty T J (1992). “Photodynamic Therapy: Basic Principles and Clinical Applications”, Marcel Dekker Inc., New York.

Henyey L G and Greenstein J L (1941). “Diffusion radiation in galaxy”, *Astrophys. J.* 93, 70-83.

Horinaka H, Hashimoto K, Wada K Cho Y and Osawa M (1995). “Extraction of quasistraightforward-propagating photons from diffused light transmitted through a scattering medium by polarization modulation”, *Opt. Lett.* 20, 1501-3

Huang D, Swanson E A, Lin C P, Schuman J S, Stinson W G, and Fujimoto G (1991). "Optical coherence tomography", Science, vol.254, 1178-1181.

Hull E L, Nicholas M G, and Foster T H (1998). "Quantitative broadband near-infrared spectroscopy of tissue-simulating phantoms containing erythrocytes", Phys. Med. Biol. 43, 3381-3404.

Inoue T, Kuwada S, Ryu D S and Osaki K (1989). "Effects of wavelength on train-induced birefringence of polymers", Polymer J. 30, 929-34.

Ishimaru A (1978). Wave propagation and scattering in random media (New York: Academic)

Ishimaru A (1989), "Diffusion of light in turbid material", *Appl. Opt.* 28, 2210-15

Jackson J D (1962). 'Mathematics for Quantum Mechanics', W.A. Benjamin, New York.

Jacques S L, Alter C A, Prahl S A (1987). Lasers Life Sci. 1, 309-333

Jacques S L, Prahl S A (1987). Lasers in Surgery and Medicine, vol.6, 494-503.

Jacquez J A and Kuppenheim H F (1955). "Theory of the integrating sphere", *J.Opt. Soc. Am.*45, 450-70

Kalos M H and Whitlock P A (1986). " Monte Carlo Methods, I: Basics", John Wiley & Sons, Inc.

Keijer M, Jacques S T, Prahl S A and Welch A J (1989). "Light distribution in artery tissue: Monte Carlo simulations for finite-diameter laser beam", Lasers Surg. Med. 9, 148-154.

Kienle A, Forster F K, and Hibst R (2001). "Influence of the phase function on determination of the optical properties of biological tissue by spatially resolved reflectance", Opt. Lett. 26(20), 1571-1573.

Kettman J R and Davis T, Chandler D, Oliver K G and Fulton R J (1998). "Classification and properties of 64 multiplexed microsphere sets", Cytometry 33, 234-243.

Korsch D (1991). *Reflective Optics* (San Diego: Academic Press)

Kubelka P (1948). "New contributions to the optics of intensely light-scattering materials: Part 1", *J. Opt. Soc. Amer.* 38, 448-57

Kubelka P (1954), "New contributions to the optics of intensely light-scattering materials: Part 2", *J. Opt. Soc. Amer.* 44, 330-35

Lavker R M, Dong G, Zheng P S and Murphy G F (1991). "Hairless micropig skin: A novel model for studies of cutaneous biology", *Am. J. Pathol.* 138 687-97

Lembares A, Hu X H, and Kalmus G W (1997). "Absorption spectra of the cornea in the far ultraviolet region", Invest. Ophthalmol. Vis. Sci. 38, 1283-87.

Lu J Q, Hu X H, Dong K (2000). "Light Distribution of a Converging Laser Beam in a Two-layer Skin Model with Rough Interfaces", *Applied Optics*, **39**, 5890-5897

Ma X, Lu J Q, Brock R S, Jacobs K, Ping Y, and Hu X (2003). "Determination of complex refractive index of polystyrene microspheres from 370 to 16100 nm", Phys. Med. Biol. 48, 4165-4172.

Ma X, Lu J Q, and Hu X H (2003). "Effect of surface roughness on determination of bulk tissue optical parameters." Optics Letters **28**: 2204-2206.

Maradudin A A, Michel T, McGurn A R, and Mendez E R (1990). "Enhanced backscattering of light from a random grating", Annals of Physics. Vol.203, 255-307.

Marchesini R, Clemente C, Pignoli E and Brambilla M (1992). "Optical properties of in vitro epidermis and their possible relationship with optical properties of in vivo skin", *J. Photochem. Photobiol. B: Biol.* 16, 12-40

Matheson L A and Saunderson J L (1952). "Optical and electrical properties of polystyrene", Styrene: Its Polymers, Copolymers and Derivatives, ed. R H Boundy and R F Boyer (New York: Reinhold) Chapter 2.

Mie G (1908), "Beiträge zur optik trüber medien speziell kolloidaler metallösungen", *Ann Phys.* 25, 377-445

Mourant J R, Boyer J, Hielscher A H, and Bigio I J (1996). "Influence of the scattering phase function on light transport measurements in turbid media performed with small source-detector separations", Opt. Lett. 21(7), 546-548.

Nikolov I D and Ivanov C D (2000). "Optical plastic refractive measurements in the visible and the near-infrared region", Appl. Opt. 39,

Oraevsky A A, Esenaliev R O and Letokhov V S (1991). "Pulse laser ablation of biological tissue: Review of the mechanism, in *Laser ablation, Mechanisms and Applications" (Eds.: Miller J C and Haglund Jr. R F)* (New York: Springer-Verlag) 112-22

Peters V G, Wyman D R, Patterson M S and Frank G L (1990). “Optical properties of normal and diseased human breast tissues in the visible and near infrared”, Phys. Med. Biol. 35, 1317-1334.

Profio A E (1989). Light transport in issue, *App. Opt.* 28, 2216-22

Ronnow D and Veszelei E (1994). ‘Design review of an instrument for spectroscopic total integrated light scattering measurements in the visible wavelength region’, Rev. Sci. Instrum. 65(2), 327-334

Schmitt J M (1999). “Optical Coherent Tomography (OCT): A Review”, IEEE J. of Selected Topics in Quantum Electronics, vol.5, No.4, 1205-1215.

Sharma S K and Banerjee S (2003). “Role of approximate phase functions in Monte Carlo simulation of light propagation in tissues”, J. Opt. A: Pure Appl. Opt. 5, 294-302.

Shvalov A N, Surovtsev I V, Chernyshev A V, Soini J T and Maltsev V P (1999). “Particle classification from light scattering with the flow cytometer”, Cytometry 37, 215-20.

Simpson C R, Kohl M, Essenpreis M and Cope M (1998). Near-infrared optical properties of *ex vivo* human skin and subcutaneous tissues measured using the Monte Carlo inversion technique, *Phys. Med. Biol.* 43, 2465-78

Song Z, Dong K, Hu X H and Lu J Q (1999). “Monte Carlo simulation of converging laser beams propagating in biological materials”, Appl. Opt.38, 2944-9.

Stout K J, Obray C and Jungles J (1985). “Specification and control of surface finish: empiricism versus dogmatism”, Optical Engineering, Vol.24, 414-418

Stuart A and Ord J K (1987). “Kendall’s Advanced Theory of Statistics”, Griffin, London.

Tearney G J, Brezinski M E, Southern J F, Bouma B E, Hee M R and Fujimoto 1995, Determination of the refractive index of highly scattering human tissue by optical coherence tomography, *Opt. Lett*. 21, 2258-60

Toublanc D (1996). “Henyey-Greenstein and Mie phase functions in Monte Carlo radiative transfer computations”, Appl. Opt. 35, 3270-4.

Van Gemert M J C, Jacques S L, Sterenborg H J C and Star W W (1989). IEEE Trans. Biomed. Eng. 36 1146-54.

Van der Zee P, Essenpreis M, and Delpy D T (1993). Proc. SPIE. 1888, 454-465

Visscher M and Struik K G (1994). “Optical profilometry and its application to mechanically inaccessible surfaces part I: principles of focus error detection”, Prec. Engng. 16, 192-8.

Wang Q Z, Liang X, Wang L, Ho P P and Alfano R R 1995, Fourier spatial filter acts as temporal gate for light propagation through a turbid medium, *Opt. Lett*. 20, 1498-500

Wilson B C (1995). “Optical-thermal Response of Laser-Irradiated Tissue”, edited by A. J. Welch and M. J. C. can Gemert, Plenum Press, New York. Chapter 8.

Wilson B C and Adams G 1983, A Monte Carlo model for the absorption and flux distributions of light in tissue, *Med. Phys.* 10, 824-30

Wilson T and Sheppard C 1984, *Theory and Practice of scanning optical microscopy* (London: Academic Press)

Wilson T 1990, *Confocal Microscopy* (London: Academic Press)

Yang P, Gao B C, Wiscombe W, Mishchenko M I, Platnick S, Huang H L, Baum B A, Hu Y X, Winker D, Tsay S C and Park S K (2002). “Inherent and apparent scattering properties of coated or uncoated spheres embedded in an absorbing medium”, Appl. Opt. 41, 2740-59.

Appendix

A.1 Mie Theory For Nonabsorptive and Absorptive Host Medium

When an electromagnetic wave $(\vec{E}, \vec{H})$ propagates in a linear, isotropic, homogeneous medium, it must satisfy the following wave equations:

$$\nabla^2 \vec{E} + k^2 \vec{E} = 0, \tag{A.1}$$

$$\nabla^2 \vec{H} + k^2 \vec{H} = 0, \tag{A.2}$$

derived from the Maxwell's equations for a monochromatic wave:

$$\nabla \cdot \vec{E} = 0, \tag{A.3}$$

$$\nabla \cdot \vec{H} = 0, \tag{A.4}$$

$$\nabla \times \vec{E} = i\omega\mu \vec{H}, \tag{A.5}$$

$$\nabla \times \vec{H} = -i\omega\varepsilon \vec{E}, \tag{A.6}$$

where $k = \omega^2 \varepsilon\mu$ is the wave number, ω is the angular frequency of the wave, ε is the permittivity of the medium, and μ is the permeability of the medium.

Instead of solving the $\vec{E}$ and $\vec{H}$ vectors directly, Mie (1908) proposed to construct to two vector functions by introducing a scalar function ψ in a spherical polar coordinates (r, θ, ϕ):

$$\overrightarrow{M} = \nabla \times (\vec{r}\psi)\,, \tag{A.7}$$

$$\overrightarrow{N} = \frac{\nabla \times \overrightarrow{M}}{k}\,, \tag{A.8}$$

where k is the wave number. We can see that $\overrightarrow{M}$ and $\overrightarrow{N}$ have the properties:

$$\nabla \cdot \overrightarrow{M} = 0\,, \tag{A.9}$$

$$\nabla \cdot \overrightarrow{N} = 0\,, \tag{A.10}$$

$$\nabla \times \overrightarrow{N} = k\overrightarrow{M}\,, \tag{A.11}$$

$$\nabla \times \overrightarrow{M} = k\overrightarrow{N}\,. \tag{A.12}$$

More importantly, if the scalar function ψ is a solution to a scalar wave equation in the spherical polar coordinates, i.e.,

$$\frac{1}{r}\frac{\partial}{\partial r}\left(r^2\frac{\partial\psi}{\partial r}\right) + \frac{1}{r^2\sin\theta}\frac{\partial}{\partial r}\left(\sin\theta\frac{\partial\psi}{\partial\theta}\right) + \frac{1}{r^2\sin\theta}\frac{\partial^2\psi}{\partial\phi^2} + k^2\psi = 0\,, \tag{A.13}$$

then $\overrightarrow{M}$ and $\overrightarrow{N}$ will satisfy the vector wave equations:

$$\nabla^2 \vec{M} + k^2 \vec{M} = 0\,, \tag{A.14}$$

$$\nabla^2 \vec{N} + k^2 \vec{N} = 0\,. \tag{A.15}$$

Therefore, $\vec{M}$ and $\vec{N}$ have all the required properties of an electromagnetic field. And the problem of finding solution to the vector field equations (A.1) and (A.2) reduces to the problem of finding the solutions to the scalar wave equation (A.13), which dramatically decrease the mathematical complexity of the problem.

The linearly independent solutions to Eq. (A.13) are:

$$\psi_{emn} = \cos(m\phi) P_n^m(\cos\theta) z_n(\rho)\,, \tag{A.16}$$

and

$$\psi_{omn} = \sin(m\phi) P_n^m(\cos\theta) z_n(\rho)\,, \tag{A.17}$$

where ρ = koru, the subscripts e and o denote even and odd, $P_n^m(\cos\theta)$ is the associated Legendre function of the first kind and z_n is any of the following four spherical Bessel functions:

$$j_n(\rho) = \sqrt{\tfrac{\pi}{2\rho}} J_{n+1/2}(\rho)\,, \tag{A.18}$$

$$y_n(\rho) = \sqrt{\tfrac{\pi}{2\rho}} Y_{n+1/2}(\rho)\,, \tag{A.19}$$

$$h_n^{(1)}(\rho) = j_n(\rho) + iy_n(\rho), \tag{A.20}$$

$$h_n^{(2)}(\rho) = j_n(\rho) - iy_n(\rho), \tag{A.21}$$

here $J_{n+1/2}(\rho)$ and $Y_{n+1/2}(\rho)$ are the Bessel functions of first and second order. Therefore, the linear independent solutions of $\vec{M}$ and $\vec{N}$ expressed by ψ_{emn} and ψ_{omn} are

$$\vec{M}_{emn} = \nabla \times (\vec{r}\psi_{emn}), \tag{A.22}$$

$$\vec{M}_{omn} = \nabla \times (\vec{r}\psi_{omn}), \tag{A.23}$$

$$\vec{N}_{emn} = \frac{\nabla \times \vec{M}_{emn}}{k}, \tag{A.24}$$

$$\vec{N}_{omn} = \frac{\nabla \times \vec{M}_{omn}}{k}, \tag{A.25}$$

which can be written in component form as:

$$\vec{M}_{emn} = \frac{-m}{\sin\theta}\sin(m\phi)P_n^m(\cos\theta)z_n(\rho)\hat{e}_\theta - \cos(m\phi)\frac{dP_n^m(\cos\theta)}{d\theta}z_n(\rho)\hat{e}_\phi, \tag{A.26}$$

$$\vec{M}_{omn} = \frac{m}{\sin\theta}\cos(m\phi)P_n^m(\cos\theta)z_n(\rho)\hat{e}_\theta - \sin(m\phi)\frac{dP_n^m(\cos\theta)}{d\theta}z_n(\rho)\hat{e}_\phi, \tag{A.27}$$

$$\vec{N}_{emn} = \frac{z_n(\rho)}{\rho}\cos(m\phi)\,n(n+1)\,P_n^m(\cos\theta)\,\hat{e}_r$$
$$+\cos(m\phi)\frac{dP_n^m(\cos\theta)}{d\theta}\frac{1}{\rho}\frac{d}{d\rho}\left[\rho z_n(\rho)\right]\hat{e}_\theta \;, \tag{A.28}$$
$$-m\sin(m\phi)\frac{P_n^m(\cos\theta)}{\sin\theta}\frac{1}{\rho}\frac{d}{d\rho}\left[\rho z_n(\rho)\right]\hat{e}_\phi$$

$$\vec{N}_{omn} = \frac{z_n(\rho)}{\rho}\sin(m\phi)\,n(n+1)\,P_n^m(\cos\theta)\,\hat{e}_r$$
$$+\sin(m\phi)\frac{dP_n^m(\cos\theta)}{d\theta}\frac{1}{\rho}\frac{d}{d\rho}\left[\rho z_n(\rho)\right]\hat{e}_\theta \,. \tag{A.29}$$
$$+m\cos m\phi\frac{P_n^m(\cos\theta)}{\sin\theta}\frac{1}{\rho}\frac{d}{d\rho}\left[\rho z_n(\rho)\right]\hat{e}_\phi$$

Because of the completeness of the functions $\vec{M}_{emn}$, $\vec{M}_{omn}$, $\vec{N}_{emn}$, $\vec{N}_{omn}$, any electromagnetic fields can be expanded in an infinite series of these functions.

Now consider a homogeneous spherical particle with radius of R_a embedded in a medium that is illuminated by a plane wave with x-polarization propagating along z (Fig.A.1):

$$\vec{E}_i = E_0 e^{ikr\cos\theta}\hat{e}_x \,, \tag{A.30}$$

where

$$\vec{e}_x = \sin\theta\cos\phi\hat{e}_r + \cos\theta\cos\phi\hat{e}_\theta - \sin\phi\hat{e}_\phi \,. \tag{A.31}$$

For the incident wave, its field can be expanded as

$$\vec{E}_i = E_0 \sum_{n=1}^{\infty} i^n \frac{2n+1}{n(n+1)} \left(\vec{M}_{o1n}^{(1)} - i\vec{N}_{e1n}^{(1)} \right), \tag{A.32}$$

$$\vec{H}_i = \frac{-k}{\omega\mu} E_0 \sum_{n=1}^{\infty} i^n \frac{2n+1}{n(n+1)} \left(\vec{M}_{e1n}^{(1)} + i\vec{N}_{o1n}^{(1)} \right), \tag{A.33}$$

where μ is the permeability of the surrounding medium, the superscript (1) appended to the vector spherical harmonics here is used to indicate that the radial dependence of the generating function is specified by j_n according to the requirement that the incident field is finite at origin.

Correspondingly, the field inside the spherical particle $\left(\vec{E}_1, \vec{H}_1\right)$ is expanded as

$$\vec{E}_1 = \sum_{n=1}^{\infty} E_n \left(c_n \vec{M}_{o1n}^{(1)} - id_n \vec{N}_{e1n}^{(1)} \right), \tag{A.34}$$

$$\vec{H}_1 = \frac{-k}{\omega\mu_1} \sum_{n=1}^{\infty} E_n \left(d_n \vec{M}_{e1n}^{(1)} + ic_n \vec{N}_{o1n}^{(1)} \right), \tag{A.35}$$

where μ_1 is the permeability of the sphere. According to the asymptotical behaviors of the spherical Bessel functions, the scattered field $\left(\vec{E}_s, \vec{H}_s\right)$ can be expanded as

$$\vec{E}_s = \sum_{n=1}^{\infty} E_n \left(ia_n \vec{N}_{e1n}^{(3)} - b_n \vec{M}_{o1n}^{(3)} \right), \tag{A.36}$$

$$\vec{H}_s = \frac{k}{\omega\mu} \sum_{n=1}^{\infty} E_n \left(ib_n \vec{N}_{o1n}^{(3)} + a_n \vec{M}_{e1n}^{(3)} \right), \tag{A.37}$$

where $E_n = i^n E_0 \left(2n+1\right)/n\left(n+1\right)$, the superscript (3) appended to vector spherical harmonics is used to indicate that the radial dependence of the generating function is specified by $h_n^{(1)}$.

At the boundary between the sphere and the surrounding medium(r = R_a), we have conditions:

$$E_{i\theta} + E_{s\theta} = E_{1\theta}, \tag{A.38}$$

$$E_{i\phi} + E_{s\phi} = E_{1\phi}, \tag{A.39}$$

$$H_{i\theta} + H_{s\theta} = H_{1\theta}, \tag{A.40}$$

$$H_{i\phi} + H_{s\phi} = H_{1\phi}. \tag{A.41}$$

From Eqs. (A.32), (A.33), (A.34), (A.35), (A.36), and (A.37), we could obtain the scattering coefficients:

$$a_n = \frac{\mu m^2 j_n\left(mx\right)\left[xj_n\left(x\right)\right]' - \mu_1 j_n\left(x\right)\left[mxj_n\left(mx\right)\right]'}{\mu m^2 j_n\left(mx\right)\left[xh_n^{(1)}\left(x\right)\right]' - \mu_1 h_n^{(1)}\left(x\right)\left[mxj_n\left(mx\right)\right]'}, \tag{A.42}$$

$$b_n = \frac{\mu_1 j_n\left(mx\right)\left[xj_n\left(x\right)\right]' - \mu j_n\left(x\right)\left[mxj_n\left(mx\right)\right]'}{\mu_1 j_n\left(mx\right)\left[xh_n^{(1)}\left(x\right)\right]' - \mu h_n^{(1)}\left(x\right)\left[mxj_n\left(mx\right)\right]'}, \tag{A.43}$$

and the coefficients of the field inside the particle:

$$c_n = \frac{\mu_1 j_n(mx)\left[xh_n^{(1)}(x)\right]' - \mu_1 h_n^{(1)}(x)\left[xj_n(x)\right]'}{\mu_1 j_n(mx)\left[xh_n^{(1)}(x)\right]' - \mu h_n^{(1)}(x)\left[mxj_n(mx)\right]'} \quad , \tag{A.44}$$

$$d_n = \frac{\mu_1 m j_n(x)\left[xh_n^{(1)}(x)\right]' - \mu_1 m h_n^{(1)}(x)\left[xj_n(x)\right]'}{\mu m^2 j_n(mx)\left[xh_n^{(1)}(x)\right]' - \mu_1 h_n^{(1)}(x)\left[mxj_n(mx)\right]'}, \tag{A.45}$$

where the prime indicates differentiation with respect to the argument in the parentheses, the size parameter $x = kR_a = \frac{2\pi N R_a}{\lambda}$, the relative refractive index $m = \frac{k_1}{k} = \frac{N_1}{N}$, N_1 and N are the refractive indices of particle and medium, respectively.

By introducing the Riccati-Bessel functions:

$$\psi_n(\rho) = \rho j_n(\rho), \tag{A.46}$$

$$\xi_n(\rho) = \rho h_n^{(1)}(\rho), \tag{A.47}$$

the scattering coefficients (A.42) and (A.43) can expressed as

$$a_n = \frac{m\psi_n(mx)\psi_n'(x) - \psi_n(x)\psi_n'(mx)}{m\psi_n(mx)\xi_n'(x) - \xi_n(x)\psi_n'(mx)}, \tag{A.48}$$

$$b_n = \frac{\psi_n(mx)\psi_n'(x) - m\psi_n(x)\psi_n'(mx)}{\psi_n(mx)\xi_n'(x) - m\xi_n(x)\psi_n'(mx)}, \tag{A.49}$$

where the permeability of the particle μ_1 and the surrounding medium μ are taken to be the same and this is approximately true for all the nonmagnetic media.

A.1.1 The Mie Theory for a Nonabsorptive Host Medium

When the host medium is nonabsorptive to the incident light, it was pointed out [Bohren and Huffman 1983] that the energy absorbed by the particle is given by

$$W_{abs} = -\int_A \vec{S} \cdot \hat{e}_r dA \,, \tag{A.50}$$

where A represents a closed surface surrounding the particle, $\hat{e}_r$ is unit vector along the radial direction in spherical polar coordinates, and $\vec{S}$ is the time-averaged Poynting vector defined as

$$\vec{S} = \frac{1}{2}\mathrm{Re}\left\{\vec{E} \times \vec{H}^*\right\}. \tag{A.51}$$

In the medium outside the sphere, the electromagnetic field $\left(\vec{E}, \vec{H}\right)$ is the superposition of the incident wave $\left(\vec{E}_i, \vec{H}_i\right)$ and the scattered wave $\left(\vec{E}_s, \vec{H}_s\right)$:

$$\vec{E} = \vec{E}_i + \vec{E}_s \,, \tag{A.52}$$

$$\vec{H} = \vec{H}_i + \vec{H}_s \,. \tag{A.53}$$

Therefore, the time-averaged Poynting vector $\vec{S}$ can be presented as the sum of three terms:

$$\vec{S} = \frac{1}{2}\mathrm{Re}\left\{\vec{E}\times\vec{H}^*\right\} = \vec{S}_i + \vec{S}_s + \vec{S}_{ext} \tag{A.54}$$

where $\vec{S}_i = \frac{1}{2}\mathrm{Re}\left\{\vec{E}_i\times\vec{H}_i^*\right\}$, $\vec{S}_s = \frac{1}{2}\mathrm{Re}\left\{\vec{E}_s\times\vec{H}_s^*\right\}$ and $\vec{S}_{ext} = \frac{1}{2}\mathrm{Re}\left\{\vec{E}_i\times\vec{H}_s^* + \vec{E}_s\times\vec{H}_i^*\right\}$.

The energy scattered by the sphere, W_{sca} can be defined as

$$W_{sca} = \int_A \vec{S}_s\cdot\hat{e}_r\, dA\,, \tag{A.55}$$

and the total energy removed or extinguished from the incident wave, W_{ext} can be expressed as

$$W_{ext} = -\int_A \vec{S}_{ext}\cdot\hat{e}_r\, dA\,. \tag{A.56}$$

We can find that, from Eqs. (A.50), (A.55), and (A.56),

$$W_{ext} = W_{abs} + W_{sca}\,. \tag{A.57}$$

Therefore, the interaction of a plane wave with a spherical particle can be characterized by the extinction cross section C_{ext}, the scattering cross section C_{sca}, and the absorption cross section as C_{abs} and they are defined respectively as

$$C_{ext} = \frac{W_{ext}}{I_i}, \tag{A.58}$$

$$C_{sca} = \frac{W_{sca}}{I_i}, \tag{A.59}$$

$$C_{abs} = \frac{W_{abs}}{I_i}, \tag{A.60}$$

where $I_i = \frac{1}{2}\frac{k}{\omega\mu}\left|E_i\right|^2$ is the incident wave intensity. And we have

$$C_{ext} = C_{abs} + C_{sca}. \tag{A.61}$$

W_{ext} and W_{sca} can written in the component form as

$$W_{ext} = \frac{1}{2}\mathrm{Re}\int_0^{2\pi}\int_0^{\pi}\left(E_{i\phi}H_{s\theta}^* - E_{i\theta}H_{s\phi}^* - E_{s\theta}H_{i\phi}^* + E_{s\phi}H_{i\theta}^*\right)r^2 \sin\theta d\theta d\phi, \tag{A.62}$$

$$W_{sca} = \frac{1}{2}\mathrm{Re}\int_0^{2\pi}\int_0^{\pi}\left(E_{s\theta}H_{s\phi}^* - E_{s\phi}H_{s\theta}^*\right)r^2 \sin\theta d\theta d\phi \tag{A.63}$$

where the radius $r \geq R_a$ of the imaginary sphere is arbitrary.

Consider the case that the incident light is x-polarized. From Eq. (A.32) and (A.33), the incident field can be written in the component form as

$$E_{i\theta} = \frac{\cos\phi}{\rho}\sum_{n=1}^{\infty} E_n\left(\psi_n \pi_n - i\psi_n^{'}\tau_n\right), \tag{A.64}$$

$$E_{i\phi} = \frac{\sin\phi}{\rho}\sum_{n=1}^{\infty} E_n\left(\psi'_n\pi_n - \psi_n\tau_n\right), \tag{A.65}$$

$$H_{i\theta} = \frac{k}{\omega\mu}\tan\phi E_{i\theta}\,, \tag{A.66}$$

$$H_{i\phi} = \frac{-k}{\omega\mu}\operatorname{cotan}\phi E_{i\phi}\,. \tag{A.67}$$

where functions π_n and τ_n are defined as

$$\pi_n = \frac{P_n^1\left(\cos\theta\right)}{\sin\theta}\,, \tag{A.68}$$

$$\tau_n = \frac{dP_n^1\left(\cos\theta\right)}{d\theta}\,. \tag{A.69}$$

The corresponding scattered field is

$$E_{s\theta} = \frac{\cos\phi}{\rho}\sum_{n=1}^{\infty} E_n\left(ia_n\xi'_n\tau_n - b_n\xi_n\pi_n\right), \tag{A.70}$$

$$E_{s\theta} = \frac{\sin\phi}{\rho}\sum_{n=1}^{\infty} E_n\left(b_n\xi_n\tau_n - ia_n\xi'_n\pi_n\right), \tag{A.71}$$

$$H_{s\theta} = \frac{k}{\omega\mu}\frac{\sin\phi}{\rho}\sum_{n=1}^{\infty} E_n\left(ib_n\xi'_n\tau_n - a_n\xi_n\pi_n\right), \tag{A.72}$$

$$H_{s\theta} = \frac{k}{\omega\mu}\frac{\cos\phi}{\rho}\sum_{n=1}^{\infty} E_n \left(ib_n \xi_n^{'} \pi_n - a_n \xi_n \tau_n \right). \tag{A.73}$$

By Substituting Eqs. (A.70), (A.71), (A.72) and (A.73) into Eq. (A.62), we can obtain the energy scattered by the sphere

$$W_{sca} = \frac{\pi |E_0|^2}{k\omega\mu}\sum_{n=1}^{\infty}(2n+1)\left(|a_n|^2 + |b_n|^2\right). \tag{A.74}$$

From Eq. (A.73), the scattering cross section can be deduced as

$$C_{sca} = \frac{W_s}{I_i} = \frac{2\pi}{k^2}\sum_{n=1}^{\infty}(2n+1)\left(|a_n|^2 + |b_n|^2\right). \tag{A.75}$$

Likewise, the extinction cross section is

$$C_{ext} = \frac{W_{ext}}{I_i} = \frac{2\pi}{k^2}\sum_{n=1}^{\infty}(2n+1)\,\mathrm{Re}\left\{a_n + b_n\right\}. \tag{A.76}$$

The scattering amplitude matrix for a plane wave scattered by a sphere has been found to have the form:

$$\begin{pmatrix} E_{\|s} \\ E_{\perp s} \end{pmatrix} = \frac{e^{ik(r-z)}}{-ikr}\begin{pmatrix} S_1 & 0 \\ 0 & S_2 \end{pmatrix}\begin{pmatrix} E_{\|i} \\ E_{\perp i} \end{pmatrix}, \tag{A.77}$$

where

$$S_1 = \sum_n \frac{2n+1}{n(n+1)}(a_n\pi_n + b_n\tau_n), \tag{A.78}$$

$$S_2 = \sum_n \frac{2n+1}{n(n+1)}(a_n\tau_n + b_n\pi_n), \tag{A.79}$$

and $(E_{\|i}, E_{\perp i})$ and $(E_{\|s}, E_{\perp s})$ are the incident and scattered wave components parallel and perpendicular to the scattering plane, which is defined by the scattering direction $\hat{e}_r$ and $\hat{e}_z$.

For an unpolarized incident wave, the scattering phase becomes

$$p(\theta) = \frac{1}{2}\left(|S_1|^2 + |S_2|^2\right). \tag{A.80}$$

And the anisotropy factor g is then given by

$$\begin{aligned} g &= \langle \cos\theta \rangle \\ &= \frac{4\pi R_a^2}{x^2 C_{sca}}\left[\sum_n \frac{n(n+2)}{n+1}\mathrm{Re}\left\{a_n a_{n+1}^* + b_n b_{n+1}^*\right\} + \sum_n \frac{2n+1}{n(n+1)}\mathrm{Re}\left\{a_n b_n^*\right\}\right]. \end{aligned} \tag{A.81}$$

A.1.2 The Mie Theory for an Absorptive Host Medium

When the medium within which the sphere is immersed is nonabsorptive to the incident wave, the effect of the host medium is simply to reduce the complex refractive index of the spherical particle by a factor of the refractive index of the medium. The scattering properties such as the scattering cross section C_{sca}, the absorption cross section

C_{abs}, and the extinction cross section C_{ext} calculated at the sphere's surface (i.e., the near field) are identical to that calculated in the radiation zone (i.e., the far field).

However, when the host medium is absorptive to the incident wave, the effect of the host medium absorption on the prediction of light scattering by the spherical particle requires thorough consideration. Different types of C_{sca} have been employed and discussed in previous studies [Chylek 1997, Fu and Sun 2001, Yang et al 2002]. An inherent scattering cross-section can be defined in the near-field, i.e., at the sphere's surface, of the scattered light while an apparent scattering cross-section can be derived from the asymptotic form of the scattered light fields in the far-field or the radiation zone where light measurements are carried out. As Yang et al [2002] have pointed out, the scattered wave when leave the particle and travel within the absorbing medium will suffer not only attenuation in magnitude but also modulation of the wave modes when reaching the radiation zone. The form of the scattering cross section used to determine the scattering properties in the far field needs careful examination. The inherent scattering cross section, will couple the medium's absorption in an inseparable way in the radiation zone that it can't correctly predict the experimental observations in the far field. The apparent scattering cross section, which is calculated from the asymptotic form of the scattering waves in the far field, will be the proper definition of the scattering cross section for the radiation transfer calculations. On the other hand, the inherent absorption cross-section is assumed identical to its apparent part, which is defined in the same way as the scattering cross section.

For a plane incident wave with a x-polarization propagating in the z direction within an absorptive medium of the complex refractive index N_0

$$N_0 = N_{0r} + iN_{0i}\,, \tag{A.82}$$

the inherent scattering cross section C_{sca} and extenuation cross section C_{sca} can be calculated from Eqs. (A.75) and (A.76), respectively. While the inherent absorption cross section is given by

$$C_{abs} = C_{ext} - C_{sca}\,. \tag{A.83}$$

However, the apparent scattering cross section $C_{sca}^{'}$ is given by

$$C_{sca}^{'} = \frac{2\pi \exp\left(-2N_{0i}k_0R_a\right)}{\left|N_0\right|^2 k_0^2} \sum_{n=1}^{\infty} \left(2n+1\right)\left(\left|a_n\right|^2 + \left|b_n\right|^2\right) \tag{A.84}$$

where $k_0 = 2\pi/\lambda$ in which λ is the wavelength of the incident wave in vacuum and R_a is the radius of the spherical particle.

Therefore, for spherical particles system of particle number concentration C_0 within an absorptive medium, in the far field, the absorption coefficient μ_a is given by

$$\mu_a = C_0 \times C_{abs} + \frac{4\pi N_{0i}}{\lambda}\,. \tag{A.85}$$

The scattering coefficient μ_s is given by, as suggested by Yang et al [2002],

$$\mu_s = C_0 \times C'_{sca} \times \exp\left(2N_{0,i}k_0R_a\right). \tag{A.86}$$

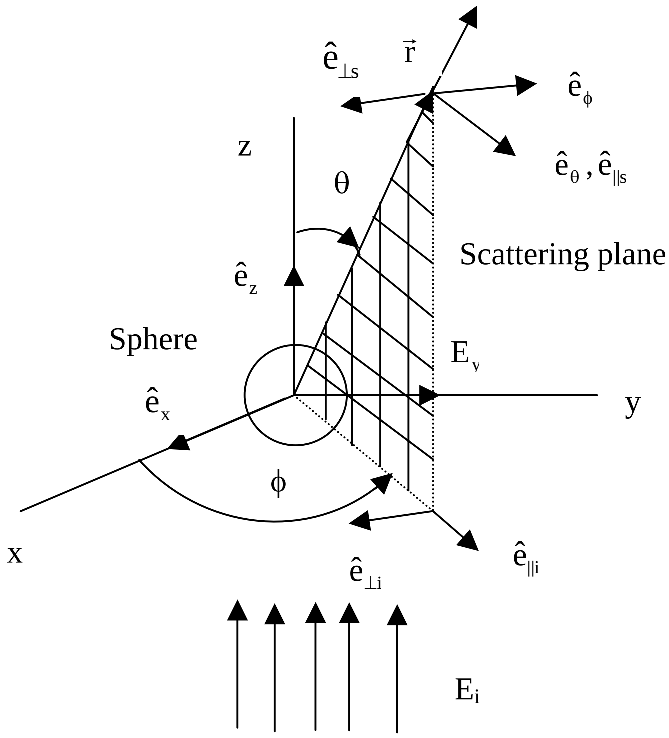

Figure A.1 Light scattering by a sphere.

A.2 Flow Chart of Monte Carlo Based Photon Tracking

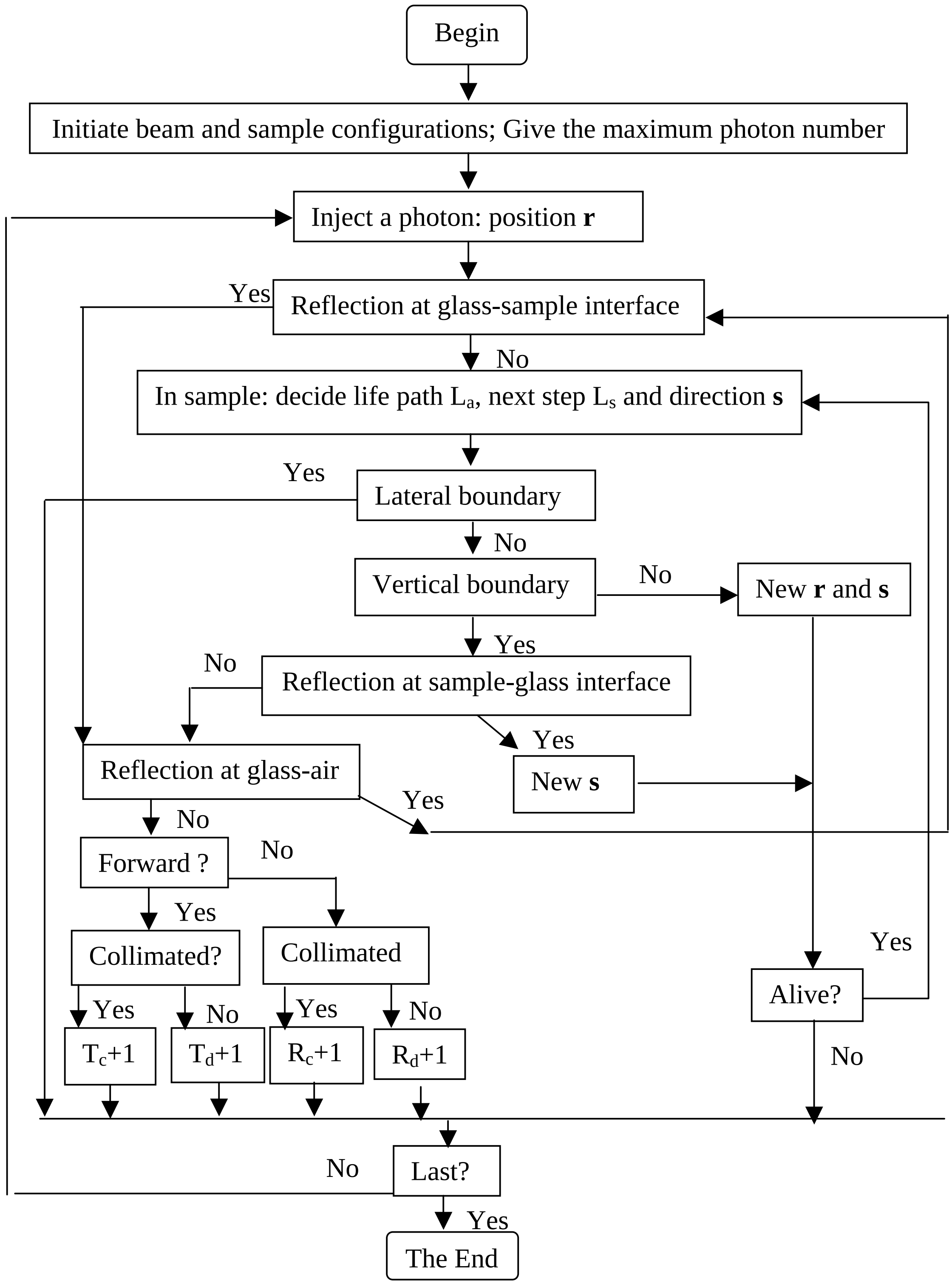

A.3 Flow Chart of Monte Carlo Based Automatic Determination of μ_s, μ_a, and g from R_d and T_d

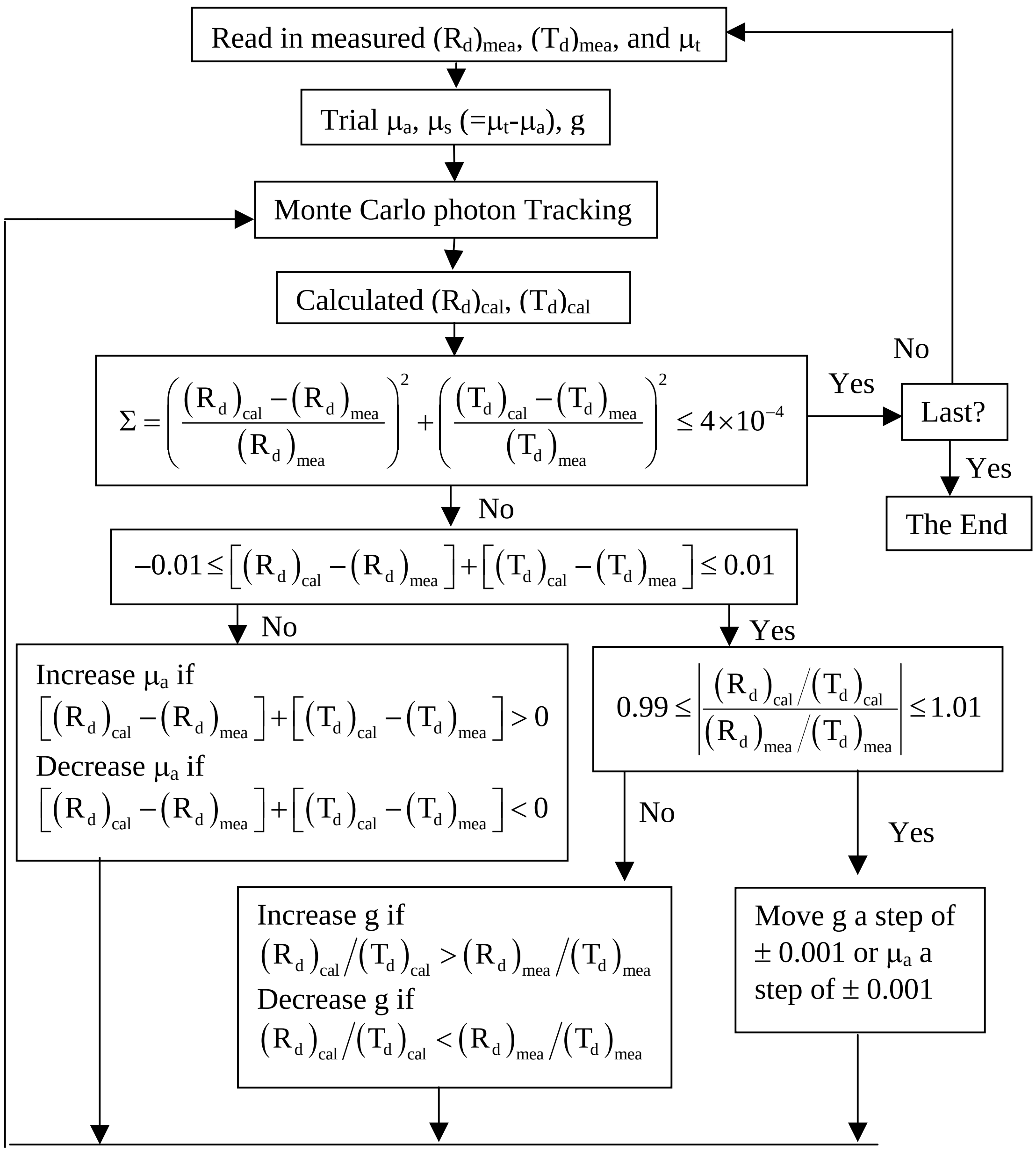

A.4 Flow Chart of Monte Carlo Based Determination of Complex Refractive Index of Microsphere Suspensions

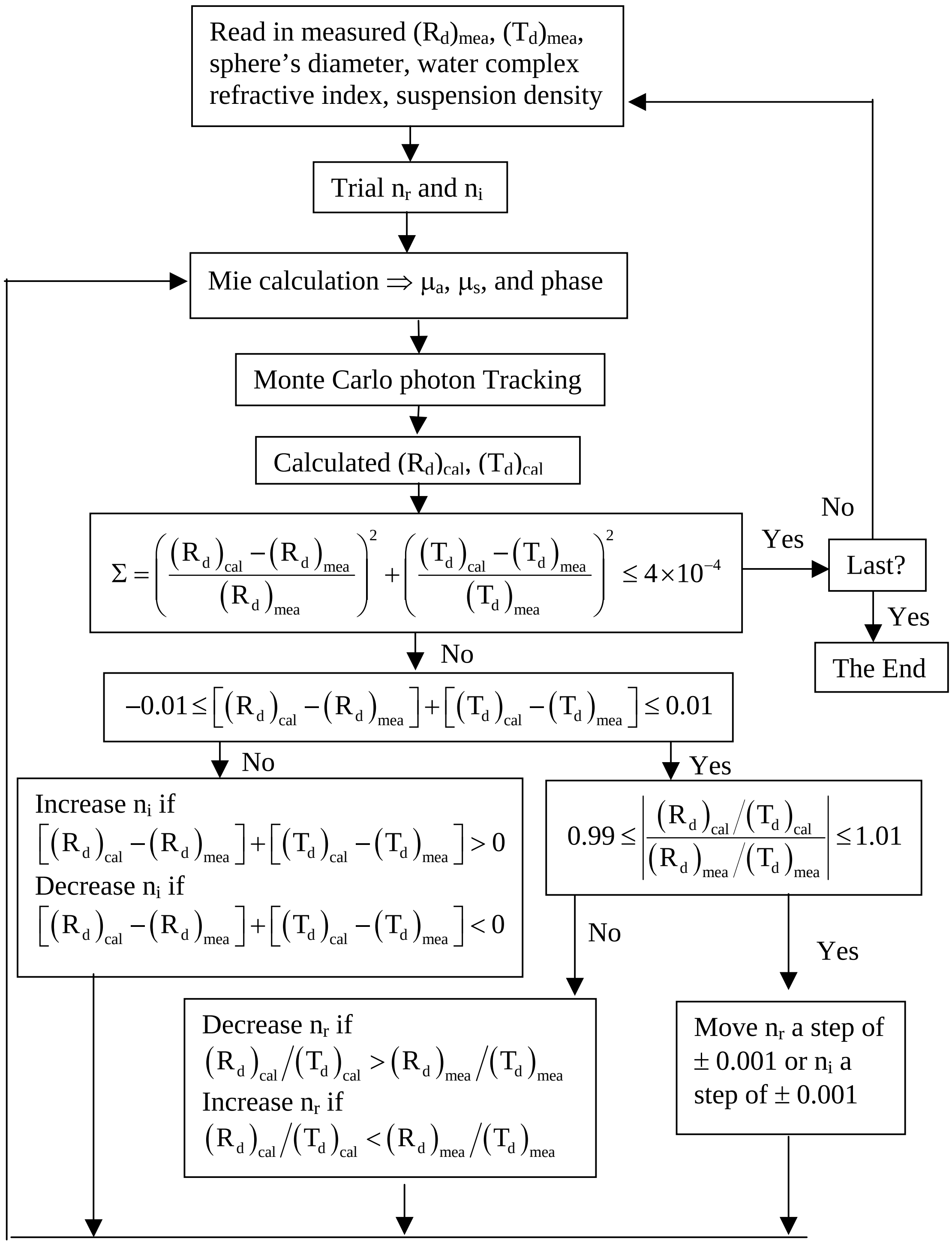

A.5 Flow Chart of Monte Carlo Based Manual Determination of μ_s, μ_a, and g under rough surfaces from R_d, T_d, and T_c

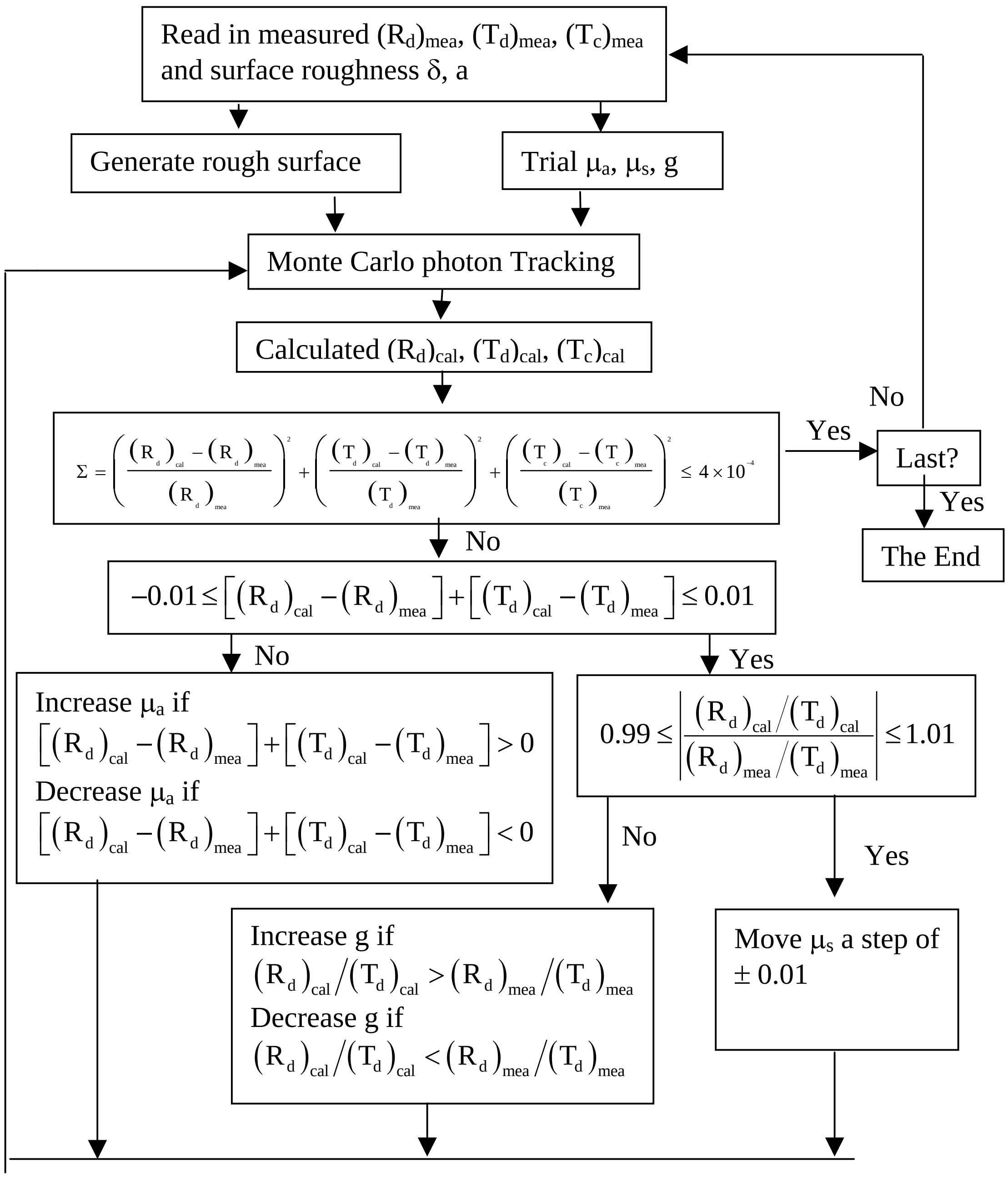

A.6 QB Code for Data Acquisition of Confocal Imaging

```
' program name: confocal.bas
' (i) reading data from lock-in via GPIB488 board
' (ii) Control a stepping motor and PZT with data acquisition at stops
using
'       DAS1600 (J2) board

'last modification by Ma: Dec 15, 2003

'$INCLUDE: 'QB4DECL.BI'
'$INCLUDE: 'DASDECL.BI'
'$INCLUDE: 'DAS1600.BI'       'library file for DAS1600 card
'$INCLUDE: 'IEEEQB.BI'        'library file for CEC488 card

      DEFINT H-Z
      DECLARE SUB initlz (er%, Delaytime!, st1$)
      DECLARE SUB moving (dr$, stpsz!)
      DECLARE SUB saving (startime$, stoptime$, st1$, totalsecond, J1%)
      DECLARE SUB GRAPHICSINITIALIZE (XMIN%, xmax%, Ymin%, Ymax%,
XLABEL$, YLABEL$)
      DECLARE SUB dproc (ADT%)
      DECLARE SUB selemenu (ha%)
      DECLARE SUB procpara (st1$, Ymin%, Ymax%)
      DECLARE SUB adpara (d%)
      DECLARE SUB motorctrl (dir%, stnumber%, trnumber%, J1%, de1$)
      DECLARE SUB delay (d1%)
      DECLARE SUB checksensitivity (vol!, phase!, fullvol!, sen%, sta%)
      DECLARE SUB snapdata (stepsequence%, vol!, phase!, Delaytime!)
      DECLARE SUB moveinch (StepSize%, Direction$)
      DECLARE SUB movestep (Axis$, StepSize%, Direction$)
      DECLARE SUB toggleDirection (Direction$)

      DECLARE SUB BitRead (ADReadIn%, ADReadOut%)

      datasize% = 10500
      DIM SHARED AdData(datasize%) AS SINGLE        ' data array
      DIM SHARED otherdata(datasize%) AS SINGLE        ' experimental
parameter
      DIM SHARED DataBuf(500) AS INTEGER         ' A/D sample buffer
      DIM SHARED CHANGAINARRAY(50) AS INTEGER    ' Chan/Gain array

      DIM SHARED nBoards AS INTEGER
      DIM SHARED nDasErr AS INTEGER              ' Error flag
      DIM SHARED szCfgName AS STRING             ' File name string
      DIM SHARED hDev AS LONG                    ' Device Handle
      DIM SHARED hAD AS LONG                     ' A/D Frame Handle
      DIM SHARED conumber AS INTEGER             ' # of total data
      DIM SHARED dsamplenumber AS INTEGER        ' dsample=# of A/D
sample per data
      DIM SHARED dsampletime AS INTEGER          ' # of (0.1us) between
A/D samples
```

```
      DIM SHARED ADgaincode AS INTEGER           ' A/D gain code
      DIM SHARED ADgain AS INTEGER               ' A/D actual gain
      DIM SHARED dactime AS SINGLE               ' time between data
acquisition
      DIM SHARED svpointer AS INTEGER           ' save pointer

'default values
      dsamplenumber = 20             'default # of samples per A/D
reading
      dsampletime = 5000             '0.5 ms between samples
      ADgaincode = 0
      ADgain = 1                     'gain=1
      conumber = 500
      datasav% = 0
      datacq% = 0
      Ymin% = 0
      Ymax% = 4096
      dactime = 1                    '1 sec between two data
acquisition
      runnumber% = 0

      CLS : LOCATE 5, 1

'initilization of board with default values

      CALL initlz(er%, Delaytime!, st1$)

      PRINT : PRINT
      PRINT "This program read signal from either CH0 of the DAS1600
board "
      PRINT "or the lock-in amplifer via GPIB 488 board."
      PRINT "The samples will be averaged to obtain data as a funtion
of time."
      PRINT "The data will be plotted on screen as a function of time."
      PRINT "The voltage range: 0.00 -- 10.00 (V)"
      PRINT
      PRINT "hit any key to continue. "
      DO WHILE INKEY$ = "": LOOP

'print menu

60      CALL selemenu(ha)

70      CLS : LOCATE 10, 1
      SELECT CASE ha
      CASE 1
            GOTO 100
      CASE 2
            GOTO 200
      CASE 3
            GOTO 300
      CASE 4
            GOTO 400
```

```
      CASE 5
            GOTO 500
      CASE 6
            GOTO 600
      CASE 7
            IF svpointer < 300 THEN
            PRINT "there is nothing to save, hit any key to main menu.
"
            DO WHILE INKEY$ = "": LOOP
            ELSE
            datasav% = datasav% + 1
            IF svpointer = 300 THEN K1% = J0%       'using parameters
for mode 3
            IF svpointer = 400 THEN K1% = J1%       'using parameters
for mode 4&5
            IF svpointer = 600 THEN K1% = stepsequence%    'using
parameters for mode 6
            CALL saving(startime$, stoptime$, st1$, totalsecond, K1%)
            END IF
            GOTO 60
      CASE 8
            GOTO 1000
      CASE ELSE
            GOTO 60
END SELECT

100     CALL procpara(st1$, Ymin%, Ymax%)    'change processing
parameters
      GOTO 60

200     CALL adpara(d%)         'change A/D board parameters (DAS1601)
      GOTO 60

'start of single-shot data acquisition loop
300     svpointer = 300           'pointer for saving data
      datacq% = datacq% + 1
      CLS
      PRINT "single-shot data acquisition: hit any key when ready for
next reading"
      PRINT "Press S key to stop the reading loop, press R key to redo
last entry."
      PRINT "total number of reading = "; conumber
      PRINT
      PRINT "hit any key to proceed >> "
      DO WHILE INKEY$ = "": LOOP

      CLS
      PRINT "sequnce"; SPACE$(10); "voltage reading (V)"; SPACE$(10),
"parameter"

      FOR J0% = 0 TO conumber - 1
      INPUT "enter an integer parameter, or S for stop, or R for redo
last entry): ", ik$
      IF UCASE$(ik$) = "S" THEN
```

```
      BEEP: LOCATE 23, 10
      INPUT "STOP detected, enter: 1--continue, 2--main menu >> ", cc1%
      J0% = J0% - 1
            IF cc1% = 2 THEN GOTO 60 ELSE GOTO 380
      ELSEIF UCASE$(ik$) = "R" THEN
      J0% = J0% - 2: GOTO 380
      ELSE
      otherdata(J0%) = VAL(ik$)
      END IF

      CALL dproc(ADT%)
      AdData(J0%) = ADT%

'be careful of overflow
      ADvol! = (ADT% / 4096 / ADgain) * 10    'converting into volt
      PRINT J0% + 1; SPACE$(10); ADvol!; SPACE$(10); otherdata(J0%)

380     NEXT J0%

      BEEP
      LOCATE 24, 10
      PRINT "Data qcquissition is done.  Hit any key to main menu. "
      DO WHILE INKEY$ = "": LOOP
      GOTO 60
'end of single-shot data acquisition loop

'start of continuous data acquisition loop
400     svpointer = 400
      XMIN = 0:               xmax = conumber
      XLABEL$ = "time":       YLABEL$ = "data"
      datacq% = datacq% + 1

      SCREEN 0: CLS
      CALL GRAPHICSINITIALIZE(XMIN, xmax, Ymin%, Ymax%, XLABEL$,
YLABEL$)
      LOCATE 3, 1: PRINT "S to stop"
      LOCATE 4, 1: PRINT "start time"
      LOCATE 5, 1: PRINT TIME$
      LOCATE 8, 1: PRINT "A/D gain"
      LOCATE 9, 1: PRINT ADgain
      LOCATE 10, 1: PRINT "total data"
      LOCATE 11, 1: PRINT "="; conumber
      LOCATE 13, 1: PRINT "data"

      startime$ = TIME$
      beginsecond = TIMER

      FOR J1% = 0 TO conumber - 1

      dacbegin = TIMER                'start timing

      CALL dproc(ADT%)                'A/D with dsamplenumber averages
      AdData(J1%) = ADT%
```

```
      PSET (J1%, ADT%)                                'draw on screen

      LOCATE 22, 1: PRINT SPACE$(79): LOCATE 22, 1
      ADvol! = (ADT% / 4096 / ADgain) * 10           'converting into
volt
      PRINT "current (V) = "; ADvol!               'be careful of
overflow
      IF J1% > 0 THEN
      LADvol! = (AdData(J1% - 1) / 4096 / ADgain) * 10
      LOCATE 22, 40
      PRINT "last (V) ="; LADvol!;
      END IF

450     IF (TIMER - dacbegin) < dactime THEN
            LOCATE 14, 1: PRINT J1%; " th"
            IF UCASE$(INKEY$) = "S" THEN
            BEEP: LOCATE 23, 10
            stoptime$ = TIME$
            totalsecond = TIMER - beginsecond
            INPUT "stop detected, enter: 1--continue, 2--main menu >>
", cc1%
                  IF cc1% = 2 THEN
                  GOTO 60
                  ELSE
                  LOCATE 23, 1: PRINT SPACE$(80)
                  GOTO 450
                  END IF
            END IF
            GOTO 450
      END IF

      NEXT J1%

      stoptime$ = TIME$
      totalsecond = TIMER - beginsecond

      BEEP
      LOCATE 6, 1: PRINT "stop time"
      LOCATE 7, 1: PRINT TIME$
      LOCATE 23, 10
      PRINT "Data qcquissition is done within"; totalsecond / 60;
"munites, ";
      PRINT "hit any key to main menu. "
      DO WHILE INKEY$ = "": LOOP
      GOTO 60
'end of continuous data acquisition loop

'start of one stepping motor control loop
500     CLS : svpointer = 400: datacq% = datacq% + 1
'assuming 1000step/turn for stepping motor and 2mm/turn for translator
      stpsz! = 2: PRINT "stepsize = 2 um"

      PRINT "choose: "
      PRINT " 1 ---- continuous driving "
```

```
      PRINT " 2 ---- stepping and data acquisition "
      INPUT "enter a number: ", ch10%
'        INPUT "enter motor direction (Forward / Reverse): ", dr$
      dr$ = "F"            'take this one out if the above one is used
      IF ch10% = 1 THEN
      CALL moving(dr$, stpsz!)
      GOTO 60
      END IF

520     INPUT "enter the number of steps per move: ", stnumber%
      IF stnumber% < 1 THEN GOTO 520
      PRINT "distance per move = "; stnumber% * stpsz!; "um"
540     INPUT "enter travel range of the motor in mm: ", trvl!
      trnumber% = trvl! / (.001 * stpsz! * stnumber%)
      IF trnumber% > 5000 THEN
      BEEP: PRINT "too many moves needed, please redo."
      GOTO 540
      ELSEIF trnumber% < 1 THEN
      BEEP: PRINT "error inputs , please redo"
      GOTO 540
      END IF
      INPUT "delay between moves (Y/N) ? ", de1$
      st1$ = "stepsize=" + STR$(stpsz! * stnumber%) + "um"
      startime$ = TIME$
      IF UCASE$(dr$) = "F" THEN dir% = 0 ELSE dir% = 1
      CALL motorctrl(dir%, stnumber%, trnumber%, J1%, de1$)
      stoptime$ = TIME$
      GOTO 60
'end of one stepping motor control loop

'start of x-z scan loop (stepping motor for x and PZT for z)
' set the step size of the motor

600    st1$ = ""
      svpointer = 600
      runnumber% = runnumber% + 1
      IF runnumber% > 1 THEN GOTO 620

'*****        motor X: 400 steps per revolution
'*****     micrometer: 500 micron per revolution
'*****           gear: 13/105

      XMotorStepSize! = 13! / 84!    '13/84um per step for motor X

'    XMotorStepSize% = 25    '2.5um per step for motor X (horizontal)
'    YMotorStepSize% = 25    '2.5um per step for motor Y (vertical)

      CLS : LOCATE 2, 1

      PRINT "In this mode, a stepping motor and a PZT will be
controlled to scan ";
      PRINT "in the horizontal direction(by stepping moyor) and in the
vertical ";
```

```
      PRINT "direction(by PZT). PZT will go up(Y) numbers of steps to
complete one";
      PRINT "way travel, then the horizontal motor will move one step
BACKWARD,";
      PRINT "then PZT will be set to 0 and start move up again. "
      PRINT
      PRINT "One data will be taken BEFORE each step of motor scan."
      PRINT : PRINT

610  PRINT "Please input varibles:"

'    INPUT "horizontal travel distance (0 - 25mm): ", XTravelDistance!
'    INPUT "horizontal step size (10 - 1000um): ", XStepSize%

      PRINT "Choose Horizontal Travel Distance(unit:um):"
      INPUT XTravelDistance!

      PRINT "Choose Horizontal Travel Step Size(unit:um):"
      INPUT XStepSize!
      PRINT

'    INPUT "vertical total travel distance (0 - 10mm): ",
YTravelDistance!
'    INPUT "vertical step size (10 - 1000um): ", YStepSize%

      INPUT "voltage step for PZT (0-10 V):", PZTContVolStep!

      PRINT
      PRINT "data acquisition delay time (in seconds): ", Delaytime!
      PRINT "---------------------------------------------"
      PRINT

'*** Calculate the loop numbers:

'    XLoopNumber% = XTravelDistance! * 1000 / XStepSize%   '=# of steps
'    XStepLoopNumber% = XStepSize% * 10 / XMotorStepSize%  '=# of TTL
pulse per step
'    YLoopNumber% = YTravelDistance! * 1000 / YStepSize%
'    YStepLoopNumber% = YStepSize% * 10 / YMotorStepSize%

      XLoopNumber% = XTravelDistance! / XStepSize!   '=# of steps
      XStepLoopNumber% = XStepSize! / XMotorStepSize!   '=# of TTL
pulse per step

      IF (XLoopNumber% + 1) * (YLoopNumber% + 1) > 10500 THEN
      PRINT "too many data, redo please"
      GOTO 610
      END IF

620    INPUT "z-position: "; zp!

      PRINT

      PRINT "step # of horizontal motor = "; XLoopNumber%
```

```
'    PRINT "step # of vertical motor = "; YLoopNumber%
      PRINT "TTL pulses per step of h-motor = "; XStepLoopNumber%
'    PRINT "TTL pulses per step of v-motor = "; YStepLoopNumber%
      PRINT

'    INPUT "Do you want to change above values? (Y/N)", IV$
'    IF UCASE$(IV$) = "Y" THEN GOTO 610

      XDirection$ = "F"       ': YDirection$ = "F"
'   JxSTOP% = 10

      CLS
      LOCATE 1, 1: PRINT "press S key to stop"
      st1$ = st1$ + "h-step #=" + STR$(XLoopNumber%) + "; v-step #=" +
STR$(YLoopNumber%)
      st1$ = st1$ + "; delay=" + STR$(Delaytime!) + "s"
      stepsequence% = 0: beginsecond = TIMER: startime$ = TIME$
      PRINT "step #", "X step #", "PZT Vol(V)", "vol", "phase"

'**** initial reading to check if sensitivity is right
'    CALL snapdata(stepsequence%, vol!, phase!, Delaytime!)
'    stepsequence% = stepsequence% - 1

'---query sensitivity

'    CALL checksensitivity(vol!, phase!, fullvol!, sen%, 0)

'---compare full scale to vol! to see if need to adjust 1 scale up or
down

'    WHILE (vol! > .95 * fullvol!) OR (vol! < .2 * fullvol!)
'    CALL checksensitivity(vol!, phase!, fullvol!, sen%, 1)
'        stepstart! = TIMER
'        WHILE (TIMER - stepstart!) < Delaytime!
'        WEND
'    CALL snapdata(stepsequence%, vol!, phase!, Delaytime!)
'    stepsequence% = stepsequence% - 1
'    WEND

      GOTO 628

'**************test A/D read**********************
'627    wDasErr = KADRead%(hDev, 0, 1, wADValue%)
'    IF (wDasErr <> 0) THEN
'        BEEP
'        PRINT "ERROR"; HEX$(wDasErr); "OCCURRED DURING A/D READ AT 0"
'        STOP
'    END IF

'    CALL BitRead(wADValue%, ADCount%)
'
'    PRINT "A/D read-in = ", ADCount%
'    PZTADReadVol! = (ADCount% - 2048) / 4096 * 2
'    PRINT "A/D Read PZT Control Voltage = ", PZTADReadVol!
```

```
'    PRINT "Do you want to continue your test?"
'    PRINT "If yes, type 1; if no, type 0."
'    INPUT wDasErr
'    IF (wDasErr = 0) THEN
'        STOP
'    END IF
'    GOTO 627
'*********************************************************
'---start of the scann loops

628    FOR Jx% = 0 TO XLoopNumber%

'---move vertical motor up in YLoopNumber% steps
'    FOR Jy% = 1 TO YLoopNumber%

'***** test KDAWrite   speed **************************
'    PZTContVol! = 120!
'    DAWVal& = (INT(PZTContVol! * 4096! / 10!)) * 16
'    PRINT "10000 KDAWrite start time =", TIMER
'    FOR Jy% = 1 TO 10000
'
'        wDasErr = KDAWrite%(hDev, 0, DAWVal&)
'        IF (wDasErr <> 0) THEN
'            BEEP
'            PRINT "ERROR"; HEX$(wDasErr); "OCCURRED DURING D/A WRITE
AT 0"
'            STOP
'        END IF
'     NEXT Jy%
'     PRINT "10000 KDAWrite end time =", TIMER
'**********************************************************************
***

'***** set PZT to 0 at each x position

      PZTContVol! = 0!

637    DAWVal& = (INT(PZTContVol! * 4096! / 10!)) * 16

      wDasErr = KDAWrite%(hDev, 0, DAWVal&)
      IF (wDasErr <> 0) THEN
            BEEP
            PRINT "ERROR"; HEX$(wDasErr); "OCCURRED DURING D/A WRITE AT
0"
            STOP
      END IF

'    INPUT "PZT Control Voltage (0 - 10 V)", PZTContVol!
'    GOTO 637

'******* read from A/D channel 0*****************

'    wDasErr = KADRead%(hDev, 0, 1, wADValue%)
'    IF (wDasErr <> 0) THEN
```

```
'        BEEP
'        PRINT "ERROR"; HEX$(wDasErr); "OCCURRED DURING A/D READ AT 0"
'        STOP
'    END IF

'    CALL BitRead(wADValue%, ADCount%)

'    PRINT "A/D read-in = ", ADCount%
'    PZTADReadVol! = (ADCount% - 2048) / 4096 * 2
'    PRINT "A/D Read PZT Control Voltage = ", PZTADReadVol!
'*************************************************************
'----initial reading to check if sensitivity is right

      CALL snapdata(stepsequence%, vol!, phase!, Delaytime!)
      stepsequence% = stepsequence% - 1

'---query sensitivity

      CALL checksensitivity(vol!, phase!, fullvol!, sen%, 0)

'---compare full scale to vol! to see if need to adjust 1 scale up or
down

      WHILE (vol! > .95 * fullvol!) OR (vol! < .2 * fullvol!)
            CALL checksensitivity(vol!, phase!, fullvol!, sen%, 1)
            stepstart! = TIMER
            WHILE (TIMER - stepstart!) < Delaytime!
            WEND
            CALL snapdata(stepsequence%, vol!, phase!, Delaytime!)
            stepsequence% = stepsequence% - 1
      WEND

      WHILE (PZTContVol! <= 9.995)        '**** move PZT ****

'*** read data first from lock-in ***
      CALL snapdata(stepsequence%, vol!, phase!, Delaytime!)

'*** compare full scale to vol! to adjust 1 scale up or down ***
      WHILE (vol! > .95 * fullvol!) OR (vol! < .3 * fullvol!)
            CALL checksensitivity(vol!, phase!, fullvol!, sen%, 1)
            stepstart! = TIMER
            WHILE (TIMER - stepstart!) < Delaytime!
            WEND
            CALL snapdata(stepsequence% - 1, vol!, phase!, Delaytime!)
      WEND

      PRINT stepsequence%, Jx%, PZTContVol!, vol!, phase!

'*** then move 1 step vertically
'    CALL movestep("Y", YStepLoopNumber%, YDirection$)

'*** move PZT one step ***
      PZTContVol! = PZTContVol! + PZTContVolStep!
      DAWVal& = (INT(PZTContVol! * 4096! / 10!)) * 16
```

```
      wDasErr = KDAWrite%(hDev, 0, DAWVal&)
      IF (wDasErr <> 0) THEN
            BEEP
            PRINT "ERROR"; HEX$(wDasErr); "OCCURRED DURING D/A WRITE AT
0"
            STOP
      END IF

'*** read from A/D channel 0 ***
'    wDasErr = KADRead%(hDev, 0, 1, wADValue%)
'    IF (wDasErr <> 0) THEN
'        BEEP
'        PRINT "ERROR"; HEX$(wDasErr); "OCCURRED DURING A/D READ AT 0"
'        STOP
'    END IF

'    CALL BitRead(wADValue%, ADCount%)

'    PRINT "A/D read-in = ", ADCount%
'    PZTADReadVol! = (ADCount% - 2048) / 4096 * 2
'    PRINT "A/D Read PZT Control Voltage = ", PZTADReadVol!
'*********************************************************************
*

      stepstart! = TIMER

      WHILE (TIMER - stepstart!) < Delaytime!
            IF UCASE$(INKEY$) = "S" THEN
                  BEEP: LOCATE 24, 1
                  stopsecond = TIMER - beginsecond
                  INPUT "stop detected, enter: 1--continue, 2--exit: ",
cc1%
                  beginsecond = TIMER - stopsecond        'reset the
begin time
                  IF cc1% = 2 THEN GOTO 670
            END IF
      WEND

      WEND        'end of PZT scan

'645     NEXT Jy%
'------ end of y-motor loop

'    CALL toggleDirection(YDirection$)       'reverse vertical travel
direction

'*** read data first from lock-in ***
'    CALL snapdata(stepsequence%, vol!, phase!, Delaytime!)

'*** compare full scale to vol! to adjust 1 scale up or down
'    WHILE (vol! > .95 * fullvol!) OR (vol! < .2 * fullvol!)

'       CALL checksensitivity(vol!, phase!, fullvol!, sen%, 1)
'       stepstart! = TIMER
```

```
'       WHILE (TIMER - stepstart!) < Delaytime!
'       WEND
'       CALL snapdata(stepsequence% - 1, vol!, phase!, Delaytime!)
'    WEND

'*** then move horizontal motor by one step ***
      IF Jx% = XLoopNumber% THEN GOTO 655     'do not move at last step

      CALL movestep("Y", XStepLoopNumber%, XDirection$)

      stepstart! = TIMER
      WHILE (TIMER - stepstart!) < Delaytime!
            IF UCASE$(INKEY$) = "S" THEN
                  BEEP: LOCATE 24, 1
                  stopsecond = TIMER - beginsecond
                  INPUT "stop detected, enter: 1--continue, 2--exit: ",
cc1%
                  beginsecond = TIMER - stopsecond
                  IF cc1% = 2 THEN GOTO 670
            END IF
      WEND

655    NEXT Jx%
'----- end of two-motor loop

670     totalsecond = TIMER - beginsecond: stoptime$ = TIME$
      BEEP: BEEP: BEEP
      dt% = (XLoopNumber% + 1) * (YLoopNumber% + 1)
      st1$ = st1$ + "; expected total data #=" + STR$(dt%) + "z-
position=" + STR$(zp!)
      PRINT st1$: PRINT

'find max and min value of the signal
      VolMax! = 0: VolMin! = 10
      FOR m% = 1 TO dt% - 2

      IF VolMax! < AdData(m%) THEN
      VolMax! = AdData(m%)
      max% = m%
      END IF

      IF VolMin! > AdData(m%) THEN
      VolMin! = AdData(m%)
      min% = m%
      END IF

      NEXT m%
      PRINT "maximum voltage ="; VolMax!; "@"; max%
      PRINT "minimum voltage ="; VolMin!; "@"; min%
      PRINT

      INPUT "do you want save data ? (y/n) ", sa$
      IF UCASE$(sa$) = "N" THEN GOTO 60
      ha = 7
```

```
690     GOTO 70

1000    IF datacq% > datasav% THEN
      CLS : LOCATE 10, 1
      INPUT "YOUR DATA MAY NOT BE SAVED ! Do you want to save them
(y/n) ? ", chc$
      IF UCASE$(chc$) = "N" THEN GOTO 1100
      GOTO 60
      END IF

1100    END

SUB adpara (d%)

2000    CLS : LOCATE 10, 1
      INPUT "enter total # of A/D sample per data: ( < 500 ): ",
dsamplenumber
      IF dsamplenumber > 500 OR dsamplenumber < 1 THEN GOTO 2000
2100    INPUT "enter time between samples (in 0.1 us): ", dsampletime
      IF dsampletime < 1000 THEN GOTO 2100
      PRINT "enter signal gain: "
      PRINT "code     <---->    voltage gain"
      PRINT " 0       <---->          1"
      PRINT " 1       <---->         10"
      PRINT " 2       <---->        100"
      PRINT " 3       <---->        500"
2200    INPUT "enter a code: ", ADgaincode
      IF ADgaincode = 3 THEN
      ADgain = 500
      ELSEIF ADgaincode = 2 THEN
      ADgain = 100
      ELSEIF ADgaincode = 1 THEN
      ADgain = 10
      ELSEIF ADgaincode = 0 THEN
      ADgain = 1
      ELSE
      GOTO 2200
      END IF

      CALL initlz(er%, Delaytime!, st1$)

END SUB

SUB BitRead (ADReadIn%, ADReadOut%)
'read 16-bit  integer  bit-by-bit
      DIM max(12) AS INTEGER

'right-shift data 4 bits
      ADReadIn% = ADReadIn% / 16

'pick bit value
      max(1) = ADReadIn% AND &H1
      max(2) = ADReadIn% AND &H2
```

```
      max(3) = ADReadIn% AND &H4
      max(4) = ADReadIn% AND &H8
      max(5) = ADReadIn% AND &H10
      max(6) = ADReadIn% AND &H20
      max(7) = ADReadIn% AND &H40
      max(8) = ADReadIn% AND &H80
      max(9) = ADReadIn% AND &H100
      max(10) = ADReadIn% AND &H200
      max(11) = ADReadIn% AND &H400
      max(12) = ADReadIn% AND &H800

      ADReadOut% = 0
      FOR i% = 1 TO 12
            ADReadOut% = ADReadOut% + max(i%)
      NEXT i%
END SUB

SUB checksensitivity (vol!, phase!, fullvol!, sen%, sta%)
'-- either query or adjust sensitivity according to the value of sta%

SELECT CASE sta%

CASE 0
'-- query the sensitivity setting and calculate full scale voltage
6000    CALL send(8, "SENS?", status%)          '8=lock-in addr
      IF status% <> 0 THEN PRINT status%: STOP

      poll% = 0:
      WHILE (poll% AND 2) = 0          'bit1=high means no command
execution
            CALL spoll(8, poll%, status%)       'serial poll of lock-in
      WEND

      s$ = SPACE$(10)
      CALL enter(s$, length%, 8, status%)
      IF status% <> 0 THEN PRINT status%: STOP

      IF length% > 2 THEN
      PRINT "string length (sens) is too long, read again"
      GOTO 6000
      END IF

      sen$ = LEFT$(s$, 2):    sen% = VAL(sen$)
      fa% = sen% MOD 3                'the remainder of sen% / 3
      ex% = (sen% \ 3) - 9

'calculate the full scale voltage from sen%
      IF fa% = 0 THEN
      fullvol! = 2 * 10 ^ ex%
      ELSEIF fa% = 1 THEN
      fullvol! = 5 * 10 ^ ex%
      ELSE
      fullvol! = 10 ^ (ex% + 1)
      END IF
```

```
CASE ELSE
'--- compare full scale voltage and vol! to adjust sensitivity
6200    fa% = sen% MOD 3
      IF vol! > .95 * fullvol! THEN
      sen% = sen% + 1
            IF fa% = 0 THEN fullvol! = 2.5 * fullvol! ELSE fullvol! = 2
* fullvol!
      ELSEIF vol! < .3 * fullvol! THEN
      sen% = sen% - 1
            IF fa% = 1 THEN fullvol! = fullvol! / 2.5 ELSE fullvol! =
fullvol! / 2
      ELSE
      GOTO 6300
      END IF

      sn$ = "SENS" + STR$(sen%)
      CALL send(8, sn$, status%)         'set the sensitivity

      poll% = 0
      WHILE (poll% AND 2) = 0          'bit1=high means no command
execution
            CALL spoll(8, poll%, status%)         'serial poll of lock-
in
      WEND

END SELECT

6300    END SUB

SUB delay (d1%) STATIC
      FOR j% = 1 TO d1%
      a1! = 1.05 ^ 10
      NEXT j%
END SUB

'**********************************************************************
SUB dproc (ADT%) STATIC

      DIM STotal AS LONG
' use the passed A/D frame handle to perform A/D and data is in
DataBuf()
      nDasErr = KSyncStart%(hAD)
      IF nDasErr <> 0 THEN
      BEEP
      PRINT "ERROR "; HEX$(nDasErr); " OCCURRED DURING 'KSyncStart'":
STOP
      END IF

' convert samples into decimal count (0 to 4095) and averaging

      STotal = 0
      FOR i% = 0 TO dsamplenumber - 1
```

```
      count0% = (DataBuf(i%) / 16) AND &HFFFF          'conversion into
count
      STotal = STotal + count0%
      NEXT i%
      ADT% = STotal / dsamplenumber

END SUB

'**********************************************************************
****
SUB GRAPHICSINITIALIZE (XMIN, xmax, Ymin, Ymax, XLABEL$, YLABEL$)
STATIC

'This routine puts up a graphics window, leaving room for axis
labelling.
'It leaves the graphics screen in "real world" coordinates so no data
'transformations are necessary before plotting.  Also makes the last
four
'lines of the screen a text window, so as to leave the graphics
undisturbed.

SCREEN 9        'set up 640x350 graphics

VIEW (113, 1)-(638, 270), , 1   'initialize size of graphics window
                        'leaving room at left for labelling and
                        'four line text window at bottom
COLOR 7, 0

'if y label is > 18 characters, just take the first 18 characters
IF LEN(YLABEL$) > 18 THEN YLABEL$ = LEFT$(YLABEL$, 18)
LASTCHAR% = LEN(YLABEL$)
'print y axis label vertically in column 13 centered about line 10
FOR j% = 1 TO LASTCHAR%
      LOCATE j% + 3, 13: PRINT MID$(YLABEL$, j%, 1)
NEXT j%

'if the x label is longer than 39 characters, just take the first 39
IF LEN(XLABEL$) > 39 THEN XLABEL$ = LEFT$(XLABEL$, 39)
LASTCHAR% = LEN(XLABEL$)
'print x axis label on line 21 centered about column 46
LOCATE 21, 46 - LASTCHAR% / 2: PRINT XLABEL$

'print axis extrema
LOCATE 1, 1: PRINT SPACE$(13 - LEN(STR$(Ymax))); Ymax
LOCATE 20, 1: PRINT SPACE$(13 - LEN(STR$(Ymin))); Ymin
LOCATE 21, 15: PRINT XMIN
LOCATE 21, 67: PRINT SPACE$(13 - LEN(STR$(xmax))); xmax

WINDOW (XMIN, Ymax)-(xmax, Ymin)    'define graphics window
                              'in "real world" coordinates

PSET (XMIN, Ymin)     'put the graphics pen in the lower left corner
                  'use "LINE -(xpoint,ypoint)" to connect points.
```

```
END SUB

SUB initlz (er%, Delaytime!, st1$)
' initialization of the internal data tables according to step.CFG /
DAS1600

'     szCfgName = "step.CFG" + CHR$(0)
      szCfgName = "DAS1600.CFG" + CHR$(0)
      nDasErr = DAS1600DEVOPEN%(SSEGADD(szCfgName), nBoards)
      IF nDasErr <> 0 THEN
      BEEP
      PRINT "ERROR "; HEX$(nDasErr); " OCCURRED DURING
'DAS1600DEVOPEN'": STOP
      END IF

'-----------------------------------------------------------------------
-----
' establishment of communication with the driver through the Device
Handle.

      nDasErr = DAS1600GETDEVHANDLE%(0, hDev)
      IF (nDasErr <> 0) THEN
      BEEP
      PRINT "ERROR "; HEX$(nDasErr); " OCCURRED DURING
'DAS1600GETDEVHANDLE'": STOP
      END IF

'-----------------------------------------------------------------------
-----
' get a Handle to an A/D Frame (the data tables inside the driver
pertaining
' to A/D operations).

      nDasErr = KGetADFrame%(hDev, hAD)
      IF (nDasErr <> 0) THEN
      BEEP
      PRINT "ERROR "; HEX$(nDasErr); " OCCURRED DURING 'KGETADFRAME'":
STOP
      END IF

'-----------------------------------------------------------------------
-----
' Assign the data array declared above to the Frame Handle, and specify
' number of samples to acquire.

      nDasErr = KSetBufI%(hAD, DataBuf(0), dsamplenumber)
      IF (nDasErr <> 0) THEN
      BEEP
      PRINT "ERROR "; HEX$(nDasErr); " OCCURRED DURING 'KSetBufI'":
STOP
      END IF

'-----------------------------------------------------------------------
-----
```

```
' Create the array of channel/gain pairs

      CHANGAINARRAY(0) = 1                    ' # of chan/gain pairs
      CHANGAINARRAY(1) = 0                    ' Chan 0
      CHANGAINARRAY(2) = ADgaincode           ' AD gain code
PRINT ADgaincode

'-----------------------------------------------------------------------
-----
' Reformat the channel/gain array for DAS-1600 driver.

      nDasErr = KFormatChanGAry%(CHANGAINARRAY(0))
      IF nDasErr <> 0 THEN
      BEEP
      PRINT "ERROR "; HEX$(nDasErr); " OCCURRED DURING
'KFormatChnGAry'": STOP
      END IF

'-----------------------------------------------------------------------
-----
' Assign the reformatted Channel/Gain array to the A/D Frame.

      nDasErr = KSetChnGAry%(hAD, CHANGAINARRAY(0))
      IF nDasErr <> 0 THEN
      BEEP
      PRINT "ERROR "; HEX$(nDasErr); " OCCURRED DURING 'KSetChnGAry'":
STOP
      END IF

'-----------------------------------------------------------------------
-----
' uses the internal clock source of f=10MHz to set period between
conversions.

      nDasErr = KSetClkRate%(hAD, dsampletime)    't=dsampletime/f
(sec)
      IF nDasErr <> 0 THEN
      BEEP
      PRINT "ERROR "; HEX$(nDasErr); " OCCURRED DURING 'KSetClkRate'":
STOP
      END IF
PRINT dsampletime
'-----------------------------------------------------------------------
-----
'initilize the GPIB488 board and lock-in amplifier
      CALL initialize(18, 0)
'set lock-in output control to 488 board (need to be done first)
      CALL send(8, "OUTX 1", status%)          '
'other parameters for lock-in
      CLS : tc% = -1: sl% = -1
      PRINT "Setting the lock-in time constants:"
      PRINT
      PRINT "code ---- time constant"
      PRINT " 4 ---- 1 ms"
```

```
      PRINT " 5 ---- 3 ms"
      PRINT " 6 ---- 10 ms"
      PRINT " 7 ---- 30 ms"
      PRINT " 8 ---- 100 ms"
      PRINT " 9 ---- 300 ms"
      PRINT "10 ---- 1 s"
      PRINT "11 ---- 3 s"
      PRINT "12 ---- 10 s"
      WHILE (tc% > 12) OR (tc% < 4)
            INPUT "enter time constant code = "; tc%
      WEND
      tc$ = "OFLT" + STR$(tc%)

      mo% = tc% MOD 2                'the remainder of tc% / 3
      di% = (tc% \ 2) - 2

'calculate the time constant from tc% in ms
      IF mo% = 0 THEN
      tmct% = 10 ^ di%
      ELSE
      tmct% = 3 * 10 ^ di%
      END IF
      PRINT "time constant = "; tmct%; " ms"

      PRINT
      PRINT "code ---- filter slope"
      PRINT " 0 ---- 6 dB"
      PRINT " 1 ---- 12 dB"
      PRINT " 2 ---- 18 dB"
      PRINT " 3 ---- 24 dB"
      WHILE (sl% > 3) OR (sl% < 0)
            INPUT "enter slope code = "; sl%
      WEND
      sl$ = "OFSL" + STR$(sl%)

'calculate delay time according to lock-in setting
SELECT CASE sl%
      CASE 0
      Delaytime! = 5 * tmct% / 1000           'in second
      CASE 1
      Delaytime! = 7 * tmct% / 1000           'in second
      CASE 2
      Delaytime! = 8.5 * tmct% / 1000           'in second
      CASE 3
      Delaytime! = 10 * tmct% / 1000           'in second
END SELECT

      CALL send(8, tc$, status%)        'set the time constant
      CALL send(8, sl$, status%)        'set the filter slope
      CALL send(8, "AGAN", status%)         'set the autogain mode

      poll% = 0: t1! = TIMER
      WHILE (poll% AND 2) = 0            'bit1=high means no command
execution
```

```
            CALL spoll(8, poll%, status%)      'serial poll of lock-in
      WEND
      PRINT "lock-in setting delay = "; TIMER - t1!
      PRINT "data reading delay time = "; Delaytime!
      PRINT "hit any key to complete initilization"
      st1$ = "time const=" + STR$(tmct%) + "ms" + "; slope code=" +
STR$(sl%) + "; "
      DO WHILE INKEY$ = "": LOOP

END SUB

SUB motorctrl (dir%, stnumber%, trnumber%, J1%, de1$) STATIC

      CLS
      PRINT "hit S to stop"

' motor driving loop for full travel
4400    FOR J1% = 0 TO trnumber% - 1
'         INPUT "enter integer parameter: ", otherdata(J10%)
      PRINT J1% + 1; "th: wait...";
      CALL dproc(ADT%)
      AdData(J1%) = ADT%
      PRINT "done;  vol= "; (ADT% / 4096) * 10; ", now drive the
motor...";

'motor driving loop for one move
      FOR J20% = 1 TO stnumber%
      value = 2 + dir%                        'go to high
      dwOUTVal = value
      nDasErr = KDOWrite%(hDev, 0, dwOUTVal)
      IF nDasErr <> 0 THEN
      BEEP:  PRINT "ERROR "; HEX$(nDasErr); " DURING 'KDOWrite'": STOP
      END IF

      value = 0 + dir%                        'go to low
      dwOUTVal = value
      nDasErr = KDOWrite%(hDev, 0, dwOUTVal)
      IF nDasErr <> 0 THEN
      BEEP:  PRINT "ERROR "; HEX$(nDasErr); " DURING 'KDOWrite'": STOP
      END IF

      CALL delay(2000)                'delay between steps

      NEXT J20%

      tmcount! = TIMER
      PRINT "done.  "

      IF UCASE$(INKEY$) = "S" THEN
      INPUT "continue (C) or exit to menu (E) ?", rl$
      IF UCASE$(rl$) = "E" THEN GOTO 4500
      END IF

      IF UCASE$(de1$) = "N" THEN GOTO 4480
```

```
      LastData% = AdData(J1% - 1)
      IF ABS(LastData% - ADT%) / ABS(LastData% + ADT%) < .01 THEN GOTO
4480

      DO                              'delay loop between moves
        tmdiff! = TIMER - tmcount!
      LOOP UNTIL tmdiff! > 1.7

4480    NEXT J1%

4500
      END SUB

SUB movestep (Axis$, StepSize%, Direction$)
'New Subroutine for two step motor contral through port A of J2
connector
'bit0=h-motor dir, bit1=h-motor step, bit2=v-motor dir, bit3=v-motor
step
'motor moves one step on each positive edge of TTL
'Axis$ -- choose the step motor (X or Y)
'StepSize%--- number of loops for each move
'Direction$-- Moving direction

      IF Axis$ = "X" THEN
            MoveValue0% = 2           'move h-motor by setting bit1
high (0010)
            IF Direction$ = "F" THEN
            dir% = 0          'forward direction (bit0=0)
            ELSE
            dir% = 1          'backward direction (bit0=1)
            END IF
      ELSE
            MoveValue0% = 8           'move v-motor by setting bit 3
high (1000)
            IF Direction$ = "F" THEN
            dir% = 0          'forward direction (bit2=0)
            ELSE
            dir% = 4          'backward direction (bit2=1)
            END IF
      END IF

'move one step on positive edge for StepSize% steps
      FOR J10% = 1 TO StepSize%
      MoveValue% = MoveValue0% + dir%
      dwOUTVal% = MoveValue%
      nDasErr = KDOWrite%(hDev, 0, dwOUTVal%)    'write to digital
ports
      IF nDasErr <> 0 THEN
      BEEP:  PRINT "ERROR "; HEX$(nDasErr); " DURING 'KDOWrite'": STOP
      END IF

'reset the TTL output to 0
      MoveValue% = 0 + dir%
      dwOUTVal% = MoveValue%
```

```
      nDasErr = KDOWrite%(hDev, 0, dwOUTVal%)
      'nDasErr = KDOWrite%(hDev, 0, MoveValue%)
      IF nDasErr <> 0 THEN
      BEEP:  PRINT "ERROR "; HEX$(nDasErr); " DURING 'KDOWrite'": STOP
      END IF

      CALL delay(3000)          'need to change the input parameter for
different PC

      NEXT J10%

END SUB

DEFSNG H-Z
SUB moving (dr$, stpsz!) STATIC
' this subroutine use 8254 counter/timer 0 with internal 100kHz clock
as
' square wave generator and an external divide-by-ten dividing chip (on
the
' small board connected to J1 connector) to drive the motor.
' (ref: user's guide, p.E-20)

      nCtrlData = &H34        'word to be writen to 8254 control
register
                        'to setup the timer
      nDasErr = DAS16008254CONTROL%(0, nCtrlData)
      IF (nDasErr <> 0) THEN
      BEEP
      PRINT "ERROR "; HEX$(nDasErr); " OCCURRED DURING
'DAS16008254CONTROL'": STOP
      END IF


'-----------------------------------------------------------------------
-----
' Enable 100KHz clock as time base for counter/timer 0

      nDasErr = DAS16008254SETCLK0(0, 0)      '0 = internal, 1 =
external
      IF (nDasErr <> 0) THEN
      BEEP: PRINT "ERROR "; HEX$(nDasErr); " OCCURRED DURING
'DAS16008254SETCLK0'": STOP
      END IF

'-----------------------------------------------------------------------
-----
' Prompts for motor operation variables
      CLS : LOCATE 10, 10
5040    INPUT "If you turn on the HALF STEP switch, enter Y; otherwise
enter N: ", HS$
      IF UCASE$(HS$) = "N" THEN hsf = 2 ELSE hsf = 1
5050    INPUT "Enter the distance of travel in unit of (mm)  >>>  ",
distance
      IF distance > 100 THEN
```

```
      PRINT "you must enter distance less than 100 mm, please redo"
      GOTO 5050
      END IF
5070    PRINT "after the input of following data, motor will run !!! "
      INPUT "Enter motor speed in unit of (mm/s)   >>>  ", speed
      speed = speed / hsf

      IF UCASE$(dr$) = "F" THEN
      dir = 0
      ELSE
      dir = 1
      END IF

' (1) prdcnt (<32,000) is the number of base period (10us) for each
output
'     pulse @ CTR0 OUT @ rate=100k(Hz)/prdcnt which must be > 3(Hz)
' (2) divide-by-mv% chips was added for lower rate:
rate=100k(Hz)/(prdcnt*mv%)
'     which becomes > 3/mv%(Hz)
' (3) with stepsz! in unit of (um) and speed of (mm/s) thus:
'       speed = rate * stpsz! * .001 = 100*stpsz!/prdcnt/mv%

      mv% = 10
      prdcnt = 100 * stpsz! / speed / mv%

      IF prdcnt > 32000 THEN
      PRINT "you must enter a smaller speed (mm/s), please redo"
      GOTO 5070
      END IF

      traveltime = distance / (speed * hsf)
'period count number based on 100kHz time base: nCountData=100 -->
rate=1kHz
      nCountData = prdcnt
' Write initial value to counter/timer 0 based on control word R/W
format
' this will enable the CTR0 pulse output
' Low byte first
      nDasErr = DAS16008254SETCOUNTER(0, 0, nCountData)
      IF (nDasErr <> 0) THEN
      BEEP: PRINT "ERROR "; HEX$(nDasErr); " OCCURRED DURING
'DAS16008254SETCOUNTER'": STOP
      END IF

' High byte second (divide by 256 is the same as shifting right by 8
bits)
      nDasErr = DAS16008254SETCOUNTER(0, 0, INT(nCountData / 256))
      IF (nDasErr <> 0) THEN
      BEEP: PRINT "ERROR "; HEX$(nDasErr); " OCCURRED DURING
'DAS16008254SETCOUNTER'": STOP
      END IF

5090    n = 0: totaltime = 0: prvstime = 0
```

```
'start of the driving loop
5100    dwOUTVal = 4 + dir
'enable the logic gates in the home-made control circuit for motor
driver
      nDasErr = KDOWrite%(hDev, 0, dwOUTVal)
      IF nDasErr <> 0 THEN
      BEEP
      PRINT "ERROR "; HEX$(nDasErr); " DURING 'KDOWrite'": STOP
      END IF
      PRINT "Running ...  press S to STOP:  "

      begintime = TIMER
'PRINT prvstime; begintime

'time control loop
      WHILE totaltime <= traveltime
            IF UCASE$(INKEY$) = "S" THEN
            dwOUTVal = 0                     'stop the motor driving
            nDasErr = KDOWrite%(hDev, 0, dwOUTVal)
                  IF nDasErr <> 0 THEN
                  BEEP: PRINT "ERROR "; HEX$(nDasErr); " DURING
'KDOWrite'": STOP
                  END IF
            prvstime = TIMER - begintime + prvstime: BEEP
            INPUT "press: 1--continue; 2--menu  ", n1%
                  IF n1% = 2 THEN GOTO 5200 ELSE GOTO 5100
            END IF
            totaltime = TIMER - begintime + prvstime
            IF totaltime > (traveltime - 7) THEN       'start of the
ending warning
            SOUND 200 + n, 1
            n = n + 1
            END IF

      WEND

      dwOUTVal = 0                     'stop the motor driving
      nDasErr = KDOWrite%(hDev, 0, dwOUTVal)
      IF nDasErr <> 0 THEN
            BEEP: PRINT "ERROR "; HEX$(nDasErr); " DURING 'KDOWrite'":
STOP
      END IF
      BEEP: BEEP: BEEP

'end of drivng loop

      PRINT "total time: "; totaltime; "(s),   speed: "; distance /
totaltime; "(mm/s)"
      IF dir = 0 THEN dir = 1 ELSE dir = 0            'direction toggle
      INPUT "Toggle direction and run again (y/n) ? ", ch20$
      IF UCASE$(ch20$) = "N" THEN GOTO 5200
      GOTO 5090

5200    END SUB
```

```
DEFINT H-Z
SUB procpara (st1$, Ymin%, Ymax%)

      CLS : LOCATE 10, 1
4000    INPUT "enter total # of data you want to take (<10000): ",
conumber
      IF conumber > 10000 OR conumber < 1 THEN GOTO 4000
      INPUT "enter time between data acquisition (in seconds): ",
dactime
      INPUT "enter test parameter: ", st1$
      INPUT "enter Y_mim (0 - 4096) for screen display: ", Ymin%
      INPUT "enter Y_max (0 - 4096) for screen display: ", Ymax%

END SUB

SUB saving (startime$, stoptime$, st1$, totalsecond, K1%)

3000    LOCATE 22, 1
      INPUT "enter output data file name: ", fil$
      IF fil$ = "" THEN GOTO 3000
      OPEN fil$ FOR OUTPUT AS #1

      timemark$ = startime$ + "---" + stoptime$
      vollim! = 10 / ADgain
      PRINT #1, DATE$, timemark$
      PRINT #1, "total seconds: ", totalsecond
      PRINT #1, "total minutes: ", totalsecond / 60
      PRINT #1, "actual number of data: ", K1%
      PRINT #1, "Input Voltage Range: 0 - "; vollim!; "(volt)"
      PRINT #1, "total # of sample per data = "; dsamplenumber; ";"
      PRINT #1, "period between samples = "; dsampletime * .0005;
"(ms)"
      PRINT #1, st1$
      PRINT #1, "-----------"
      PRINT #1, K1%

      IF svpointer = 300 THEN
      PRINT #1, " data count"; "  parameter"
      END IF

      FOR p1% = 0 TO K1% - 1
      IF svpointer = 300 OR svpointer = 600 THEN
      PRINT #1, AdData(p1%), otherdata(p1%)
      ELSE
      PRINT #1, AdData(p1%)
      END IF
      NEXT p1%

      CLOSE

END SUB

SUB selemenu (ha) STATIC
```

```
      SCREEN 0: CLS : LOCATE 10, 1
      PRINT "SELECT MODE: "
      PRINT " 1 ---- Setting data acquisition parameters"
      PRINT " 2 ---- Setting A/D board parameters "
      PRINT
      PRINT " 3 ---- Start single-shot data acquisition"
      PRINT " 4 ---- Start continuous data acquisition "
      PRINT
      PRINT " 5 ---- One stepping motor control (using J1 connector)"
'     PRINT " 6 ---- Two stepping motor control (using J2 connetor)"
      PRINT " 6 ---- Confocal: PZT and One stepping motor"
      PRINT
      PRINT " 7 ---- Saving data to file "
      PRINT " 8 ---- Exit "
      PRINT
      INPUT " enter a number: ", ha

END SUB

SUB snapdata (stepsequence%, vol!, phase!, Delaytime!)

7000    lastvol! = vol!
      CALL send(8, "SNAP?3,4", status%)        'querylock-in output R
AND THETA

      poll% = 0
      WHILE (poll% AND 2) = 0          'bit1=high means no command
execution
            CALL spoll(8, poll%, status%)         'serial poll of lock-
in
      WEND

      r$ = SPACE$(50)
      CALL enter(r$, length%, 8, status%)
      vol$ = LEFT$(r$, length%)

      IF length% < 10 THEN
      PRINT "string length is wrong, read again"
      GOTO 7000
      END IF

      ln% = length% - 1
      WHILE MID$(vol$, ln%, 1) <> ","
            ln% = ln% - 1
      WEND
      ll% = length% - ln%

      v$ = LEFT$(vol$, ln% - 1): theta$ = RIGHT$(vol$, ll%)
      vol! = VAL(v$): phase! = VAL(theta$)

' take twice longer to read data for large variation
      IF stepsequence% < 1 THEN GOTO 7100
```

```
      tt1! = TIMER
      IF ABS(lastvol! - vol!) > .2 * lastvol! THEN
            WHILE (TIMER - tt1!) < Delaytime!
            WEND
            GOTO 7000
      END IF

7100    AdData(stepsequence%) = vol!
      otherdata(stepsequence%) = phase!
      stepsequence% = stepsequence% + 1

END SUB

SUB toggleDirection (Direction$)
IF Direction$ = "F" THEN
      Direction$ = "R"
ELSE
      Direction$ = "F"
END IF

END SUB
```

A.7 Experimental Data of R_d, T_d, and T_c for Porcine Dermis at 325 nm, 442 nm, 532 nm, 632.8 nm, 850 nm, 1064 nm, 1330 nm, and 1550 nm

Wavelength (nm)	R_d	T_d	T_d	Thickness (mm)
325	0.23970	0.077175	1.9977×10^{-6}	0.31
	0.23887	0.080543	2.2606×10^{-6}	0.32
	0.24330	0.082808	2.3836×10^{-6}	0.35
	0.24521	0.082411	2.2247×10^{-6}	0.29
	0.24857	0.072434	1.6667×10^{-6}	0.29
442	0.22255	0.13161	5.2262×10^{-6}	0.49
	0.17572	0.20032	1.3116×10^{-5}	0.28
	0.19186	0.14454	7.0528×10^{-6}	0.47
	0.19402	0.16439	7.3314×10^{-6}	0.39
	0.24489	0.098015	3.1297×10^{-6}	0.53
532	0.11721	0.37484	4.6444×10^{-5}	0.32
	0.15357	0.27957	1.5763×10^{-5}	0.40
	0.12746	0.29977	1.5996×10^{-5}	0.38
	0.17630	0.18309	7.2656×10^{-6}	0.71
	0.16205	0.22745	9.2072×10^{-6}	0.53

632.8	0.13595	0.30702	1.4966×10^{-5}	0.54
	0.14539	0.28927	1.4122×10^{-5}	0.68
	0.13006	0.32592	1.7470×10^{-5}	0.49
	0.11003	0.40032	3.7433×10^{-5}	0.39
	0.13925	0.32083	1.9652×10^{-5}	0.55
850	0.10506	0.40832	2.2115×10^{-5}	0.58
	0.11353	0.37396	1.9439×10^{-5}	0.49
	0.07123	0.58783	7.3364×10^{-5}	0.33
	0.10980	0.36753	1.9902×10^{-5}	0.48
	0.09156	0.42504	2.5252×10^{-5}	0.46
1064	0.092588	0.54550	7.1006×10^{-5}	0.50
	0.071364	0.59834	9.9329×10^{-5}	0.37
	0.075033	0.61865	1.3838×10^{-4}	0.35
	0.13746	0.34726	4.5773×10^{-5}	0.54
	0.22472	0.34776	5.5714×10^{-5}	0.46
1310	0.083625	0.49633	1.2045×10^{-4}	0.44

	0.094692	0.43392	4.8034×10^{-5}	0.53
	0.081498	0.49742	1.2443×10^{-4}	0.37
	0.083650	0.48759	1.2400×10^{-4}	0.44
	0.072600	0.31670	2.4563×10^{-5}	0.84
1550	0.07483	0.17580	2.2525×10^{-5}	0.82
	0.07506	0.12480	1.1367×10^{-5}	0.98
	0.07499	0.20060	3.4741×10^{-5}	0.75
	0.07531	0.18570	2.1074×10^{-5}	0.83
	0.07519	0.18000	2.2541×10^{-5}	0.82

A.8 Refractive Index of BK7 Glass, UV Glass, and Porcine Dermis

Wavelength (nm)	BK7 Glass	UV Glass	Porcine Dermis
325	1.5451	1.4816	1.3933
442	1.5261	1.4662	1.3755
532	1.5195	1.4607	1.3586
632.8	1.5151	1.4570	1.3539
850	1.5098	1.4525	1.3635
1064	1.5066	1.4496	1.3599
1310	1.5036	1.4468	1.3571
1550	1.5007	1.4440	1.3608